National Library of Canada
Acquisitions and Bibliographic Services Branch
395 Wellington Street
Ottawa, Ontario
K1A 0N4

Bibliothèque nationale du Canada
Direction des acquisitions et des services bibliographiques
395, rue Wellington
Ottawa (Ontario)
K1A 0N4

Your file Votre référence

Our file Notre référence

NOTICE

The quality of this microform is heavily dependent upon the quality of the original thesis submitted for microfilming. Every effort has been made to ensure the highest quality of reproduction possible.

If pages are missing, contact the university which granted the degree.

Some pages may have indistinct print especially if the original pages were typed with a poor typewriter ribbon or if the university sent us an inferior photocopy.

Reproduction in full or in part of this microform is governed by the Canadian Copyright Act, R.S.C. 1970, c. C-30, and subsequent amendments.

AVIS

La qualité de cette microforme dépend grandement de la qualité de la thèse soumise au microfilmage. Nous avons tout fait pour assurer une qualité supérieure de reproduction.

S'il manque des pages, veuillez communiquer avec l'université qui a conféré le grade.

La qualité d'impression de certaines pages peut laisser à désirer, surtout si les pages originales ont été dactylographiées à l'aide d'un ruban usé ou si l'université nous a fait parvenir une photocopie de qualité inférieure.

La reproduction, même partielle, de cette microforme est soumise à la Loi canadienne sur le droit d'auteur, SRC 1970, c. C-30, et ses amendements subséquents.

Canada

UNIVERSITY OF ALBERTA

Polarimetry with a Wide-Field Aperture Synthesis Radio Telescope

By

© Richard James Smegal

A thesis submitted to the Faculty of Graduate Studies and Research in partial fulfillment of the requirements for the degree of Doctor of Philosophy.

DEPARTMENT OF ELECTRICAL ENGINEERING

Edmonton, Alberta
SPRING 1995

National Library of Canada

Acquisitions and Bibliographic Services Branch

395 Wellington Street
Ottawa, Ontario
K1A 0N4

Bibliothèque nationale du Canada

Direction des acquisitions et des services bibliographiques

395, rue Wellington
Ottawa (Ontario)
K1A 0N4

Your file Votre référence

Our file Notre référence

THE AUTHOR HAS GRANTED AN IRREVOCABLE NON-EXCLUSIVE LICENCE ALLOWING THE NATIONAL LIBRARY OF CANADA TO REPRODUCE, LOAN, DISTRIBUTE OR SELL COPIES OF HIS/HER THESIS BY ANY MEANS AND IN ANY FORM OR FORMAT, MAKING THIS THESIS AVAILABLE TO INTERESTED PERSONS.

L'AUTEUR A ACCORDE UNE LICENCE IRREVOCABLE ET NON EXCLUSIVE PERMETTANT A LA BIBLIOTHEQUE NATIONALE DU CANADA DE REPRODUIRE, PRETER, DISTRIBUER OU VENDRE DES COPIES DE SA THESE DE QUELQUE MANIERE ET SOUS QUELQUE FORME QUE CE SOIT POUR METTRE DES EXEMPLAIRES DE CETTE THESE A LA DISPOSITION DES PERSONNE INTERESSEES.

THE AUTHOR RETAINS OWNERSHIP OF THE COPYRIGHT IN HIS/HER THESIS. NEITHER THE THESIS NOR SUBSTANTIAL EXTRACTS FROM IT MAY BE PRINTED OR OTHERWISE REPRODUCED WITHOUT HIS/HER PERMISSION.

L'AUTEUR CONSERVE LA PROPRIETE DU DROIT D'AUTEUR QUI PROTEGE SA THESE. NI LA THESE NI DES EXTRAITS SUBSTANTIELS DE CELLE-CI NE DOIVENT ETRE IMPRIMES OU AUTREMENT REPRODUITS SANS SON AUTORISATION.

ISBN 0-612-01761-3

Canada

University of Alberta

Library Release Form

Name of Author: Richard J. Smegal

Title of Thesis: Polarimetry with a Wide-Field Aperture Synthesis Radio Telescope

Degree: Doctor of Philosophy

Year this Degree Granted: 1995

Permission is hereby granted to the University of Alberta Library to reproduce single copies of this thesis and to lend or sell such copies for private, scholarly, or scientific research purposes only.

The author reserves all other publication and other rights in association with the copyright in the thesis, and except as hereinbefore provided, neither the thesis nor any substantial portion thereof may be printed or otherwise reproduced in any material form whatever without the author's prior written permission.

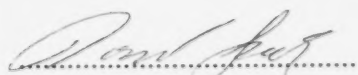

Penticton, B.C., Canada

april 20, 1995

UNIVERSITY OF ALBERTA

FACULTY OF GRADUATE STUDIES AND RESEARCH

The undersigned certify that they have read, and recommended to the Faculty of Graduate Studies and Research for acceptance, a thesis entitled *Polarimetry with a Wide-Field Aperture Synthesis Radio Telescope* submitted by Richard J. Smegal in partial fulfilment of the requirements for the degree of Doctor of Philosophy.

Dr. J. F. Vaneldik (Supervisor)

Dr. T.L. Landecker (Co-Supervisor)

Dr. D. Routledge

Dr. D.P. Hube

Dr. F.E. Vermeulen

Dr. C.V. Wilson

Date: March 31, 1995

Abstract

Polarimetry has been added to the wide-field aperture synthesis radio telescope at the Dominion Radio Astrophysical Observatory. This addition has significantly extended the ability of this telescope to explore the astrophysics of large low brightness objects at arcminute resolution at 21 cm wavelength.

A unique combination of equatorial antenna mounts and circularly polarized non-rotatable feed antennas preclude the option of using calibration techniques established for other synthesis telescopes.

A directional coupler is shown to be a good model for a polarization transducer. A transducer formed by a four port network that is matched, lossless and reciprocal will permit the measurement of polarized intensity without the need for special calibration techniques. Although low in ohmic losses, practical networks suffer from mismatch losses, and require calibration and correction for non-orthogonality. Calibration of transducer orthogonality is readily accomplished for this type of instrument but determination of the array polarization is not. However it is shown that the polarization of the antennas need not be known exactly, providing that the feed polarization is predominately circular and the source polarization is linear.

Polarization of the antenna feeds was measured in an antenna range and confirmed adequate to allow polarimetry with orthogonality calibration only. The phase-amplitude method for antenna measurement was employed and proved to be of great utility in situations where preparation and set-up are a major undertaking. A technique to calibrate the field probes involved in this method of measurement is presented which allows the use of probes with both arbitrary and unknown polarization.

A technique for calibrating the orthogonality of the array was implemented and its operation verified by a number of astronomical test observations. The results are presented. Observations made of the extended supernova remnant DA530 placed at two different positions in the field of view demonstrate that the telescope is capable of polarimetric imaging of extended objects up to 0.5 degree in angular size and has a usable field of view, for polarimetry, of at least 1.5 degrees.

Acknowledgement

The author acknowledges the immense support of his supervisors Fred Vaneldik, Tom Landecker and Dave Routledge at the University of Alberta. The entire staff of the Dominion Radio Astrophysical Observatory were instrumental in attaining the objectives of this thesis, moreover, they provided a stimulating and enjoyable environment in which to work, for which the author is grateful.

Jason Kingston and company at 'Over the Top Pizza Shop' will be remembered for keeping body and soul united during many long work sessions over the course of this thesis.

Contents

1 Introduction 1

1.1 The DRAO Synthesis Telescope 1

1.2 Astrophysical Implications of Polarimetry 3

1.3 The Technical Challenge 6

2 Instrument Description and Models 7

2.1 Aperture Synthesis and Polarimetry 7

2.1.1 Properties of the radiation 8

2.1.2 Interferometry and aperture synthesis 13

2.1.3 Polarimetry with a synthesis telescope 15

2.2 Instrumental Considerations 24

2.2.1 Co-ordinate systems and telescope geometry 24

2.2.2 The DRAO synthesis telescope co-ordinate system 29

2.2.3 Circular polarization ratio 29

2.2.4 Instrument model 31

2.2.5 Antenna system 33

2.2.6 Waveguide components and the direction coupler model . . . 34

2.2.7 Frequency conversion 39

2.2.8 Correlator output 40

2.2.9 Coupler orthogonality and instrumental polarization 42

3 Telescope Calibration 44

3.1 Calibration and Correction of Instrumental Effects 44

3.1.1 The need for interferometer response correction 45

3.1.2 Uncertainty due to unknown RHCP-LHCP phase difference . 47

3.1.3 Errors due to uncertainty in antenna polarization 48

3.1.4 Errors due to non-orthogonality and non-similarity 49

3.1.5 Array orthogonality 56

3.1.6 Summary 58

3.2 Calibration Methodology 59

3.2.1 Channel gain calibration 59

3.2.2 Channel orthogonality calibration 61

3.2.3 Cross-polarization reference phase determination 62

3.2.4 Array polarization calibration 63

3.2.5 Visibility data correction 64

3.2.6 The implementation details 65
3.2.7 Overview of the calibration and correction process 65
3.2.8 Channel gain calibration 68
3.2.9 Channel orthogonality 68
3.2.10 Cross-polarization reference gain 69
3.2.11 The calibration database 69
3.2.12 Calibration sources 69
3.3 Verification of the calibration process 70
3.3.1 Sky measurements 71
3.4 Noise and Error in Polarization Measurement 78
3.4.1 Conclusions 85

4 Antenna Measurements **87**
4.1 Antenna Measurement Programme at DRAO 87
4.2 Antenna Measurements Using the Phase-amplitude Method 89
4.2.1 Theory of the method 91
4.2.2 Channel gain calibration 92
4.2.3 Calibration of probes of unknown polarization 93
4.2.4 Implementation of the phase-amplitude measurement range . 95
4.3 Measurement Results 99
4.3.1 Feed measurements 99
4.3.2 Antenna range errors 103
4.3.3 Probe calibration test 106
4.3.4 Comparison with telescope observations 107
4.3.5 Conclusions 113

5 DA530 : A Test Observation **115**
5.1 Introduction 115
5.2 Observations and Analysis 117
5.2.1 Comparison of centred and offset observations 119
5.2.2 Comparison with other observations 123
5.3 Conclusions 124

Bibliography **134**

List of Figures

2.1 Geometrical relationship between a celestial source and the synthesis telescope. 13
2.2 Relationship between the co-ordinate system describing the polarization of the source (A) and the ground based co-ordinate system describing the synthesis telescope (B). 17
2.3 The Poincaré sphere and its relation to the Stokes parameters and coherency elements. 21
2.4 The co-ordinate transformation for expressing Stokes parameters in terms of the coherency elements for circularly polarized components. 22
2.5 Geometrical relationship of the visibility, map, track and polarization co-ordinates. The systems are shown at HA 0 and declination, $\delta = 90°$. 26
2.6 Direction cosines and their relation to the celestial sphere. 27
2.7 A block diagram of the synthesis telescope model. 43

3.1 Stokes Q and V parameters as a function of RHCP contamination of the LHCP channel. 50
3.2 Error in linearly polarized flux measurement as a function of RHCP contamination of the LHCP channel. The four traces represent varying amounts of circularly polarized flux present. 51
3.3 Polarization ellipses representing orthogonal but non-identical antennas in an interferometer are shown by the two left diagrams and of identical but non-orthogonal antennas by the right. 52
3.4 The ratio of total intensity observed with an inteferometer consisting of non-identical antennas, each providing orthogonal outputs, to the true value of total intensity. Labels on the curves represent the fraction of polarization and ellipse tilt of the received radiation. . . . 54
3.5 The visibility phase as observed by an interferometer consisting of non-identical antennas with orthogonal outputs. The true visibility phase is zero. Labels on the curves represent the fraction of polarization and ellipse tilt of the received radiation. 55
3.6 The imaginary part of Stokes Q observed for an interferometer consisting of non-identical antennas each providing orthogonal outputs. The polarization ellipses of the opposite hands have the same orientation for both antennas (see figure (3.3)) as a worst case example. . 56

3.7 Instrumental polarization resulting from an interferometer consisting of two identical antennas each providing non-orthogonal outputs. The two antenna outputs correspond to elliptical polarizations having opposite senses of rotation. Four traces for the difference in orientation of the major axes of the polarization ellipses are shown. (See the right drawing of figure (3.3)) 57
3.8 A flow diagram of the data collection and telescope calibration steps. The subroutine XPOL_SOL is based on the development described in this thesis. 66
3.9 Application of calibration coefficients to the data. The subroutines X_APPLY and POLPHASE were developed as part of this thesis. The majority of the other subroutines depicted were modified to accommodate polarimetry. 67
3.10 A sample of cross-polar coefficients specifying coupling from the RHCP to LHCP channel. 72
3.11 A sample set of cross-polar coefficients specifying the coupling from LHCP to RHCP channels. The coupling for antenna 7, the polarization reference antenna, is set to zero. 73
3.12 Phase of the cross-polar coefficients specifying coupling from the RHCP to LHCP channel. 74
3.13 Phase of the cross-polar coefficients specifying coupling from LHCP to RHCP channels. 75
3.14 Channel gain amplitude for sample baselines. 76
3.15 Channel gain amplitudes for sample baselines. 77
3.16 Channel phases for sample baselines. 78
3.17 Channel phases for sample baselines. 79
3.18 The phase difference between the RHCP and LHCP channels for four sample baselines. Antenna 5 is the phase reference and has been set to zero. 80
3.19 The cross-polar reference phase over approximately one year. Distinct night and day observations were selected. 81
3.20 Test observation of source 3c380. The polarization calibration was disabled for the lower two boxes. Contour levels are given in units of mJy/beam. 82
3.21 Test observation of polarized source 3c138. Contour levels are given in units of mJy/beam. 83
3.22 A plot of the orthogonality between opposite hand channels of three selected antennas. The best and worst are represented here. 84

4.1 A cross section diagram of the feed antenna. The waveguide section which includes the $\lambda/4$ plate and output probes is also shown. 89
4.2 A schematic representation of the measuring system. The antenna range co-ordinates are shown above the turn-table and the AUT is placed at the origin of this system. The spherical co-ordinates, θ and ϕ refer to the antenna radiation pattern. 96

4.3 A plan view of the antenna range. 96
4.4 Photo of the antenna range (top) and the probe (bottom). 97
4.5 Photo of a DRAO feed antenna being lowered onto the turn-table of the range for testing (top) and of the calibration antenna in place of the AUT during the calibration phase (bottom). 98
4.6 The cross-polarisation gain (normalised to the peak value of the co-polarisation gain) as a function of azimuth angle, θ for feed #7. This plot contains contributions to the polarization by both the feed aperture and waveguide components. 100
4.7 The amplitude of the circular polarization ratio on boresight (electrical) as a function of frequency for the RHCP port. 101
4.8 The amplitude of the circular polarization ratio on boresight (electrical) as a function of frequency for the LHCP port. 102
4.9 The phase of the circular polarization ratio on boresight (electrical) as a function of frequency for the LHCP port. 103
4.10 The phase of the circular polarization ratio on boresight (electrical) as a function of frequency for the RHCP port. 104
4.11 The cross-polarization pattern of the aperture made from vectorially subtracting the boresight cross-polarization from the total pattern. 105
4.12 A plot of the cross-polarization gain for $\phi = 0^{\circ}$ (aperture contribution) superimposed on a corresponding calculated pattern. 106
4.13 The co-polarization gain normalised to its peak value as a function of azimuth angle θ. A calculated pattern is superimposed for comparison. 107
4.14 The phase as measured for the feed antenna. The large excursion is due to the difference between the mechanical axis of rotation and the antenna phase centre. 108
4.15 The residual phase variation after correcting the phase pattern data for the offset of the rotation axis. 109
4.16 The circular polarization ratioof an antenna taken with the setup under two vastly different conditions. The correct calibration was applied to the corresponding data for two of these and mismatched in the third to test the probe calibration method. 110
4.17 The accompanying phase plot for the probe calibration test. 111
4.18 The focus box position in terms of the antenna range co-ordinate, ϕ, (left) and the relation between antenna range co-ordinates and the ST co-ordinates (right). 113

5.1 DA530 as observed with the new ST polarimeter at DRAO. The contours represent total intensity of levels 2, 6, 10, 14, 18, 22, 26, 30, 34, 38, 42, and 46 mJy/beam. The polarization lines are aligned with the electric field and their length represent polarized intensity amplitude such that 10 arcminutes = 80 mJy/beam. 117
5.2 The offset field observation of DA530 as a grey shade map. 126
5.3 Maps of sample regions and corrupted data within DA530 that are used in the polarimeter performance evaluation. 127

5.4 A comparison of linearly polarized flux density between the centred (top) and offset (bottom) fields of the DA530 observations with the DRAO synthesis telescope. 128
5.5 A comparison of polarization vectors between the centred (top) and offset (bottom) fields of DA530 observations with the DRAO synthesis telescope. 129
5.6 Probability density histograms of the position angle difference between centred and offset fields of the DA530 observation using sample set 'A'. 130
5.7 Probability density histograms of the position angle difference between centred and offset fields of the DA530 observation using sample set 'B'. 131
5.8 These figures were extracted from Lalitha et al. (1984). The top plots contain polarization vectors on top of total intensity contours (left) and polarized intensity contours (right). The bottom left is a map of rotation measure across DA530 as determined from the observations at 4.7 GHz by Lalitha et al. (1984) and at 2.7 GHz by Haslam et al.(1980). The bottom right is a plot of the projected magnetic field within DA530. 132
5.9 The top and bottom boxes depict DA530 as observed at DRAO and the VLA respectively. Polarization vectors are superimposed on contours of total intensity. 133

List of Tables

1.1 The specifications of the new upgraded DRAO synthesis telescope pertaining to 1420 MHz continuum facility. 2

2.1 Output products from the frequency conversion process. 40

3.1 The first and second rows consist of the polarization conditions required to result in zero LR and RL products respectively. The column entries represent the three baselines of the three element array. . . . 58

3.2 Sources used for polarimeter calibration. 70

4.1 Polarization orthogonality per antenna in percent. Values based on both telescope calibration with sky data and antenna range measurements are presented. 112

4.2 Percent contamination of the opposite to principal polarization associated with the feed antennas for both sky and laboratory based measurements. 112

5.1 The standard deviation in mJy/beam of the background noise for four sample regions. 120

5.2 A comparison of polarized intensity for selected regions between the centred and offset fields. 121

List of Symbols

(in alphabetical order)

Symbol	Description	Page
AIPS	Astronomical Image Processing System	27
AR	Axial Ratio (see also χ)	18
AUT	Antenna Under Test	
$B(\xi, \eta)$	brightness	13, 26
B	magnetic flux density	4
CLEAN	A deconvolution algorithm for image processing	74
CPRG	Cross-Polar Reference Gain	60, 69
dB	decibel: 1 dB = 20 log (V_R) , where V_R is a voltage ratio	
DRAO	Dominion Radio Astrophysical Observatory	
HA	Hour Angle	
I	intensity (equivalent to Stokes paramater, I)	13, 19
IAU	International Astronomical Union	
IEEE	Institute of Electrical and Electronics Engineers	
IP	Instrumental Polarization	55
IX	instrumentally generated contribution to the cross-polar correlation products due to observation of an unpolarized source	61
l_L	LHCP component in the left hand channel	32
l_R	LHCP component in the right hand channel	32
Jy	the unit Jansky: 1 Jy = 10^{-26} W m^{-2} Hz^{-1}	
LHC (P)	Left Hand Circular (-ly Polarised)	18
MCDB	Main Calibration DataBase	68, 69
NRAO	National Radio Astronomy Observatory	27
PA	Position Angle	23
PDM	Polarization Distortion Matrix	93
PX	instrumentally generated contribution to the cross-polar correlation products due to observation of an polarized source	62
Q	Stokes parameter, Q	19
q	circular polarization ratio	30
RHC (P)	Right Hand Circularly (-ly Polarised)	18
RM	Rotation Measure	4
r_L	RHCP component in the left hand channel	32
r_R	RHCP component in the right hand channel	32
S	power flux density	

S_{ij}	scattering matrix element, (i,j)	35
ST	Synthesis Telescope	
U	Stokes parameter, U	19
u,v,w	visibility co-ordinates	25
V	Stokes parameter, V	19
VLA	Very Large Array (operated by NRAO at Socorro, New Mexico)	
δ	declination *or* various phases as required	
ξ, η	map co-ordinates	25
ϑ	visibility	13
ρ	normalised coherency matrix	12
Γ_{mn}	polarization coherence function	11
Γ	voltage ratio (antenna lab measurements)	91
τ	ellipse tilt	18
χ	angular form of axial ratio (see also *AR*)	18

Chapter 1

Introduction

The aperture synthesis telescope operated by the Dominion Radio Astrophysical Observatory of the Herzberg Institute of Astrophysics has, for about a decade, provided images of the sky at 21 cm wavelengths with a field of view at this wavelength unsurpassed by other synthesis telescopes in the world. The wide field of view and sensitivity to extended emission have secured it a niche in the study of galactic nebulae. The images were based on total intensity emission from sources but provided no information on the polarization properties of this emission. Polarization properties of a radio image provide information on the mechanism of radiation and on the properties of the intervening medium that cannot be obtained with total intensity measurements alone.

A major upgrade programme for the instrument was undertaken from 1989 through to the spring of 1995. In addition to substantial performance enhancements, resulting in greatly improved sensitivity and observing speed, polarimetry and a high resolution spectrometer were added as new capabilities. The telescope became operational, collecting high quality data, in the autumn of 1992 after which time the polarimeter facility was added. Polarimetry became publicly available in late autumn of 1993.

This thesis describes the development of the calibration techniques needed for successful polarimetry with this instrument and presents astronomical tests of its performance.

1.1 The DRAO Synthesis Telescope

The synthesis telescope (hereafter ST) of the Dominion Radio Astrophysical Observatory (DRAO) provides radio images of the sky from simultaneously observed continuum radiation at 408 MHz and 1420 MHz as well as spectral line emission from neutral hydrogen near 1420 MHz.

This instrument has proven well suited to the study of extended radio sources possessing features in the angular size range 5 to 100 arcminute and from 0.2° to 5° at the observation frequencies of 1420 MHz and 408 MHz respectively. This size-resolution range makes the telescope especially suitable for objects within our

number of antennas	7
antenna diameter	9 m
maximum baseline	604 m
minimum baseline	4.3 m
angular resolution	$1.0 \times 1.0 \csc \delta$ arcminute^2
field of view	2.6° to the 20% power level
largest structure adequately sampled	~ 20 arcmin
bandwidth	30 MHz
system temperature	65 K
rms noise at the field centre	0.23 mJy/beam
observing speed	12 periods of 12 hours per field

Table 1.1: The specifications of the new upgraded DRAO synthesis telescope pertaining to 1420 MHz continuum facility.

own galaxy although utility for imaging large extragalactic objects has been demonstrated. Resolution is limited by the synthesized beamwidth which is on the order of 1.0 arcminute at 1420 MHz and 3.5 arcminute at 408 MHz. Observations are limited to sources with declinations greater than 15°.

The present ST consists of an array of seven prime focus reflector antennas, 9 metres in diameter, placed in an east-west line (baseline). Three of these antennas are mounted on carriers that can be precisely positioned on a rail track. The movable antennas in conjunction with the fixed four provide 144 inter-antenna distances (or spacings) which, as discussed in detail in chapter 2, spatially sample an equivalent aperture of diameter equal to the projection of the largest spacing in the direction under observation. The resolution is therefore determined by the largest antenna separation in wavelengths which, in this case, is about 3000 wavelengths at 1420 MHz. The field of view, on the other hand, is determined by the reception (radiation) pattern of the individual elements which in turn is a function of their diameter. A trade-off exists between increasing antenna collecting area, which improves sensitivity, and a decrease in field size. The published specifications of the DRAO ST are listed in table (1.1).

The polarization of an electromagnetic wave is described by decomposing the electric field vector into two orthogonal components and the telescope must be capable of independently measuring both of these in order to function as a polarimeter. Chapter 2 on the theoretical background discusses the selection of these components in general, but the selection of right and left circular for the instrument polarization components is not only convenient, but was imposed by the design of the existing telescope before polarization was attempted. The polarization components chosen for the observation are not necessarily the most convenient in which to represent the physical properties of the radiation. Radiation from astrophysical sources, as discussed in the next section, is linearly polarized so that representation of such radiation in the form of linear components is desired. Radiation from astrophysical sources is generated from an ensemble of independent sources and is therefore statistical in nature. Such radiation may be partially polarized so that both the

fraction of polarization and the position angle of the electric field vector of the linearly polarized part must be provided in order to characterize this radiation. Polarimetry with this instrument entails simultaneously collecting both right and left circularly polarized components of the incoming radiation and than combining these data to express the polarization in terms of the more physically meaningful fraction of polarization and position angle.

1.2 Astrophysical Implications of Polarimetry

The DRAO polarimeter will be concerned with polarized continuum radiation at 1420 MHz. Synchrotron radiation with high Lorentz factor (greater than 1000) charged particles is the most likely source of such radiation. The degree of polarization and position angle of such radiation can yield information on the magnetic field structure associated with the source.

Synchrotron radiation is generated by an ensemble of highly energetic charged particles (hereafter considered to be electrons) each of which propagates along a helical path whose axis is parallel to a prevalent magnetic field. The angle between an electron trajectory and the magnetic field vector is referred to as the pitch angle. Radiation generated by an individual electron (with high Lorentz factor) under these conditions is elliptically polarized with electric field maximum perpendicular to the projection of the magnetic transverse to the line of sight.

For an ensemble of electrons that is isotropic, homogeneous and with a uniform distribution of pitch angles in a uniform magnetic field, the polarization will be linear with fraction of polarization and spectral index dependent on the energy distribution (electron spectral index) of these electrons. The position angle of the partially polarized radiation will be determined by the magnetic field direction as in the case of a single electron. If the electron distribution as a function of energy, E, is given (see Verschuur and Kellermann (1988)) by

$$N(E)\,dE = N_o E^{-p} dE$$

the intensity of the observed radiation as a function of frequency, ν, will have a power law distribution,

$$I(\nu) \propto \nu^{\alpha} \tag{1.1}$$

where, $p = 1 - 2\alpha$, and the fraction of polarization, m_p, is

$$m_p = \frac{p+1}{p+\frac{7}{3}} \tag{1.2}$$

The fraction of polarization is $m \simeq 0.7$ for typical values of $2 \leq p \leq 4$.

Equations (5.1) and (5.5) together provide information on the electron energy distribution of the source. The spectral index from (5.1) is $-0.5 \leq \alpha \leq -1.5$. The spectral index alone is often used to distinguish synchrotron radiation from the other prevalent source of radio continuum emission, emission from thermal plasma

sources. If a plasma is optically thin (the usual case) it exhibits a spectral index of $\alpha \sim 0.1$.

Polarimetry offers another discriminator between emission from a plasma (thermal emission) and syncrotron emission (non-thermal emission). Thermal emission arises from electron-ion interactions in the plasma. Thermal continuum emission is generated when the electron does not enter a bound state. This is the free-free emission, in contrast with the bound-bound emission, the latter of which is also characterized as spectral line emission. Thermal emission is completely unpolarized.

The spectral index may be subject to ambiguity due to complications, for example, synchrotron self-absorption or a mix of thermal and non-thermal emission. The fraction of polarization may be influenced by Faraday depolarization. Hence both spectral index and fraction of polarization taken together provide more reliable information than either alone.

The intrinsic position angle is the orientation of the electric field vector of the linearly polarized component of the wave *at the source*. The field vector will be perpendicular to the projection of the magnetic field of the source in the direction of the observer and therefore provides a means to map the internal field of the source. However the position angle is subject to Faraday rotation and the observed degree of polarization differs from the intrinsic value as a result of depolarization. This depolarization results from non-uniform rotation measure between the emitting region of the source and the observer. Specific cases of this depolarization mechanism will be discussed further on.

The electric field vector of a linearly polarized wave propagating through a magneto-ionic medium will undergo a rotation (Faraday rotation) of ψ according to

$$\psi = RM\ \lambda^2 \tag{1.3}$$

where the rotation measure, RM, is given by

$$RM = 8.1 \times 10^5 \int n_e B_\parallel dL \quad \left[\text{rad m}^{-2}\right] \tag{1.4}$$

where, $B_\parallel$, is the magnetic field component (in Gauss) parallel to the direction of propagation and n_e is the density of free electrons (in cm^{-3}) in the medium. Equation (1.4) applies to a non-emitting region, that is a region of space containing only non-relativistic, free electrons.

A priori knowledge of the electron density, magnetic field and distance through the medium (i.e. known rotation measure) allows calculation of the intrinsic position angle from the observed value. Knowledge of these parameters is usually insufficient and the rotation measure must be deduced from a multiple frequency measurement of position angle. For large rotations (such as those of low frequencies) an ambiguity exists that requires measurements at a minimum of three frequencies. Error in the estimation of RM can be minimized through use of higher frequencies provided the source is bright enough for observation at these frequencies. Frequently quoted values for the galactic electron density and magnetic field magnitude are 0.03 cm^{-3} and 3 μG. The resulting rotation measure is $76.5 \times 10^{-3} L$ rad m^{-2} where L is in parsecs. This implies that a 180° rotation of the position angle occurs after

propagation through 1000 pc of the galactic medium at 1420 MHz and that position angles associated with objects further than this, under these conditions, will be subject to the $n\pi$ ambiguity. The RM in the line of sight to an object can sometimes be established by combining observations of the source at more than one frequency, with perhaps, a number of different instruments.

The type of observation determines whether Faraday rotation is a hindrance or a valuable tool. On the negative side rotation must be accounted for in efforts to map the magnetic field of the source itself and depolarization reduces the amount of observed polarization to work with. Positive aspects of Faraday rotation are

1. Observations of Faraday rotation have proven useful in mapping the magneto-ionic content of our galaxy (Spoelstra (1984), Simard-Normandin et al. (1980)). Observations of rotation imparted to the position angle of partially polarized radiation from point sources yield information on the magnetic field and electron density of the interstellar medium.

2. Depolarization provides information on the scale size of unresolved magnetic and electron density fluctuations in the source and intervening medium providing that such depolarization is not excessive (a problem at low frequencies).

Faraday rotation can result in depolarization or at least to a reduction of the measured polarized intensity by one or all of the following mechanisms.

1. Faraday rotation within the source will lead to a superposition of different polarization vectors. The net radiation emerging from the source has a smaller degree of polarization than expected from a given energy distribution.

2. Different lines of sight are observed together in a finite beamwidth. Differences in Faraday rotation for each line of sight result in a reduction of the measured polarization when integrated over the beam of the telescope. This effect can be minimized by decreasing the beamwidth of the telescope.

3. Faraday rotation is a function of frequency. Hence observations over a finite bandwidth will again lead to a superposition of different polarization vectors and resulting decrease of the fraction of polarization. This effect can be minimized by observation over a smaller bandwidth.

Depolarization described in the latter two points is instrument dependent. Beamwidth depolarization (point (2) above) is a limitation of instruments with low resolution. Extended objects with small scale polarization structure may exhibit significantly higher levels of polarization when observed with instruments of higher resolution.

Depolarization across the receiver band (point 3) is given by Gardner and Whiteoak (1966) as

$$m_o = m_i \frac{\sin(\Delta\psi)}{\Delta\psi}$$

where m_o is the observed fraction and the differential rotation across the receiver bandwidth, $\Delta\nu$, is found from

$$\Delta\psi = -RM\lambda_o^2 \frac{2\Delta\nu}{\nu_o}$$

For illustrative purposes a rotation measure of 0.0045 rad MHz^{-1} is calculated for 1420 MHz over the 1000 pc path length and rotation measure considered earlier. For the maximum bandwidth available with the DRAO telescope, 30 MHz, this effect results in a 2% reduction of the observed polarized radiation level. This is not considered a serious error. In cases where RM is much greater, and providing the object is bright enough, bandwidth depolarization can be overcome by observing with a decreased bandwidth.

1.3 The Technical Challenge

Assumptions made regarding the polarization of the instrument are, in reality approximations, so that a process of calibration is require before polarimetry can be successfully achieved. Calibration techniques are unique to each instrument. This telescope is the only synthesis array that employs circularly polarized antennas on equatorial mounts with the consequence that calibration techniques developed for other facilities cannot be applied. Specific problems are

1. the equatorial antenna mounts assure by design that the radiation patterns of the antennas remain fixed to the sky,
2. no rotation of the antenna feed systems is possible and
3. the antenna feed systems are of unknown polarization due to the fact that this instrument was not originally designed as a polarimeter.

Models of the instrument are developed both from theory (chapter 2), and on the basis of laboratory measurements (chapter 4), and used as a basis for calibration techniques (chapter 3) applied to the telescope. The calibrated instrument was tested by an astronomical observation of an object with known polarization properties. The results are presented in chapters 3 and 5.

Chapter 2

Instrument Description and Models

This chapter reviews the background theory, and introduces the key issues addressed in implementing the objective of this thesis. The formation of images at radio wavelengths by the technique of aperture synthesis is a mature field in that basic principles are well established and that standards (albeit de facto in most cases) exist for the design of much of the associated hardware and software. These principles will be reviewed in the section on aperture synthesis and polarimetry. Moreover, some of the notation and concepts that will be employed in the remainder of this work will be introduced here. There are some aspects of the instrument design that are unique to each installation. The section on instrument description and models will consider problems unique to the instrument at DRAO.

The performance of a polarization transducer, an essential component of any polarimeter, is analysed in a novel way, by analogy to the directional coupler. It is demonstrated that if the transducer is matched and lossless, then it exhibits perfect orthogonality, and an interferometer using such devices can measure polarized intensity without special calibration techniques. However, in practice, polarization transducers, although low in ohmic losses, exhibit mismatch losses and a polarization interferometer will require calibration, using techniques such as those described in succeeding chapters. The directional coupler model allows simple modelling of the non-ideal response of the transducer.

2.1 Aperture Synthesis and Polarimetry

A review of the properties of the incoming radiation and its source will establish some of the basic notation used in subsequent chapters and will identify the polarization coherency matrix as the basic observable on which the process of polarized image formation is based. Assumptions made regarding the radiation incident upon the instrument are based on physically reasonable conditions under which the radiation is observed and which are necessary to allow a tractable mathematical description of the underlying operation to be formulated and to limit discussion to a realisable

instrument. Cases that violate these basic assumptions may be accommodated by an existing instrument but analysed outside this archetypal theoretical framework by applying appropriate approximations and corrections on a case by case basis. The radiation from the sources of interest will be of a statistical nature and distributed over a broad range of frequencies. The process of image formation will exploit this property. However, discussion of some aspects of instrument operation, notably with respect to polarimetry, will be simplified by the assumption of monochromatic radiation. The process of generating images containing polarization information given an idealised measurement of the polarization coherence function can be and is described without consideration of specific hardware. Although specific hardware is not considered, the basic geometry of the instrument and the choice of co-ordinate systems, establish some of the fundamental instrument capabilities. Again, without specification of hardware, the concept of instrumental polarization is introduced with the resulting requirement of instrument calibration and subsequent data correction.

2.1.1 Properties of the radiation

Consider an electromagnetic wave propagating in a homogeneous medium free of current sources and charges. Solutions to the wave equation describing this phenomenon are well established in the classic work by Born and Wolf (1959) and more recently by Harrington (1961). Much of the following development and notation is derived from these. The *i'th* component of the electric field vector in a three dimensional co-ordinate system of a propagating wave at a position expressed by position vector, $\mathbf{r}$, can generally be expressed in trigonometric form as

$$E_i^r(\mathbf{r},t) = a(\mathbf{r},t)\cos\left(2\pi\nu t - g(\mathbf{r},t)\right) \tag{2.1}$$

where ν is a constant representing frequency and the superscript r designates this as a real function. The functions a and g have been made functions of time as well as space to allow for application of the quasi-monochromatic condition later. The argument of the cosine function is referred to as the phase of the wave. The following discussion will assume that radiation is in the form of a plane wave, that is to say, that radiation propagates in a manner where there is a constant phase plane of infinite extent (which in practice means as large as necessary) that is perpendicular to the direction of propagation and at any instant in time the electric field vector can be decomposed into two orthogonal vectors within this plane. Alternatively, if thought of in the form of rays emanating from any point of the source under observation and terminating on extreme elements of the instrument, these rays appear parallel to a good approximation. This approximation is met in practice (from Thompson et al. (1986)) when

$$R_s >> \frac{D^2}{\lambda} \tag{2.2}$$

where R_s is the distance to the source, D is the length of the instrument and λ is the operating wavelength. This condition is violated only for observations within the solar system and with extreme size and wavelength combinations of existing

earthbound instruments. This applies to a very small fraction of radiotelescope observations and such observations can be accommodated with application of a suitable correction factor if the distance is known a priori (Thompson et al. (1986)). The concept of wave polarization is valid for non-planar waves and measurements of wave polarization are routinely performed with laboratory instruments, but in the case of an interferometric polarimeter of the type under consideration here, no analysis is known to the author. This condition is considered a special case, beyond the scope of this thesis, and the plane wave (i.e. far field) assumption stands. Equation (2.1) is modified to

$$E_i^r(\mathbf{r},t) = a_i(t)\cos(2\pi\nu t - \mathbf{k}\bullet\mathbf{r} + \alpha_i(t)) \tag{2.3}$$

where $\mathbf{r}$ is the propagation vector in the direction of propagation (the magnitude commonly referred to as the wave number in the free space case). No restrictions have thus far been placed on the time varying amplitude and phase functions α and a ; ν is simply a constant with no physical meaning. If these functions are made constants then equation (2.3) describes the routinely discussed monochromatic plane wave of frequency, ν, and the functions respectively become the wave amplitude and phase constant. A quasi-monochromatic field is said to exist when these functions are allowed to vary very slowly with time as compared to the reciprocal of ν. The field then retains its cosine-like form with a frequency ν but allows the description of statistical radiation within certain spectral limits. The concept of statistical, quasi-monochromatic radiation will be employed throughout the remainder of this thesis and elaborated upon further.

The analytic signal representation is a generalisation of phasor representation for sinusoidal (monochromatic) signals used frequently in engineering and will be used extensively in subsequent discussions. This representation not only results in significant convenience but the notation will be consistent with many other publications on the subject of coherence theory. If E^r represents the real function, then a complex analytic signal, E may be formed by

$$E(\mathbf{r},t) = E^r(\mathbf{r},t) + E^i(\mathbf{r},t) \tag{2.4}$$

where E^i is the Hilbert transform of E^r. Further details on the Hilbert transform are found in Beran and Parrent (1964). The real function must possess a Fourier transform if it is to be specified in analytic form, a sufficient condition for the existence of which is that the time domain signal, $V(t)$, be of finite energy. Thus,

$$\int_{-\infty}^{\infty} |V(t)|^2\, dt < \infty \tag{2.5}$$

It is assumed at this point that signals in all following discussions will be of this type and hence amenable to representation in this fashion. Expressing (2.3) in this form yields

$$E_i(\mathbf{r},t) = a_i(t)e^{\pm j(2\pi\nu t - \mathbf{k}\bullet\mathbf{r} + \alpha_i(t))} \tag{2.6}$$

The wave formulation of equation (2.3) is represented by using either $+\nu t$ or $-\nu t$ as arguments for the exponential function of (2.6), the former of which will be adopted in this thesis.

Consider the radiation which results if $a(t)$ and $\alpha(t)$ are allowed to vary slowly (to maintain the quasi-monochromatic approximation) in a random manner such that the field at two sample points designated by $\mathbf{r}_1$ and $\mathbf{r}_2$ is statistical in nature. Moreover it is assumed that the resulting field is stationary, ergodic and can be described by Gaussian statistics. Such radiation can be completely characterised by the first and second moments (Beran and Parrent(1964)). The first moment or average, A, of statistical signal, V, will be designated by pointed braces, thus

$$A = \langle V(t) \rangle = \lim_{T \to \infty} \frac{1}{2T} \int_{-\infty}^{\infty} V(t) dt \tag{2.7}$$

where $V(t)$ is truncated as $V(t) = 0$ for $|t| > T$ to allow the existence of the Fourier transform as specified for equation (2.5).

A second order moment representing correlation between like electric field components (designated by i) at two different times t and $t - \tau$ at two positions in space $\mathbf{r}_1$, $\mathbf{r}_2$ will be referred to as the *mutual coherence function* and expressed as

$$\Gamma(\mathbf{r}, \tau) = \langle E_i(\mathbf{r}_1, t) E_i^*(\mathbf{r}_1 - \mathbf{r}, t - \tau) \rangle \tag{2.8}$$

The assumption of stationarity allows consideration of a time difference as opposed to absolute times. Likewise, the correlation is dependent on differences in position of the sample points, as opposed to their absolute positions since the radiation is in the form of a plane wave (the constant phase plane is infinite in extent). The Fourier transform of the analytic field contains only positive frequencies and a quasi-monochromatic field has frequencies contained within a small band, $2\Delta\nu$ wide centred around some mean frequency, ν_o. The quasi-monochromatic assumption is valid (Beran and Parrent (1964)) for the condition

$$\Delta\nu \, |\tau| << 1 \tag{2.9}$$

The above treatment does not take into account the vector nature of the field. Similar correlations can be defined between two orthogonal field components that define the wave polarization and lie in a plane perpendicular to the wave propagation. Consider the plane wave of equation (2.8) as a vector. Thus

$$\mathbf{E} = \sum_{i=1}^{3} \hat{\mathbf{u}}_i E_i(\mathbf{r}, t) \tag{2.10}$$

where, $\hat{\mathbf{u}}_i$, is the unit vector in an arbitrary co-ordinate system. Choosing a co-ordinate system so that the propagation vector is parallel to one of the axes yields

$$\mathbf{E}(\mathbf{r}, t) = E_m(\mathbf{r}, t)\hat{\mathbf{m}} + E_n(\mathbf{r}, t)\hat{\mathbf{n}} \tag{2.11}$$

where $\hat{\mathbf{m}}$ and $\hat{\mathbf{n}}$ are orthogonal unit vectors that may, in general, be complex. That is to say

$$\langle \widehat{\mathbf{m}} \bullet \widehat{\mathbf{m}}^* \rangle = 1 \qquad \langle \widehat{\mathbf{n}} \bullet \widehat{\mathbf{n}}^* \rangle = 1 \qquad \langle \widehat{\mathbf{m}} \bullet \widehat{\mathbf{n}}^* \rangle = 0 \tag{2.12}$$

Ko (1967) introduced the polarization coherence function which can be obtained by applying (2.8) to equation (2.11). Thus

$$\Gamma_{mn}(\mathbf{r}, \tau_0) = \langle E_m(\mathbf{r}_1, t) E_n^*(\mathbf{r}_1 - \mathbf{r}, t - \tau_0) \rangle \tag{2.13}$$

Hence four independent field correlations may be performed between any two points in space. The coherency matrix introduced by Born and Wolf (1959) can be derived by considering equation (2.13) with $\mathbf{r} = \mathbf{0}$, $\tau_0 = 0$. It is multiplied by a factor to convert the square of field strength (Volts^2 /metre^2 in mks units) to units of power per unit area as employed in the paper by Ko (1962). The elements of the matrix are the time autocorrelation functions of the radiation at a single point in space for each of the vector component products. Thus,

$$\rho' = \frac{1}{2Z_0} \begin{bmatrix} \langle E_m E_m^* \rangle & \langle E_m E_n^* \rangle \\ \langle E_n E_m^* \rangle & \langle E_n E_n^* \rangle \end{bmatrix} \tag{2.14}$$

The coherency matrix completely specifies the polarization of the radiation and the polarization coherence function is an extension to correlation between two points in space. Generally speaking the polarization coherence function of (2.13) is the basic observable on which the imaging and polarimetry described in the next section are based. The function is an ideal abstraction that is observed with an imperfect instrument. The calibration and subsequent correction of the instrument response to the incident field must be applied before these idealised quantities can be recorded.

The power flux density is defined for a periodic field as the time average of the Poynting vector over a single period (IEEE (1977)). For a wave of constant amplitude a, as in equation (2.1),

$$S = \frac{1}{T} \int_0^T \frac{|E_i^r(\mathbf{r}, t)|^2}{Z_0} dt \tag{2.15}$$

which yields

$$S = \frac{1}{2Z_0} a_i^2(\mathbf{r}) \tag{2.16}$$

where Z_o is the characteristic impedance of free space (377 Ohm in mks units) and the subscript i now refers to one of the two orthogonal co-ordinates m or n. For the quasi-monochromatic analytic signal of equation (2.6), the amplitude is complex and is a random function of time with Gaussian statistics and so the power flux density becomes

$$S = \frac{1}{2Z_0} \langle a_i(\mathbf{r}, t) a_i^*(\mathbf{r}, t) \rangle \tag{2.17}$$

Omitting the frequency ($2\pi\nu$) and spatial ($\widehat{\mathbf{k}} \bullet \widehat{\mathbf{r}}$) phase terms, equation (2.17) above is identical to the principal diagonal elements of the coherency matrix with i

replaced by m and n respectively. Since m and n represent orthogonal field components the sum of these elements is the total power flux density of the plane wave in question.

The coherency matrix of (2.14) may be normalised with respect to the total power flux density. Thus

$$\rho = \frac{\rho'}{S} \tag{2.18}$$

is the normalised coherency matrix as employed in Ko (1962). This quantity will hereafter be referred to as the coherency matrix (the normalisation implied). This matrix has the following properties:

$$\begin{aligned} \rho_{11} &\geq 0 \qquad \rho_{22} \geq 0 \\ \rho_{11} + \rho_{22} &= 1 \qquad \rho_{12} = \rho_{21}^* \end{aligned} \tag{2.19}$$

$$\rho_{11}\rho_{22} - \rho_{12}\rho_{21} \geq 0 \tag{2.20}$$

The principal diagonal elements are real, positive and must sum to unity. The matrix is Hermitian ($\rho_{12} = \rho_{21}^*$) so that (2.20) consists of real terms and is simply the determinant of the matrix. The equality occurs only for a completely polarized wave, that is to say, a wave that either has all of its power in one of the components (one of the principal diagonal elements), or if present in both components, the fields are completely correlated. Otherwise the wave is said to be partially polarized. An unpolarized wave is one where the power is equally represented in both components and the fields are completely uncorrelated, i.e. $\rho_{11} = \rho_{22} = \frac{1}{2}$ and $\rho_{12} = \rho_{21} = 0$. The concept of wave polarization will be expanded upon later in this section.

The power in this case refers to the total power within the band of frequencies for which the radiation exists. Since the range of existence and the range over which the quasi-monochromatic wave assumption is valid will in general differ some confusion may result over the interpretation of total power flux density as expressed in (2.17). Moreover, the valid frequency range of the quasi-monochromatic approximation is a function of the physical geometry involved and of the instrumentation. To limit the observed quantities to properties of the radiation field the concept of spectral power flux density, which is the power flux density expressed on a per unit frequency basis, is introduced. The total power flux density is the integral over frequency of the spectral power flux density. The terminology will be simplified (down to a single word at least) when the quantity of intensity (the spectral power flux density per unit solid angle) is adopted for discussing interferometry. For the remaining discussion mks units will be employed. The spectral power flux density will be expressed in units of W m^{-2} Hz^{-1} and the intensity in W m^{-2} Hz^{-1} sr^{-1}. The unit *Jansky* (1 Jy $= 10^{-26}$ W m^{-2} Hz^{-1}) will frequently be employed because the spectral power flux density of radiation encountered on Earth from astronomical sources will typically be on the order of *milliJanskys* (mJy).

2.1.2 Interferometry and aperture synthesis

Polarization interferometry is the measurement of the polarization coherence function of equation (2.13). Aperture synthesis is the process of forming images from the output of the interferometer.

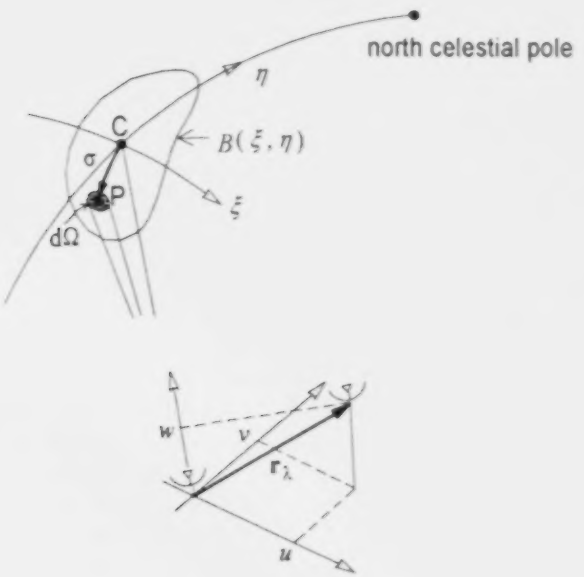

Figure 2.1: Geometrical relationship between a celestial source and the synthesis telescope.

Polarization interferometry entails sampling the electric field at two points separated by the position vector, $\mathbf{r}$, and forming the four correlations between the field vector components. The absolute positions of the sample points are unimportant and only the vector difference between them (i.e. $\mathbf{r}$) needs to be considered as the radiation is assumed to be planar and stationary in space.

The objective of aperture synthesis is to *map* (i.e. display as a function of position variables on the celestial sphere, or, in short, the 'sky') quantities referred to as *brightness* and *polarization* of a celestial source. This information can be obtained by performing a Fourier transform operation on the polarization coherence function as evaluated for a number of $\mathbf{r}$ samples. The term *visibility*, designated by ϑ, will hereafter refer to a special case of the polarization coherence function of equation (2.13) where the delay, τ_o, is set to zero. Thus,

$$\vartheta_{mn} = 2\Gamma_{mn}(\mathbf{r},0)$$

The factor of 2 is included to equate visibility and total intensity for correlation performed between like polarization components (i.e. $m = n$) in the case of unpo-

larized radiation. *Brightness* will refer to the intensity of radiation that emanates from the celestial sphere and *intensity* to the spectral power flux density per unit solid angle (as defined earlier). The solid angle in this case is equivalent to an area of the celestial sphere.

A Fourier transform relation exists between the brightness and visibility. Defining a reference point on the sky as the *reference phase centre*, (C in figure (2.1) this relation allows recovery of the brightness distribution as a function of a vector displacement, $\boldsymbol{\sigma}$, about this point (i.e. vector difference of points C and P) given the visibility for a set of vectors, $\mathbf{r}$. This relationship between brightness, B , and visibility may be expressed as

$$\vartheta_{mn}(\mathbf{r}_\lambda) = 2\int_{4\pi} A_{N_{mn}}(\boldsymbol{\sigma})\,\rho_{mn}(\boldsymbol{\sigma})B(\boldsymbol{\sigma})e^{-j2\pi(\mathbf{r}_\lambda\bullet\boldsymbol{\sigma})}d\Omega \qquad (2.21)$$

where the subscript, λ, indicates measurement in terms of wavelength at the mean frequency of the quasi-monochromatic radiation. The minus sign associated with the exponential kernel of the integral will be used in this thesis to indicate the forward transform. Integration is performed over the celestial sphere with elemental solid angle, $d\Omega$, and $\boldsymbol{\sigma}$ is specified in terms of direction cosines or the associated angles of a spherical co-ordinate system. If the brightness is specified in units consistent with intensity (i.e. Jy per steradian) then (2.21) yields units of spectral power flux density (Jy) for the visibility. The factor A_N is the interferometer element response and is introduced here in anticipation of further discussion. Although primarily representing the antennas this factor takes into account any instrument characteristics that are a function of position on the map plane (that is to say relative to the phase reference centre). It is presented in a somewhat idealised form here as the element response may also be a function of other variables for, example, absolute position on the sky (i.e. declination and hour angle), time and frequency. The coherency matrix, ρ, appears as a function of sky position to impart polarization information to the brightness distribution.

This operation is similar to the formation of an image in the focal plane of a large-aperture optical system. In this case, an imaginary aperture is synthesised by the sample set of spacing vectors, $\mathbf{r}$, hence the term aperture synthesis. These vectors need not be sampled simultaneously since the radiation is also stationary in time.

This Fourier transform relationship between brightness and visibility can be demonstrated by invoking the Van Cittert-Zernike theorem. A statement of the Van Cittert-Zernike theorem is that the mutual coherence function as measured over a plane is the Fourier transform of the brightness distribution of the source. Thompson, Moran and Swenson (1986) present an almost identical derivation to that of Born and Wolf (1959) but with slightly different co-ordinates for compatibility with current practices in radio astronomy (basically assuming the opposite direction for the propagation of the observed radiation). Detailed dissertations on the Fourier transform can be found in a variety of texts, notably that by Bracewell (1978). The inherent assumptions involved in deriving this relationship in this manner are the following.

1. The radiation is in the far field of the source (i.e. planar) as specified previously.

2. The source is incoherent. An incoherent source is one where the radiation at some infinitesimal distance away from any element within the source is uncorrelated with any other element of the source over the integration time specified. It is demonstrated by Beran and Parrent (1964) that, although rigorous application of this definition is too restrictive mathematically to allow existence of such a source, these difficulties are due to the imposition of mathematical idealisation and can be circumvented by the application of realistic constraints such as the size of the source being large relative to the observation wavelength. For purposes of this thesis, the definition as presented here should be adequate.

3. The source is within the bandwidth pattern of the interferometer. This condition is required by the fact that the Van Cittert-Zernike theorem is based on periodic waveforms, that is to say, radiation that is at least quasi-monochromatic and is met by applying the constraint of (2.9) for quasi-monochromatic radiation. The radiation from extremities of the source suffers a delay relative to that arriving from the phase centre and this delay must be smaller than that associated with a change of period experienced over the available bandwidth. An inverse relationship then exists between the maximum observable field of view and the available bandwidth of the radiation. In practical instruments the field size and bandwidth will be limited by elements of the hardware. Practical design considerations will be elaborated upon later.

Some complications are hidden by the innocuous looking dot product ($\mathbf{r} \bullet \boldsymbol{\sigma}$) in the kernel of the integral in (2.21). The map is expressed with two co-ordinates (over a two dimensional plane tangent to the celestial sphere at the phase centre if direction cosines are used or two angles in the case of a spherical co-ordinate system) while, in general, the spacing vector, $\mathbf{r}$, is specified in three dimensions. The Fourier transform relationship demonstrated by application of the Van Cittert-Zernike theorem can still be used but additional steps in the form of constraints and corrections to the data may be required beyond the Fourier transform in moving between the map and the space containing $\mathbf{r}$. The two dimensional transform can still be used if the instrument is designed so that the spacing vector, $\mathbf{r}$, always lies in a plane (specified by u-v co-ordinates introduced in section 2.2.1) parallel to the map plane. This is physically achieved in the DRAO telescope by having all elements of the array lie in an east-west line as described in section 2.2.1. Details may be found in Thompson (1986).

2.1.3 Polarimetry with a synthesis telescope

Polarimetry with regard to a synthesis telescope is the extraction of vector information about the radiation as a function of sky position. It has already been stated that each spacing vector, $\mathbf{r}$, results in four separate correlations as expressed by the

polarization coherence function of equation (2.13) and that the Fourier transform relates a spectrum of spacing vectors to a product of polarization coherence and brightness over the map of the sky. In principle the inverse Fourier transform of (2.21) will yield the product of brightness distribution and coherency matrix for each point on the map. The radiation is specified by two orthogonal vectors; consequently the principal diagonal elements of the matrix are the (normalised) intensity present in each of the principal polarizations. If the radiation is completely polarized the total intensity can be present in either one or both of these. If some fraction appears in both, then, although the two fields will vary randomly, the power that is common to both principal polarizations will exhibit complete correlation and will be manifest in the cross polarization elements (commonly referred to as the *cross-hand correlation*). This is expressed mathematically by the determinant of the coherency matrix being zero as stated in (2.20). Monochromatic radiation is completely polarized but completely polarized radiation may be either monochromatic or statistical in nature. Radiation is said to be completely unpolarized when identical power is present in the parallel hand elements and no correlation exists between them. Partial polarization refers to intermediate degrees of polarization between completely polarized and unpolarized. Mott (1986) demonstrates that a partially polarized wave may be decomposed into a sum of an unpolarized wave and a completely polarized one and that the coherency matrix may be expressed uniquely as

$$\rho = \rho_{polarized} + \rho_{unpolarized}$$

Moreover, the intensity of the polarized part is given by

$$I_p = I_T \left[(\rho_{mm} + \rho_{nn})^2 - 4 \left\| \rho \right\| \right]^{\frac{1}{2}} \tag{2.22}$$

where I_T is the total flux and the determinant is restated from equation (2.20) as

$$\left\| \rho \right\| = \rho_{mm}\rho_{nn} - \rho_{mn}\rho_{nm}$$

The *fraction of polarization* is given by

$$m_p = \frac{I_p}{I_T} \tag{2.23}$$

Although the polarization coherence function is the quantity sampled by the instrument, its corresponding quantity upon transformation, the coherency matrix, is a complex quantity which is incompatible with the existing mapping process. The fact that the brightness is real is exploited in image processing software of long history. Moreover, a representation of even longer history, the Stokes parameters (introduced later) , is in widespread use by astronomers and provides a convenient representation for polarized radiation in terms of real quantities and expressed in units of brightness. Use of the Stokes parameters for polarization synthesis imaging has the great advantage that, because all the Stokes parameters are real quantities, the same imaging techniques can be applied to each. The coherency matrix can be

represented by the intensity, I, and three additional real quantities, M, C and S (using the notation of Deschamps (1973)) such that

$$\rho = \frac{1}{2I} \begin{bmatrix} I+M & C-jS \\ C+jS & I-M \end{bmatrix} \tag{2.24}$$

where, because of the Hermitian nature of the coherency matrix,

$$C = I\,\mathrm{Re}(\rho_{mn}) = I\,(\rho_{mn} + \rho_{nm}) \tag{2.25}$$

$$S = -I\,\mathrm{Im}(\rho_{mn}) = jI\,(\rho_{mn} - \rho_{nm}) \tag{2.26}$$

$$M = I\,(\rho_{mm} - \rho_{nn}) \tag{2.27}$$

Substitution of (2.24) into equation (2.22) yields

$$I_p = \sqrt{M^2 + S^2 + C^2} \tag{2.28}$$

Thus, although the polarization of the principal elements of the coherency matrix is unspecified, the total polarized intensity can be determined from the four real quantities as described above. Physical interpretation of these quantities depends on the choice of principal polarization vectors, $\mathbf{m}$ and $\mathbf{n}$.

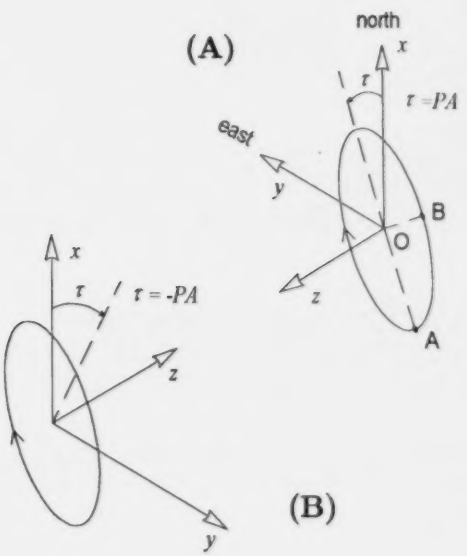

Figure 2.2: Relationship between the co-ordinate system describing the polarization of the source (A) and the ground based co-ordinate system describing the synthesis telescope (B).

A right-handed, rectangular co-ordinate system is traditionally employed to describe the polarization of a wave in physically meaningful terms. Consider the plane wave of equation (2.6) propagating in the $+z$ direction of the co-ordinate system depicted in figure (2.2a). The propagation term, $\mathbf{r} \bullet \mathbf{k}$ becomes kz and equation (2.6) becomes

$$\mathbf{E}(z,t) = \left[a_x(t)e^{j\alpha_x(t)}\hat{\mathbf{u}}_x + a_y(t)e^{j\alpha_y(t)}\hat{\mathbf{u}}_y\right] e^{j(2\pi\nu t - kz)} \tag{2.29}$$

The amplitudes of the two components are constants in the case of a monochromatic wave or a quasi-monochromatic wave over a short period of time. It is shown in detail by Kraus (1986), Mott (1986) and many other treatments on the subject that, in general, the tip of the electric vector of a monochromatic wave traces out an ellipse in the plane perpendicular to the direction of propagation as the wave travels forward. The quantity τ is the tilt of the polarization ellipse (see figure (2.2a)) and χ represents the axial ratio. The definition of axial ratio, AR, as adopted by Kraus (1986) is

$$AR = \frac{\text{major axis}}{\text{minor axis}} = \frac{OA}{OB}, \qquad 1 \leq |AR| \leq \infty \tag{2.30}$$

and

$$\chi = \cot^{-1}(AR), \qquad -45^\circ \leq \chi \leq 45^\circ \tag{2.31}$$

with negative values of axial ratio indicating right hand elliptical polarization and positive values indicating left hand elliptical polarization. Alternatively Mott (1986) provides a detailed derivation of AR as a function of the component amplitudes and their phase difference. Thus,

$$\sin(2\chi) = AR = \frac{2a_x a_y}{a_x^2 + a_y^2}\sin(\alpha_y - \alpha_x) \tag{2.32}$$

where in this case $-1 \leq AR \leq +1$. The sign of AR and χ is in agreement with that of Kraus (1986). The sign of the axial ratio is arbitrary although believed by the author to be consistent with most of the established literature on the subject. The left and right designations define the sense of rotation of the electric field vector in the polarization ellipse. Although arbitrary in principle the definition of rotation sense conforms to the IEEE definition whereby the vector for a left hand wave rotates in a counterclockwise direction when viewed in the direction of propagation and the corresponding right hand vector rotates clockwise. This definition was adopted for radio astronomy by the IAU (Thompson et al. (1976)) and is the one used here. The vector of a left hand elliptically polarized wave would rotate clockwise in the case of figure (2.2a). Circularly polarized and linearly polarized waves are special cases of elliptical polarization where the axial ratio is -1 (equation (2.32) with $(\alpha_y - \alpha_x) = -90^\circ$) for right hand circular (RHC), +1 for left hand circular (LHC) and zero for linear polarization. The sense of rotation is necessary to fully specify circularly polarized radiation and the tilt to likewise describe linear polarization.

The Poincaré sphere, a graphical representation of wave polarization, can be adapted for used with partially polarized radiation. Polarization for a completely polarized wave is mapped onto the surface of a unit sphere where, 2χ, and twice the ellipse tilt, 2τ, are the latitude and longitude of a point representing a unique polarization state. The equatorial plane of the sphere represents linear polarization while the north and south poles are LHCP and RHCP respectively (using the definitions of equations (2.31) and (2.32)). Orthogonal polarization states are antipodal points on the sphere's surface. The polarized fraction is represented by the distance from the centre (Deschamps (1973)) in the case of partially polarized radiation. The surface of the Poincaré sphere represents the fully polarized state while completely unpolarized radiation is represented by the centre. Moreover, in the case of a lossless transducer (i.e. the intensity is preserved through the device), a change of polarization state as the radiation propagates through the device is represented by a rotation of the sphere. The fraction of polarized intensity remains constant.

The geometry is depicted in figure (2.3). Orthogonal axes j, k and l represent the correlation between the principal polarization components (alias parallel hand or co-polar) components and the real and imaginary component of the cross hand correlations respectively (twice the value of the coherency matrix elements for the unit sphere). Co-ordinates of a unique polarization state within the sphere may also be represented by M, C and S of equation (2.24). The Stokes parameters, Q, U and V refer to M, C and S respectively for the specific co-ordinate system of figure (2.3). The principal diagonal elements of the coherency matrix correspond to the x and y field components and the cross correlation elements to linear polarization with $\tau = 45°$. Letting $m = x$ and $n = y$ in equations (2.25) to (2.27) yields the Stokes parameters in terms of the coherency matrix elements. Thus,

$$\begin{aligned} Q &= M = I\left(\rho_{xx} - \rho_{yy}\right) \\ U &= C = I\left(\rho_{xy} + \rho_{yx}\right) \\ V &= S = jI\left(\rho_{xy} - \rho_{yx}\right) \end{aligned} \tag{2.33}$$

where I is the total intensity and is typically considered to be one of four Stokes parameters. The Stokes parameters can be expressed in terms of the field amplitudes and phases of equation (2.29) by use of equations (2.14) and (2.18). Thus,

$$\begin{aligned} I &= \langle a_x^2 \rangle + \langle a_y^2 \rangle \\ Q &= \langle a_x^2 \rangle - \langle a_y^2 \rangle \\ U &= 2\langle a_x a_y \cos(\alpha_y - \alpha_x) \rangle \\ V &= 2\langle a_x a_y \sin(\alpha_y - \alpha_x) \rangle \end{aligned} \tag{2.34}$$

This is the basic form of the Stokes parameters (based on linearly polarized components) introduced in many established texts on the subject (the earliest referenced in this thesis being Born and Wolf (1959)). Moreover, if propagation is in the $+z$ direction as assumed in the above, these expressions are consistent with

the original paper by G. G. Stokes (1852) on representing partially polarized radiation in this manner. Hence equation (2.34), representing a wave propagating in the $+z$ direction, is considered the definitive form of the Stokes parameters. These parameters are consistent with the definition of axial ratio in equation (2.32) and $0 \leq (\alpha_y - \alpha_x) \leq 90°$ will result in a positive Stokes V corresponding to LHCP (the IRE definition as described earlier). It is noted that Thompson et al. (1986) do not adopt this definition of Stokes parameters with the result that Stokes V is positive for RHCP. This may have been an oversight on the part of the authors.

Stokes parameters expressed in terms of spherical co-ordinates (axial ratio and tilt) of a point on the Poincaré sphere are

$$\begin{aligned} Q &= I \cos 2\chi \cos 2\tau \\ U &= I \cos 2\chi \sin 2\tau \\ V &= I \sin 2\chi \end{aligned} \tag{2.35}$$

The Q and U parameters represent linearly polarized radiation as all the polarized power is present in these if axial ratio, 2χ , and hence V, is zero. In contrast, V is seen to represent circular polarization. Like the elements of the coherency matrix, Stokes parameters are additive for independent waves. For partially polarized radiation, it is physically meaningful to consider the field as being composed of unpolarized, linearly polarized and circularly polarized parts as opposed to a polarized contribution of a given axial ratio and tilt.

Starting with equations (2.28) and (2.33), the fraction of linear, circular, total polarized flux and tilt of the linear polarized radiation can be shown to be

$$\begin{aligned} m_l &= \frac{\sqrt{Q^2 + U^2}}{I} \\ m_c &= \frac{V}{I} \\ m_p &= \frac{\sqrt{Q^2 + U^2 + V^2}}{I} \\ \tau &= \frac{1}{2} \arctan\left(\frac{U}{Q}\right) \qquad 0 \leq \tau \leq \pi \end{aligned} \tag{2.36}$$

respectively. The tilt of the linear radiation electric field vector, τ, can be derived from equation (2.35).

The adoption of x and y directed linear fields for the principal polarizations of the coherency matrix may not always be appropriate. Stokes parameters may be expressed in terms of other principal polarizations providing they meet the criteria of orthogonality. Figure (2.3) depicts the special case where M, C and S are equivalent to the Stokes parameters. In this case the principal elements of the coherency matrix are aligned with the j-axis and the imaginary part of the element corresponding to the xy correlation with the l-axis. Through a series of two rotations the j, k, l axes may be rotated to a new set, designated j', k', l' within the Poincaré sphere.

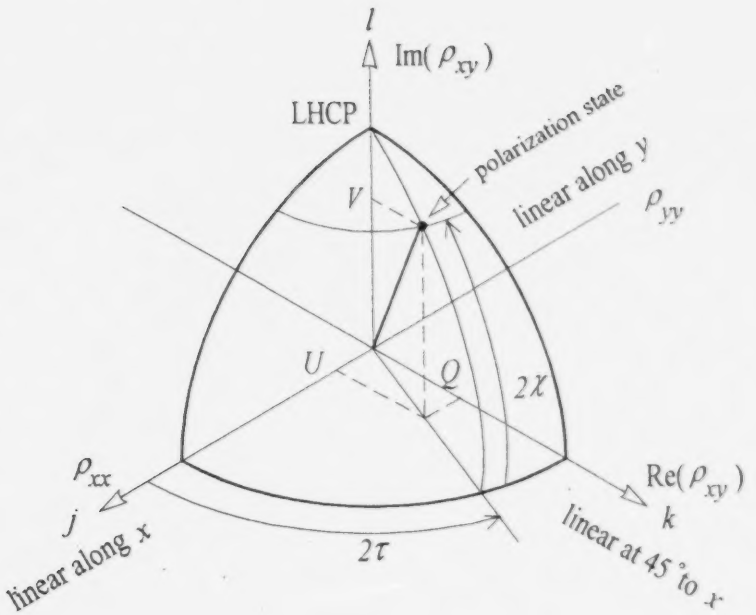

Figure 2.3: The Poincaré sphere and its relation to the Stokes parameters and coherency elements.

The first rotation selects the principal polarizations by arranging the j'-axis to pass through antipodal points on the Poincaré sphere representing two orthogonal polarization states. The second rotation applies a rotation of phase to the cross polarization elements of the coherency matrix thereby selecting a reference for the tilt and axial ratio. The M, C and S co-ordinates will then be expressed in terms of these new polarization states. The rotations can be performed according to

$$\begin{bmatrix} M \\ C \\ S \end{bmatrix} = [\mathbf{F}] \begin{bmatrix} Q \\ U \\ V \end{bmatrix} \tag{2.37}$$

where $\mathbf{F}$ is the Euler angle matrix and is expressed in Mott (1986) as

$$[\mathbf{F}] = \begin{bmatrix} \cos\beta\cos\gamma & \cos\beta\sin\gamma & -\sin\beta \\ \sin\alpha\sin\beta\cos\gamma - \cos\alpha\sin\gamma & \sin\alpha\sin\beta\sin\gamma + \cos\alpha\cos\gamma & \sin\alpha\cos\beta \\ \cos\alpha\sin\beta\cos\gamma + \sin\alpha\sin\gamma & \cos\alpha\sin\beta\sin\gamma - \sin\alpha\cos\gamma & \cos\alpha\cos\beta \end{bmatrix} \tag{2.38}$$

where the angles are measured from one of the j, k, l axes of the original Stokes co-ordinate system to the corresponding axis of the new system. The rotations are performed in the order

1. γ around the l-axis in the direction $j \rightarrow k$
2. β around the k-axis in the direction $l \rightarrow j$ (2.39)
3. α around the j-axis in the direction $k \rightarrow l$

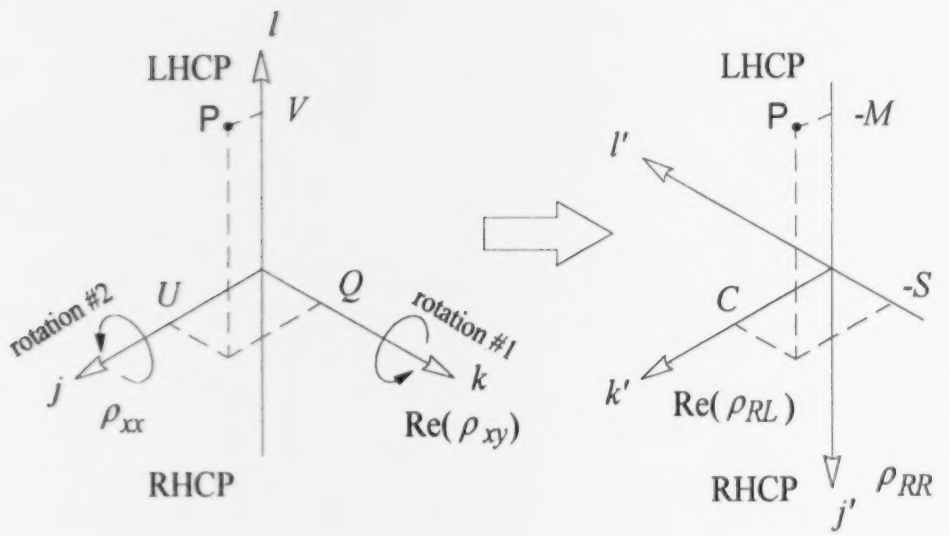

Figure 2.4: The co-ordinate transformation for expressing Stokes parameters in terms of the coherency elements for circularly polarized components.

RHC and LHC are a common principal polarization pair and are adopted here. The first rotation about the k-axis (the second rotation in (2.39)) with $\beta = 90°$ selects RHC and LHC as the principal polarizations by passing the j'-axis through the south pole of the Poincaré sphere. Since the j-axis and j'-axis are still aligned the real part of the element corresponding to the *right-left* correlation still responds to linear polarization at a $\tau = 45°$ tilt to the x-axis of figure (2.2a). A second rotation (the third of (2.39)) with $\alpha = 90°$ selects a new reference for the tilt of the ellipse. The real part of the *right-left* coherency term now responds to a tilt of zero (i.e. along the x-axis). This transformation is depicted in figure (2.4). Expressing the Stokes parameters in terms of the new M, C, S co-ordinates and substituting the elements of the coherency matrix with $m = R$ and $n = L$ in equations (2.25) to (2.27) yields

$$\begin{aligned} Q &= C = I\,(\rho_{RL} + \rho_{LR}) \\ U &= -S = -jI\,(\rho_{RL} - \rho_{LR}) \\ V &= -M = I\,(\rho_{LL} - \rho_{RR}) \end{aligned} \tag{2.40}$$

The above formulations for the Stokes parameters assume that the wave is propagating in the $+z$ direction. The sense of rotation by the IEEE definition is determined by the rotation direction observed while looking in the direction of propagation. Therefore, it follows that an observer receiving this wave will observe a rotation in the opposite direction. The Stokes parameters and coherency matrix elements reflect the behaviour of the principal polarization vectors in a plane so that the change in direction is observed as an apparent change in the sense of rotation. Retaining the labels according to the IEEE convention and, given that the coherency matrix is Hermitian, this change in propagation is manifest in a conjugation of ρ_{RL} and ρ_{LR}. The Stokes U parameter of (2.40) is composed of the sum of the imaginary parts of these elements and as a result becomes

$$U = jI\left(\rho_{RL} - \rho_{LR}\right) \tag{2.41}$$

for a wave propagating in the negative z direction (the receiver at the origin). The coherency matrix can be expressed, from equation (2.36), in terms of the tilt and fraction of linear polarization as

$$\rho_{RL} = \rho_{LR}^{*} = \frac{m_l}{2} e^{j2\tau} \tag{2.42}$$

for propagation in the $+z$ direction and

$$\rho_{RL} = \rho_{LR}^{*} = \frac{m_l}{2} e^{-j2\tau} \tag{2.43}$$

for propagation in the -z direction. It is apparent from the above that linear polarization shows up only as cross-correlation products of the circularly polarized field components and that all information (i.e. fraction of linear polarization and tilt of the electric field vector) regarding the linearly polarized part is obtained from these quantities. By convention the tilt of the electric field vector of the linearly polarized contribution to the radiation is measured from north to east on the sky (see section 2.2.1) and will hereafter be referred to as the *position angle*, PA, in the context of sky radiation. Figure (2.2a) represents this case if the axes are oriented so that the x-axis is directed north and the y-axis is directed east.

The coherency matrix elements may be referenced to a ground based co-ordinate system where radiation propagates toward the observer. In this case, the y-axis is directed west on the Earth's surface, the position angle is related to the tilt of the polarization ellipse by $PA = -\tau$, and the Stokes parameter U is determined from equations (2.43) and (2.41). Figure (2.2b) depicts this system.

The Stokes parameters as a distribution over the sky are equivalent to the product of the brightness and the coherency matrix. The Fourier transform is a linear operation and, by use of the addition theorem in Bracewell (1978), the Stokes parameters as expressed above may be applied to the coherency matrix of equation (2.21) to yield

$$\frac{1}{2}\left(\vartheta_{RR}(\mathbf{r}_\lambda) + \vartheta_{LL}(\mathbf{r}_\lambda)\right) \;=\; \int_{4\pi} A_N\left(\boldsymbol{\sigma}\right) I(\boldsymbol{\sigma}) e^{-j2\pi \mathbf{r}_\lambda \bullet \boldsymbol{\sigma}} d\Omega$$

$$\frac{1}{2}\left(\vartheta_{RL}(\mathbf{r}_\lambda)+\vartheta_{LR}(\mathbf{r}_\lambda)\right) = \int_{4\pi} A_N(\boldsymbol{\sigma})\, Q(\boldsymbol{\sigma}) e^{-j2\pi \mathbf{r}_\lambda \bullet \boldsymbol{\sigma}} d\Omega \qquad (2.44)$$

$$\frac{-j}{2}\left(\vartheta_{RL}(\mathbf{r}_\lambda)-\vartheta_{LR}(\mathbf{r}_\lambda)\right) = \int_{4\pi} A_N(\boldsymbol{\sigma})\, U(\boldsymbol{\sigma}) e^{-j2\pi \mathbf{r}_\lambda \bullet \boldsymbol{\sigma}} d\Omega$$

$$\frac{1}{2}\left(\vartheta_{LL}(\mathbf{r}_\lambda)-\vartheta_{RR}(\mathbf{r}_\lambda)\right) = \int_{4\pi} A_N(\boldsymbol{\sigma})\, V(\boldsymbol{\sigma}) e^{-j2\pi \mathbf{r}_\lambda \bullet \boldsymbol{\sigma}} d\Omega$$

The Stokes U, as given by (2.41), applies to the sky based co-ordinate system of figure (2.2a). The polarization properties of the antenna system as a function of position have been ignored and only the scalar gain considered. That is to say, the antenna pattern term, A_N, is assumed identical for both principal polarizations (in this case LHCP and RHCP). Inversion of the transform will yield a product of the antenna gain and Stokes distributions as obtained from measured visibilities.

The polarimeter provides two levels of information on the polarization state of partially polarized radiation. These are as follows.

1. The polarized intensity can be found by measuring the intensity present in two orthogonal polarization components. These components are arbitrary in that their polarization need not be known in order to make this determination. Orthogonal polarizations are characterised by zero correlation between their respective field components for unpolarized radiation.

2. The characteristics of the polarized portion of the radiation (i.e. sense of rotation, ratio of linear to circular intensities and position angle) can only be determined if the specific polarization of the measured components is known.

2.2 Instrumental Considerations

The visibilities discussed thus far refer directly to the incident radiation as opposed to that which is measured by a real instrument. The response of the real instrument to this radiation will now be considered. A model is constructed that closely resembles the existing instrument at DRAO and deviations between the two (which are variable with time as well as other factors) are dealt with by the application of corrections to the data based on calibration operations. The development of these calibration and correction procedures form most of the work of the remaining thesis. The model and instrument response for which calibration procedures are developed will be presented in this section. The models are instrument specific so that many of the features of the synthesis telescope (ST) at DRAO will now be incorporated into the discussion. However, some of these features are common to other instruments so that the models may be applied to some extent in these cases. The section begins with a specific definition of co-ordinate systems over which the telescope is constructed and that play a part in the operation of the ST. Aspects of the instrument operation will be limited to those pertaining to polarimetry.

2.2.1 Co-ordinate systems and telescope geometry

Five co-ordinate systems will be considered over the course of this thesis. These are

1. the *polarization co-ordinates* which have been discussed in some detail in the previous section,

2. *visibility co-ordinates* (commonly referred to as the *u-v plane*),

3. the *map* (also called *sky*) co-ordinates,

4. the *track* or *antenna co-ordinates* that specify physical locations of the interferometer elements and

5. the *antenna pattern co-ordinates.*

A brief description of each now follows.

The polarization state of the source is described by Stokes parameters as described in the last section. The position angle is, according to IAU convention, measured in the direction from *north to east* on the map co-ordinate system. References made to the coherency matrix or polarization properties of antennas and other system elements will be taken in a ground-based rectangular system as in figure (2.2b) in which the instrument is situated at the origin and receiving radiation propagating in the -z direction. This is also shown as the x, y, z-axis triplet in figure (2.5). The x-axis is directed northward on the sky to retain compatibility with the IAU definition of position angle.

The spacing vector, $\mathbf{r}$ is described by the visibility co-ordinates designated in modern literature by u, v and w. This is a right-handed Cartesian co-ordinate system where u and v lie in a plane perpendicular to the incoming radiation and w points to the phase centre. The visibility phase is measured relative to that for radiation propagating from the direction of the phase centre. A point source located at the phase centre of the map will generate visibilities, for any given $\mathbf{r}$, that have zero phase and an amplitude corresponding to the total power flux density of the radiation associated with this source. A displacement of the source from the phase centre will manifest itself as a phase change in the visibility function. The u and v visibility co-ordinates are parallel to the map co-ordinates, ξ and η, respectively. The map co-ordinates are those over which the brightness map of the source under observation is placed and the origin of the map is coincident with the phase centre. The u and ξ axes point in a west to east direction and the v and η point south to north. Figure (2.1) depicts the relation between these systems. Although the visibility co-ordinates are linear, the map co-ordinates are specified in terms of direction cosines. From figure (2.6) it is seen that that the direction cosine is a projection of the celestial sphere onto a plane that is tangent to the sphere at the phase centre. For small fields of view angular separations between points on the sky are proportional to distance on the map. If the map distances represented by ξ and η have units of radians then the resulting units of u and v will be cycles per radian. This is frequently interpreted as *spatial frequency* since, for a specific choice of u or v , the coherence function will be maximised by a source having a sinusoidal brightness distribution (the fringe pattern) over the sky, the frequency of which is this spatial frequency. Following Thompson et al. (1986), equation (2.21) can be expressed in terms of these co-ordinates by applying the following

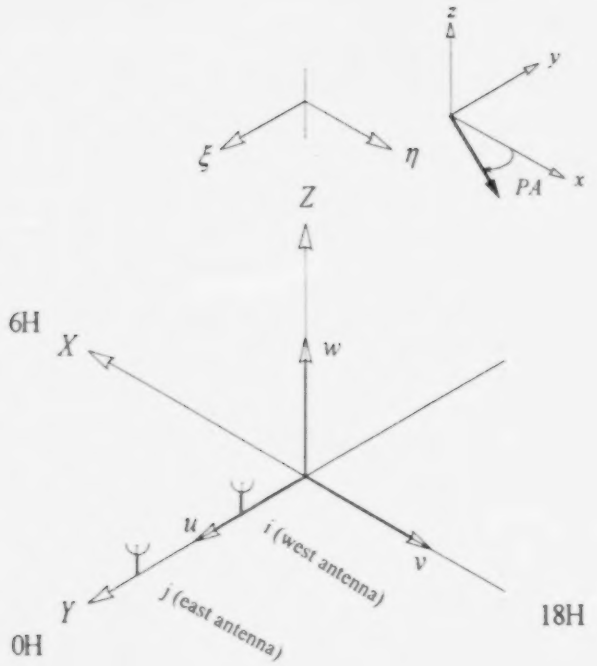

Figure 2.5: Geometrical relationship of the visibility, map, track and polarization co-ordinates. The systems are shown at HA 0 and declination, $\delta = 90°$.

$$\begin{aligned} \mathbf{r}_\lambda \bullet \mathbf{r}_c &= w \\ \mathbf{r}_\lambda \bullet \mathbf{r}_p &= \left(u\xi + v\eta + w\sqrt{1-\xi^2-\eta^2} \right) \\ d\Omega &= \frac{d\xi d\eta}{\sqrt{1-\xi^2-\eta^2}} \end{aligned} \tag{2.45}$$

Thus (2.21) becomes,

$$\begin{aligned} \vartheta_{mn}(u,v,w) &= 2\iiint_{-\infty}^{\infty} A_{N_{mn}}(\xi,\eta)\,\rho_{mn} B(\xi,\eta)\, e^{-j2\pi\left[u\xi+v\eta+w\left(\sqrt{1-\xi^2-\eta^2}-1\right)\right]} \\ &\quad \frac{d\xi d\eta}{\sqrt{1-\xi^2-\eta^2}} \end{aligned} \tag{2.46}$$

The simplicity of the transform is compromised by the non-linear term involving w. However, in the case where baselines form an east-west line on the Earth's surface and w points to the celestial pole (i.e. the phase centre is at the pole), the spacing

vector remains in the u-v plane because there is no component of motion parallel to the rotation axis. The component w is set to zero in (2.45) and the relation is once again restored to a two dimensional transform. Thus

$$\vartheta_{mn}(u,v) = 2\iint_{-\infty}^{\infty} \frac{A_{N_{mn}}(\xi,\eta)}{\sqrt{1-\xi^2-\eta^2}} \rho_{mn} B(\xi,\eta)\, e^{-j2\pi[u\xi+v\eta]} d\xi d\eta \qquad (2.47)$$

The map centre may be moved away from the celestial pole, but if w remains set to zero, the map plane will undergo a predictable distortion along the direction of the η axis. A one-to-one correspondence exists between points on the map plane to points on the u-v plane so that map fidelity can be restored with a suitable co-ordinate transformation applied to the map after the image is formed. Details may be found in Thompson et al. (1986). This reference describes co-ordinate system definitions employed at the VLA (Very Large Array, a synthesis telescope, that is operated by the National Radio Astronomy Observatory (NRAO) of the United States in New Mexico) and within the imaging software system AIPS (for Astronomical Image Processing System). AIPS has become the de facto standard for image processing at aperture synthesis telescopes in general.

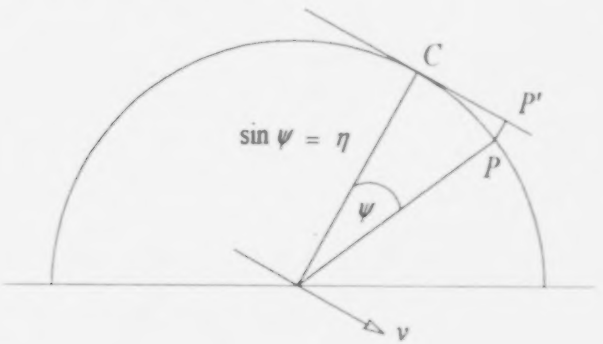

Figure 2.6: Direction cosines and their relation to the celestial sphere.

The third co-ordinate system which will not be considered in great detail here is the *track* or *antenna co-ordinate* system. The u-v plane is sampled in real instruments by fixing a number of receiving elements to an earth or satellite based co-ordinate system and then allowing motion of this platform relative to the visibility co-ordinate system to accomplish the task of sampling. A set of physical distances between elements, or *spacings*, when projected onto the u-v plane, sample the spacing vector, $\mathbf{r}$. The visibility system remains fixed to the sky but the antenna co-ordinate system is dependent on the HA (hour angle) or earth-sky position. Antenna co-ordinate systems vary between installations although many terrestrial ones are at least similar (usually within a rotation of the X-Y plane) to the right-handed cartesian system specified in Thompson (1986) (based on the VLA). This system

is employed here. Designated by X,Y and Z, this co-ordinate system lies in the earth's equatorial plane and is positioned so that the Z-axis points to the celestial north pole and the Y-axis points east. The declination, δ, and hour angle, HA, refer to the position of the phase centre on the sky. The origin of the antenna co-ordinate system is situated at some reference point of the array, usually the element used as a visibility phase reference. The alignment shown in figure (2.5) is a convenient reference position when discussing the instrument response. This occurs when the phase reference centre is at the north celestial pole, (declination, $\delta = 90^{\circ}$) and the HA (in a 24 hr system) is 0 or 24 hr, in which case the Z and Y axes are coincident with the w and u axes respectively. The co-ordinates are related by the transformation matrix

$$\begin{bmatrix} u \\ v \\ w \end{bmatrix} = \begin{bmatrix} \sin H & \cos H & 0 \\ -\sin\delta\cos H & \sin\delta\sin H & \cos\delta \\ \cos\delta\cos H & -\cos\delta\sin H & \sin\delta \end{bmatrix} \begin{bmatrix} X \\ Y \\ Z \end{bmatrix} \tag{2.48}$$

For a series of elements spaced along the Y-axis, it can be demonstrated with the above transformation that, the u-v tracks are a series of concentric ellipses (circles for the special case of a polar source, $\delta = 90^{\circ}$) that form over the 24 hour rotation period of the earth. The set of spacing samples is formed by pairs of elements along the Y-axis and two dimensional u-v plane coverage occurs as a result of rotation of these spacing vectors.

The Fourier transform of a function in the first domain is its complex conjugate reflected about the origin in the second domain (Bracewell (1978)). The product of brightness and the principal diagonal elements of the coherency matrix is a real quantity so that the corresponding transform, the visibility, is simply conjugated for negative spatial frequencies. That is to say,

$$2\rho_{mm}(\xi,\eta)B(\xi,\eta) = \mathcal{f}^{-1}\vartheta_{mm}(u,v) = \mathcal{f}^{-1}\vartheta^{*}_{mm}(-u,-v) \tag{2.49}$$

where, $\mathcal{f}^{-1}$, denotes the inverse transform of (2.21). This property is exploited to generate a map by sampling only one half of the u-v plane, that is, it is necessary to observe for only 12 hours as opposed to 24. The cross-polarized elements of the coherency matrix are in general complex so that

$$2\rho^{*}_{mn}(\xi,\eta)\,B(\xi,\eta) = \mathcal{f}^{-1}\vartheta^{*}_{mn}(-u,-v) \qquad n \neq m \tag{2.50}$$

but since, $p_{mn} = \rho^{*}_{nm}$, equation (2.50) may also be expressed as

$$2\rho_{mn}(\xi,\eta)B(\xi,\eta) = \mathcal{f}^{-1}\vartheta_{mn}(u,v) = \mathcal{f}^{-1}\vartheta^{*}_{nm}(-u,-v) \tag{2.51}$$

so that, outside the sampled HA range, the cross-polarization visibilities must be exchanged between polarizations and, in addition, the conjugate operation must be applied.

The final co-ordinate system specifies the *radiation pattern* of the antenna systems that form each of the elements of the interferometer. The antenna far field pattern is the element response to the oncoming plane wave as a function of antenna

direction. This antenna pattern co-ordinate system may be fixed relative to the visibility co-ordinates, as in the case of a true equatorial mount, or dependent on HA and declination, as for alt-azimuth mounts. There are also intermediate cases, for example in the case of most practical equatorial mounts, where there is a movement of the antenna in the direction of the w axis as the antenna tracks the source even though two of the co-ordinates remain fixed with respect to the u-v plane. The details of antenna patterns will be left for later discussion.

2.2.2 The DRAO synthesis telescope co-ordinate system

The synthesis telescope at DRAO lies along an east-west baseline as described in chapter 1 and adheres to the basic co-ordinate description presented in section 2.2.1. Some details, important to the implementation of polarimetry, are now discussed.

Reduction software at DRAO assumes that the the u-v plane is sampled according to equation (2.48) over an HA range of 18 to 06 Hours. This will hereafter be referred to as the *principal HA range*. In practice, data is observed outside this range, but reordered and conjugated according to equations (2.49) and (2.51) of section 2.2.1. This operation is referred to as *HA range justification*.

The antennas lie along the Y-axis with co-ordinates increasing toward the east when the baseline is in the 0 HA position. The u-axis will be parallel to the Y-axis at this position. In the DRAO baseline numbering scheme, the baselines, designated generally by ij , are numbered according to

$$i = 1, 2 \ldots 6, \quad j = (i+1), (i+2) \ldots 7 \quad i < j, \quad i \neq j$$

and i refers to the *west-most* antenna of the pair. According to the definition adopted for spatial frequency in equation (2.8), the spatial frequency u is given by $u = u_1 - u_2 = Y_1 - Y_2$ where the subscript 1, in this case, refers to the west antenna position and 2 the east. Since $Y_1 < Y_2$, u will be negative. A similar argument holds for v. Thus the visibility co-ordinates for this instrument are negative within the principal HA range, for the co-ordinate system adopted, and negative according to the definitions within AIPS. This point is referred to in section (2.2.8) following a discussion on instrument response and has implications for polarimetric imaging.

2.2.3 Circular polarization ratio

This section digresses somewhat from the topic of coordinate systems to introduce circular polarization components and the related *circular polarization ratio*. These quantities will be referred to in the discussion of instrument models (section 2.2.4) that follow. Later discussion on instrument calibration and on antenna measurements will utilize the concept of circular polarization ratio.

The field amplitudes correspond to components of a total field given by

$$\mathbf{E} = E_L \hat{\mathbf{u}}_L + E_R \hat{\mathbf{u}}_R = E_o (l \hat{\mathbf{u}}_L + r \hat{\mathbf{u}}_R) \tag{2.52}$$

where the unit circular vectors are expressed in terms of the polarization co-ordinates of figure (2.2b) as

$$\hat{\mathbf{u}}_L = \frac{\hat{\mathbf{u}}_x - j\hat{\mathbf{u}}_y}{\sqrt{2}} \tag{2.53}$$

$$\hat{\mathbf{u}}_R = \frac{\hat{\mathbf{u}}_x + j\hat{\mathbf{u}}_y}{\sqrt{2}} \tag{2.54}$$

and $|l|^2 + |r|^2 = 1$.

The polarization of the above wave can be completely described by its *circular polarization ratio* (a special case of polarization ratio; for a general discussion, see Mott (1986)). The circular polarization ratio is defined by

$$q = \frac{l}{r} \tag{2.55}$$

where q is arbitrarily large for a LHCP wave, zero for a RHCP wave and unity for linear polarization. The axial ratio and tilt of the polarization ellipse is given by

$$AR = \left|\frac{1+|q|}{1-|q|}\right|$$

and

$$\tau = -\frac{1}{2}\arg(q)$$

respectively.

The unit vectors and polarization ratio for a wave defined to be propagating in the $+z$ direction will be the complex conjugate of those given by (2.53), (2.54) and (2.55) respectively.

Frequent references to circular polarization components defined by vectors

$$\hat{\mathbf{u}}_L = \hat{\mathbf{u}}_x - j\hat{\mathbf{u}}_y \tag{2.56}$$

$$\hat{\mathbf{u}}_R = \hat{\mathbf{u}}_x + j\hat{\mathbf{u}}_y \tag{2.57}$$

are made where $|l|^2 + |r|^2 = \frac{1}{2}$ and this will be adopted in the discussion on antenna measurements in order to maintain consistency with the literature. The definition has no impact on the circular polarization ratio.

The polarization ratio of a wave, designated by subscript 1, is orthogonal to 2 if the condition

$$q_1 = \frac{1}{-q_2^*} \tag{2.58}$$

is met. Physically, the wave represented by q_2 has the opposite sense of rotation, the same axial ratio but major axis of the ellipse in quadrature to that of q_1.

2.2.4 Instrument model

The polarimeter consists of a number of interferometers made by forming pairs of receiving elements from a larger array. In order to maximise the number of interferometers (and therefore spacings) from a given array, elements are usually common to many different interferometers. Moreover in most telescopes, these elements are mobile, allowing the formation of even more spacings over a period of time. The interferometer forms the basic unit of the synthesis telescope and plays a definitive role in the polarimetric response of the instrument. The interferometer model depicted schematically in figure (2.7) represents a class of instrument possessing the following characteristics.

1. The antenna is a prime focus reflector and feed arrangement where the feed is an aperture of a low loss waveguide system.

2. The antennas are capable of tracking the phase centre as the Earth rotates, that is to say the reference phase centre remains fixed at a constant polar angle, θ, in the antenna pattern. The normal observing situation will be to keep the reference phase centre on boresight, $\theta = 0$. Moreover, there is no rotation of the antenna co-ordinate system with respect to the map system. Fixing the antenna pattern to the map co-ordinate system in this manner is accomplished with equatorial mounting systems.

3. Motion of the antenna in the direction of the source resulting in changes in geometrical delay, τ_g, has been compensated for by adjustment of an electrical delay.

4. The antenna system responds to radiation of two orthogonal polarizations simultaneously both of which are used for the imaging process.

5. A common local oscillator is used in the frequency conversion of both polarization channels.

Other considerations not explicitly built into the model are assumed in order to simplify the following discussion. As the earth rotates the track co-ordinate system relative to the sky, motion of the u-v plane in the direction of w is possible, resulting in changes to the geometrical delay, τ_g in figure (2.7). Variation in this delay manifests itself as a rotation of the visibility phase. Insertion of a compensating instrumental delay, τ_j , to offset this effect is assumed to be in effect and a complex correlator capable of providing both real and imaginary parts of the visibility in the absence of this rotation is then required.

The quasi-monochromatic assumption remains in effect for the model analysis. Bandwidth beyond that allowing for satisfactory operation as an imaging telescope is accommodated in this instrument by dividing the input spectrum into four separate sub-band channels (hereafter called bands) after the front end (i.e. antenna system, polarization networks and RF electronics) and processing them independently. Changes in the centre frequency of the instrument are small with respect

to the operating bandwidth of the model elements. The model elements are then either assumed to be bandwidth independent or their frequency response accounted for by averaging over this band. Channel gain, g_C, is a complex factor that relates intensity of the incident radiation to units of the recorded correlator output and includes the net contribution from many system components, examples being, the front end and intermediate frequency amplifiers.

A high degree of isolation exists between most model elements so that they do not contribute significantly to inter-channel coupling (also referred to as crosstalk). The most consequential, from the standpoint of polarimetry, is that between channels of opposite polarization. Such coupling is most likely to occur at the correlator where two channels are present as inputs and at the antenna system where the radiation is separated into the two orthogonal polarizations. Inter-band coupling between channels of like polarization is not considered a problem in this study and inter-band coupling between opposite polarizations will be no more severe than the previous two cases. Crosstalk at the correlator is expected to be much smaller than that of the antenna system so that the latter will be the subject of cross talk models presented in the following discussion. All coupling between channels is accounted for in the model by a front end directional coupler which, in reality, is formed by elements of the antenna and RF transmission system. The model will consider an interferometer formed from two channels of opposite polarization but same band because coupling in this situation is expected to have a direct impact on the response to polarization. In general the channels may be associated either with two distinct antennas or by both polarizations received by a single antenna.

The model includes a frequency conversion stage and serves to demonstrate the effect of a frequency conversion at least from the standpoint of polarimetry. Single sideband reception is considered as this is employed within the DRAO ST.

Polarization will be described by orthogonal circular components. The coordinate system for describing the physical properties of polarization (i.e. tilt and rotation sense) described earlier (section 2.2.1 and figure (2.2b)) will be maintained. This is a rectangular system with the z-axis parallel but with opposite direction to the direction of propagation, the x-axis directed northward on the sky and its origin at the instrument. The coherency matrix will refer to this system. With exception of the feed rotation phase, ϕ, the model does not presuppose any particular choice of polarization representation, but a selection is made at this point to simplify notation. This choice is obvious since the inherent response of the existing instrument is nearly circular. Unless specified otherwise, upper case L and R subscripts will label quantities that are associated with the *left* and *right* channels respectively. The designation of *left* and *right* in this case refer to the principal polarization of that particular channel (i.e. the component of polarization that contributes most significantly to the response of the channel). Lower case l and r designate *left* and *right* components of an arbitrarily polarized wave, hence, l_R would be the LHC component present in the channel with RHC principal polarization. Two channels, one responding to LHCP power from antenna i, and the other RHCP from antenna j are correlated by the complex correlator to form the product, LR_{ij}, and will exemplify the response of the interferometer. All correlation products RR, LL, LR and RL

are measured simultaneously for each of four bands within the existing instrument.

It is useful to reference a co-ordinate system when discussing the response of the model. A suitable reference system is formed by considering the antenna co-ordinates when the Y-axis is aligned with the u-axis of the visibility co-ordinate system as depicted in figure (2.5). This situation occurs when the reference phase centre is located at 0 HA and over the celestial pole as seen from equation (2.48). The contribution to the interferometer response will now be considered in more detail.

2.2.5 Antenna system

The antennas employed in the array are prime focus parabolic reflectors, 8.5 metres in diameter, and 0.4 f/d. The reflectors are illuminated by a circularly symmetric, multimode feed antenna that serves to match the aperture of a circular waveguide to the focal plane fields of the reflector. A drawing of this feed appears in figure (4.1). The circular waveguide is 0.7λ in diameter and the outer cavity of the matching section is 2.6λ (65 cm).

The antenna will be modelled as a product of boresight gain, g_a and normalised voltage radiation pattern. However, since the model is confined to predicting polarization characteristics at the field centre (near boresight of the antenna), only the boresight gain is considered as the high degree of circular symmetry in the reflector and feed system imply a low contribution to the overall cross-polarization coupling, at least relative to the system elements that follow.

The antenna position angle (about the boresight axis) is depicted in figure(2.7) by a length of transmission line of electrical length, ϕ, which adds a phase constant to each but opposite in sign between channels. Rotation is represented in this manner in as far as the quasi-monochromatic assumption holds. Strictly speaking, the phase due to rotation is not likely to be frequency dependent, as it is for a length of transmission line. This quantity is constant, since there is no rotation of the antenna relative to the sky, and has no direct consequence for calibration and subsequent data correction. However, it is included to account for the feed position in anticipation of later comparison of the interferometer response to laboratory measurements of the feed antenna.

Considering incident radiation represented by the field components, E_L and E_R , the input to the waveguide is then given by

$$E_{SL} = g_a E_L e^{-j\phi} \tag{2.59}$$

$$E_{SR} = g_a E_R e^{j\phi} \tag{2.60}$$

where ϕ represents the feed position angle and is related to the ellipse tilt of the incoming radiation, τ, in figure (2.2b) by $\phi = \tau$. The phase of the LHCP component advances as ϕ decreases (north to east) and the RHCP is correspondingly retarded.

2.2.6 Waveguide components and the direction coupler model

Although circular polarization is considered in the model to be the principal polarization, in reality the antenna system is not so constrained. That is to say that any two orthogonal polarizations could be received by the hardware. Ultimately, electric field components representing the two principal polarizations must be transferred and independently applied to the system electronics which in themselves are not sensitive to vector quantities but rather to complex voltages. The waveguide system now considered performs the transformation from polarization vector to channel voltages and in doing so defines the principal polarizations of the ST.

Power from the antenna feed aperture is coupled into a circular waveguide of diameter $0.7\lambda_{1420}$ by exciting the dominant TE11 mode (see Chatterjee (1986) and other references, notably Marcuvitz (1986)). A circularly polarized wave propagates down the waveguide as two orthogonal linear components in phase quadrature. A quarter-wave plate consisting of three reactive posts perpendicular to the wall of the wavguide serve to delay the propagation of electric field components that are parallel to the posts and in so doing convert a circularly polarized wave to a single linear component. A circularly polarized wave of opposite sense to the first will be likewise converted by this structure but to a linear component orthogonal (i.e. perpendicular) to the former. Thus, the quarter-wave plate performs the conversion of circular to linear polarization where the linear components now correspond to respective circular components at the waveguide input aperture. These linear field components are coupled out of the waveguide by two probes perpendicular to each other which feed low noise amplifiers of the ST receiving system. A drawing of the feed is presented in figure (4.1) on page 88. A detailed discussion of the quarter wave plate in general may be found in many elementary texts on microwave theory such as that by Gardiol (1984). The geometry and number of posts are necessary to increase the operating range of the device by maintaining the desired phase delay at 90° over a range of frequencies. Details of this design (on which the present implementation is based) can be found in a paper by Simmons (1952).

The quarter-wave plate and circular waveguide as just described are idealisations and are only approximated in reality by elliptical waveguides, probes which are coupled together by electric fields or not exactly perpendicular (especially for probes of finite thickness) and phase delays that are only approximately 90°. All the aforementioned deviations from the ideal concept result in a less than complete separation of circular into orthogonal linear components. Hence the output probe corresponding to one of the principal polarizations will also contain a fraction (frequently thought of as a leakage term) of the opposite one. This has consequences for polarimetry and hence much attention will be paid to the performance of these elements. For the purposes of understanding instrument response and developing calibration procedures it is unnecessary to undertake a detailed study of the waveguide elements and their associated imperfections, but rather replace them with a representative circuit model relating the response or terminal voltages (v_{SL} and v_{SR} in figure (2.7)) to the principal polarization. The bounded nature of this structure makes it amenable to such analysis because energy conservation constraints can

readily be applied and indeed such tools exist for the analysis of microwave circuits of this type.

The waveguide, quarter-wave plate and probe structures can be modelled by a four port microwave network expressed in the usual scattering matrix notation (Gardiol (1984)). Thus

$$\begin{bmatrix} b_1 \\ b_2 \\ b_3 \\ b_4 \end{bmatrix} = \bar{S}\,[s_i] \begin{bmatrix} a_1 \\ a_2 \\ a_3 \\ a_4 \end{bmatrix} \tag{2.61}$$

where waves propagating toward the network port i are represented by the normalised quantity a_i and away from the network by b_i such that the power incident on port i, P_i, is given by

$$P_i = |a_i|^2 - |b_i|^2 \tag{2.62}$$

The scattering matrix S relates the electric fields of waves entering the waveguide system to voltages of waves leaving through coaxial transmission lines via the linear probes. The output ports are affiliated with obvious physical structures whereas the input ports are not. However Chatterjee (1986) demonstrates, in his discussion on power orthogonality, that a lossless, hollow cylindrical waveguide can carry power independently in each possible mode. Two TE11 modes in space quadrature are excited by the two orthogonal fields present at the aperture of the waveguide and are thought of as the two input ports of the system. The following properties are assumed about the network.

The network is reciprocal, so that

$$S_{ij} = S_{ji} \qquad i \neq j \tag{2.63}$$

, and is lossless, so that

$$\sum_{i=1}^{n} S_{ij}^{*} S_{ik} = \delta_{jk} \qquad \delta_{jk} = 1 \text{ for } j = k, \quad \delta_{jk} = 0 \text{ for } j \neq k \tag{2.64}$$

and matched at all four ports such that

$$S_{ii} = 0 \tag{2.65}$$

It is shown by Gardiol (1984) (and many others) that the above network must be either a trivial case of two uncoupled two port networks or a directional coupler. For the port labelling of figure (2.7) the scattering matrix of this device is

$$S = \begin{bmatrix} 0 & \alpha e^{j\delta_{LL}} & 0 & \beta e^{j\delta_{LR}} \\ \alpha e^{j\delta_{LL}} & 0 & \beta e^{\delta_{RL}} & 0 \\ 0 & \beta e^{\delta_{RL}} & 0 & \alpha e^{j\delta_{RR}} \\ \beta e^{j\delta_{LR}} & 0 & \alpha e^{j\delta_{RR}} & 0 \end{bmatrix} \tag{2.66}$$

where

$$\alpha^2 + \beta^2 = 1 \qquad \text{and} \qquad (\delta_{LL} + \delta_{RR}) - (\delta_{LR} + \delta_{RL}) = \pi \pm 2n\pi \tag{2.67}$$

It will now be demonstrated that for a network with the above properties, the two output ports (2 and 4 in figure(2.7)) will respond to respective orthogonal waves at the input of the waveguide. Consider an input wave described by

$$\mathbf{E} = a_1\hat{\omega}_L + a_3\hat{\omega}_R$$

where $\hat{\omega}_L$ and $\hat{\omega}_R$ are unit polarization vectors that may, for the sake of an example, represent left and right circular components. Setting the normalised input waves, a_1 and a_3 to unity associates ports 1 and 3 of the network with the two unit vectors $\hat{\omega}_L$ and $\hat{\omega}_R$. The output quantities of the network may be expressed in terms of this polarization vector set by substituting the scattering matrix of equation (2.66) into equation (2.61). Thus

$$\overline{\mathrm{b}} = \overline{S}\overline{a} = \begin{bmatrix} 0 \\ \alpha e^{j\delta_{LL}}\hat{\omega}_L + \beta e^{j\delta_{RL}}\hat{\omega}_R \\ 0 \\ \beta e^{j\delta_{LR}}\hat{\omega}_L + \alpha e^{j\delta_{RR}}\hat{\omega}_R \end{bmatrix} \tag{2.68}$$

where, by invoking reciprocity, the vectors $\mathbf{b}_2$ and $\mathbf{b}_4$ are the polarization vectors of waves (expressed in terms of the unit polarization vectors $\hat{\omega}_L$ and $\hat{\omega}_R$) that would be generated by exciting ports 2 and 4 respectively. Applying a check for orthogonality yields

$$\mathbf{b}_2 \bullet \mathbf{b}_4 = \alpha\beta e^{j(\delta_{LL} - \delta_{LR})} + \alpha\beta e^{-j(\delta_{RR} - \delta_{RL})} \tag{2.69}$$

Rewriting the phase constraint of equation (2.67) as

$$(\delta_{LL} - \delta_{LR}) + (\delta_{RR} - \delta_{RL}) = \pi$$

and substitution into equation (2.69) yields

$$\mathbf{b}_2 \bullet \mathbf{b}_4 = \alpha\beta e^{j(\delta_{LL} - \delta_{LR})} + \alpha\beta e^{-j(\pi - \delta_{LL} + \delta_{LR})} = 0 \tag{2.70}$$

hence the vectors are orthogonal. This result implies, that as long as the lossless, matched, reciprocal conditions are met, the two output ports of the directional coupler will respond to orthogonal components of an arbitrarily polarized input wave.

Physically, the probes are linear structures and the coupling parameters can in principle be chosen to convert the linear probe polarizations to any other orthogonal pair of vectors, in this case, circular. However the coupler model may also be exploited to model the non-ideal response, that is, deviations from the ideal design response of the system without consideration of the internal structure of the waveguide components. In this abstraction the input polarization is assumed pure circular and the output ports respond to pure circular so that, in an ideal instrument, the waveguide would be a simple transmission system with $\alpha = 1$ and $\beta = 0$.

In the existing, non-ideal instrument the coupler would then represent the leakage from one of the principal polarization channels into the other. The motivation for this approach is to express the polarization throughout the system by a single set of orthogonal vectors (in this case circular) which are close to the actual receiver response and then approximate the principal channel coupling by unity, i.e. $\alpha = 1$. This approximation greatly simplifies the formulation of the system response and the development of calibration procedures.

The voltage output of the LHCP channel by the coupler model, v_{IL}, is

$$v_{IL} = (E_{SL}\alpha_L e^{j\delta_{LL}} + E_{SR}\beta_{RL}e^{j\delta_{RL}})h_l g_{cl} \tag{2.71}$$

where, h_l and g_{cl} , represent the effective probe height relating units of electric field (Volt metre^{-1}) to units of potential (Volt) and the collective voltage gain of the system electronics that follow respectively. The voltage gains above and the phase of the coupler arm corresponding to the principal polarization can be combined into an aggregate channel gain, g_{Lo} as given by

$$g_{Lo} = g_a e^{j\delta_{LL}} h_l g_{cl} \tag{2.72}$$

which when applied to equation (2.71) after substitution of (2.59) and (2.60) give the following expression for the output of the LHC channel,

$$v_{IL} = \left(\alpha_L E_L e^{-j\phi} + \beta_{RL}e^{j(\delta_{RL}-\delta_{LL})}E_R e^{j\phi}\right) g_{Lo} \tag{2.73}$$

Following a series of steps similar to the derivation of equation (2.73) results in an equivalent expression for the RHCP channel. Thus,

$$v_{IR} = \left(\alpha_R E_R e^{j\phi} + \beta_{LR}e^{j(\delta_{LR}-\delta_{RR})}E_L e^{-j\phi}\right) g_{Ro} \tag{2.74}$$

Assuming the principal polarizations as a reference, the coupler coefficients can be expressed as normalised components of a general circularly polarized wave described in section 2.2.3. Since, the main arm coupler phase has been absorbed by the channel gain (as in equation (2.72)), the principal polarization component simply becomes the coupler coefficient, α, and, by definition of principal polarization, is very near unity. The LHCP component in the principally LHCP channel and the RHCP component present in the RHCP channel become respectively

$$l_L = \alpha_L \qquad r_R = \alpha_R \tag{2.75}$$

where α_L and α_R are real.

Following consistent notation to the above the LHCP and RHCP components become

$$l_R^* = \beta_{LR}e^{j(\delta_{RR}-\delta_{LR})} \tag{2.76}$$

and

$$r_L^* = \beta_{RL}e^{j(\delta_{LL}-\delta_{RL})} \tag{2.77}$$

respectively. The normalised polarization components are consistent with the reception of waves that are propagating in the -z direction and are defined in equation (2.53) and (2.54) of section 2.2.3. The conjugate operation applied to these components is a consequence of this co-ordinate system choice. The scattering matrix, to which δ_{LR} and δ_{RL} apply, is defined for waves propagating in the $+z$ direction. In terms of these normalised polarization components, equations (2.73) and (2.74) become

$$v_{L=} \left(E_L e^{-j\phi} l_L + E_R e^{j\phi} r_L \right) g_{Lo} \tag{2.78}$$

$$v_R = \left(E_R e^{j\phi} r_R + E_L e^{-j\phi} l_R \right) g_{Ro} \tag{2.79}$$

The feed position angle is constant in this type of instrument and therefore it may be included in the channel gain. This step will simplify expressions to follow. Letting g_L^* and g_R^* be the channel gains (the conjugate operation is a notational simplification anticipated for later use), which include the feed position phase, equations (2.78) and (2.79) become

$$v_L = \left(E_L l_L + E_R e^{j2\phi} r_L \right) g_L^* \tag{2.80}$$

$$v_R = \left(E_R r_R + E_L e^{-j2\phi} l_R \right) g_R^* \tag{2.81}$$

In an ideal system, the cross hand coupling terms, r_L and l_R , are zero and the voltage present at the outputs of the waveguide-amplifier system is simply the product of their respective channel gains and input field components. Applying the constraints of equations (2.67) to the normalised polarization components of (2.76) and (2.77) yields

$$l_R = -r_L^* \tag{2.82}$$

representing the reciprocal, lossless and matched four port model.

The condition of reciprocity holds without question for passive components that do not contain gyrotropic materials. The waveguide components considered here contain metallic conductors with exception of the dielectrics associated with transmission lines connecting the probes to the amplifiers and are therefore expected to satisfy the reciprocity condition. The networks were designed to exhibit low loss since this condition is a prerequisite for the reduction of thermal noise, hence, the low loss condition is reasonable. There is however nothing inherent in the physical makeup of the device to predispose the condition of good matching. Good design practice dictates that networks possess matched ports but practical limitations in construction and adjustment usually preclude a reflectionless network. Typical networks are considered matched if the return power from any excited port is 20 dB (10 % of the incident voltage) below that of the incident wave. A good match is considered to be near the noise floor of quality commercial lab equipment, without invoking extraordinary efforts in the measurement procedure. Such a condition exhibits about 40 dB return loss. A finite return loss at the ports can destroy the

symmetry of the scattering matrix with the result being that the cross coupling coefficients are no longer equal and the phase constraints for the ideal coupler no longer hold. This manifests itself as an asymmetry in the cross correlation products as discussed later. Even with the ideal coupler model assumption violated the form of the model is still representative, to a good approximation, of the polarization imposed on the instrument by the waveguide system. The expression of polarization in the form of normalised polarization components will be retained throughout this thesis although the underlying coupler model will be implied.

2.2.7 Frequency conversion

The frequency conversion stage included in the model is representative of a number of such stages that may exist in a given instrument. Frequency conversion is achieved by a multiplication of the input signal by that of the local oscillator (which can be fixed or tunable) to produce an output which has a spectrum similar to the input but shifted in frequency to the sum and the difference of the two input frequencies. Expressing the signals in the analytic form of equation (2.6) and using the left hand channel as an example,

$$v_L = v_{LI} \cdot v_{LO} = |v_I|\, e^{\pm j(\omega_{IL} t + \phi_{IL})} e^{\pm j(\omega_{LO} t + \phi_{LO})} \tag{2.83}$$

where ϕ_{LO} and ϕ_{IL} are the phases of the local oscillator and input signal respectively and, ω , is the radian frequency in rad $\sec^{-1}$. The gain or loss of the frequency conversion is incorporated into the overall channel gain so that equation (2.83) represents the effect of this process on the frequency and phase of the applied signal. The frequency conversion is a non-linear process so the above relation is only valid with the assumption that

1. high order frequency products are removed from the output by filters leaving only signals at the sum and difference of the fundamental input frequency components and

2. that the device is operated with the amplitude level of the local oscillator well into the saturation range so that changes in its amplitude are not reflected in the output product.

These conditions are met in any practical frequency converter. Four possible products result depending on the sign combination selected for the exponential arguments of equation (2.83). The results are summarised in table (2.1).

The last entry for the lower sideband of the up conversion process is discarded in keeping with the original decision to represent the analytic signal by a positive sign (i.e. accept positive frequencies as representing reality). Down conversion refers to the situation where the output frequency is below that of the input and represents the two cases found in this instrument. The upper sideband conversion is employed in the front end of the telescope after the first stages of amplification and serves to bring the input frequencies down to an intermediate frequency where further amplification and signal delay is applied. Since the phase and spectrum of the input

conversion direction	sideband	frequency	phase
down	lower	$\omega_{LO} - \omega_I$	$\phi_{LO} - \phi_I$
down	upper	$\omega_I - \omega_{LO}$	$\phi_I - \phi_{LO}$
up	upper	$\omega_I + \omega_{LO}$	$\phi_I + \phi_{LO}$
up	lower	$-\omega_I - \omega_{LO}$	$-\phi_I - \phi_{LO}$

Table 2.1: Output products from the frequency conversion process.

are preserved, this stage is of little consequence to the operation of the instrument. A second conversion (the baseband conversion) divides the intermediate frequency band into the four subbands of the instrument, the lowest in frequency beginning at near zero and increasing. In this case the local oscillator is above the input frequency (the lower sideband selection of the down conversion process) and the spectrum of the output signal is inverted relative to that of the input (i.e. increasing input frequency results in a corresponding decrease in output frequency). Moreover, the phase is likewise negated and this phase inversion has a consequence on telescope response. This phase conversion may be accounted for in equations (2.80 and (2.81) by a conjugate of the channel phase. Letting , v_L and v_R , be the channel outputs after frequency conversion, these two equations become

$$v_L = \left(E_L^* l_L + E_R^* e^{-j2\phi} r_L^*\right) g_L \tag{2.84}$$

$$v_R = \left(E_R^* r_R + E_L^* e^{j2\phi} l_R^*\right) g_R \tag{2.85}$$

where the channel gains, g_R and g_L , take into account the phase inversion of the frequency conversion stage. This phase inversion applies only to the phase of elements that are located between the antenna and frequency conversion even though the back-end system elements are also lumped together in this factor. A more rigorous approach would be to have carried an additional factor representing the gain elements after frequency conversion but, since it is of little consequence in this study, it has been ignored for notational convenience. The effects of frequency conversion must also be accounted for in the application of delay but these considerations are beyond the scope of this thesis.

2.2.8 Correlator output

Treating the correlator as essentially a multiplication process, equations (2.84) and (2.85) may be multiplied together to form one of the correlation products. Letting, i and j, represent two distinct elements of the array, the left-right correlation product, LR, may be formed as

$$LR_{ij} = v_{L_i} v_{R_j}^* = g_{L_i} g_{R_j}^* \left(E_L^* E_R + E_L^* E_L l_{R_j} e^{-j2\phi_j} + E_R^* E_R r_{L_i}^* e^{-j2\phi_i}\right) \tag{2.86}$$

The co-polarization components, l_L and r_R , represent the principal polarizations and are assumed to be unity in keeping with the coupler model of this section.

Moreover, products involving the cross polarization components, l_R and r_L, with the cross polarization field terms, $E_L^* E_R$, have been ignored as they are expected to be much smaller than the remaining ones. Strictly speaking, equation (2.86) is not valid for monochromatic radiation, but the condition asserted by the quasi-monochromatic radiation assumption is that, although the radiation is confined to an arbitrarily small spectrum width, its components are not coherent and therefore can only be described by the first and second moments of statistical radiation. The visibility as introduced in equation (2.21) encompasses these quantities and can therefore replace the field products of equation (2.86). Thus,

$$LR_{ij} = 2g_{L_i} g^*_{R_j} \left(\vartheta^*_{LR}(\mathbf{r}) + \vartheta^*_{LL}(\mathbf{r}) e^{-j2\phi_j} l_{R_j} + \vartheta^*_{RR}(\mathbf{r}) e^{-j2\phi_i} r^*_{L_i} \right) \tag{2.87}$$

The factor two in front of the gain product serves as a reminder that the visibility definition used by radio astronomers is twice the value of the respective coherency matrix elements as traditionally defined. Applying similar operations to the three other correlator products yields

$$RL_{ij} = 2g_{R_i} g^*_{L_j} \left(\vartheta^*_{RL}(\mathbf{r}) + \vartheta^*_{RR}(\mathbf{r}) e^{j2\phi_j} r_{L_j} + \vartheta^*_{LL}(\mathbf{r}) e^{j2\phi_i} l^*_{R_i} \right) \tag{2.88}$$

$$LL_{ij} = 2g_{L_i} g^*_{L_j} \left(\vartheta^*_{LL}(\mathbf{r}) + \vartheta^*_{LR}(\mathbf{r}) e^{j2\phi_j} r_{L_j} + \vartheta^*_{RL}(\mathbf{r}) e^{-j2\phi_i} r^*_{L_i} \right) \tag{2.89}$$

$$RR_{ij} = 2g_{R_i} g^*_{R_j} \left(\vartheta^*_{RR}(\mathbf{r}) + \vartheta^*_{RL}(\mathbf{r}) e^{-j2\phi_j} l_{R_j} + \vartheta^*_{LR}(\mathbf{r}) e^{j2\phi_i} l^*_{R_i} \right) \tag{2.90}$$

The spacing vector, $\mathbf{r}$, is related to the interferometer pairs designated by ij in accordance with earlier discussions on co-ordinate systems. Some details of the correlator design when taken with the frequency conversion have consequences for the instrument response that must be accounted for in the mapping process. The frequency conversion inverts the phase of the visibility and has two consequences;

1. the map is rotated by 180° and
2. the coherency matrix associated with the brightness (equation (2.21)) is conjugated.

The formulation for Stokes U will undergo a sign change as a result of the conjugated coherency matrix. Stokes U as calculated from equation (2.40) is employed within the DRAO software at the time of this writing even though the adoption of the polarization co-ordinates of figure (2.2b) suggests the use of (2.41). Although the map is rotated by the frequency conversion, the negation of the u-v visibility co-ordinates (see section 2.2.2) compensates for this when the kernel of the transform in (2.47) is employed.

2.2.9 Coupler orthogonality and instrumental polarization

A condition for orthogonality of two waves as specified in the last section is that their correlation product be zero for incident unpolarized radiation. If the ideal coupler condition of equation (2.82) is applied to (2.87) and (2.88) together with the conditions for unpolarized radiation, $\vartheta_{RR} = \vartheta_{LL}$, $\vartheta_{LR} = \vartheta^*_{RL}$, the following products are obtained,

$$LR = I g_{L_i} g^*_{R_j} \left(l_{R_j} - l_{R_i} \right)$$

$$RL = I g_{R_i} g^*_{L_j} \left(-l^*_{R_j} + l^*_{R_i} \right)$$

where, I , is the intensity. Eliminating terms between these two equations yields

$$\frac{RL}{I g_{R_i} g^*_{L_j}} = \frac{-LR^*}{I g_{L_i} g^*_{R_j}}$$

Hence, if the antenna systems are identical (i.e. $l_{R_i} = l_{Rj}$), in addition to providing orthogonal polarization outputs, or, in the case of a single antenna in which, $i = j$, the above correlation products are zero. This is to say that an inteferometer will provide orthogonal outputs if

1. conditions pertaining to an ideal coupler, i.e. lossless and matched input network, are met and

2. both antennas are identical.

The latter is an additional constraint imposed on interferometers over single antennas.

If the above two conditions are met, the total polarized intensity can be determined from either equation (2.22) or in terms of Stokes parameters by equation (2.36).

In reality, the ideal coupler constraints are not met and the antennas are not identical with the consequence that the cross-correlation products are non-zero for unpolarized radiation. This apparent polarization of an unpolarized source is referred to as *instrumental polarization*, in the case of the non-ideal coupler, and must be removed before reliable maps can be made with the instrument. Instrumental polarization will be formally defined in chapter 3 together with a method presented to remove it.

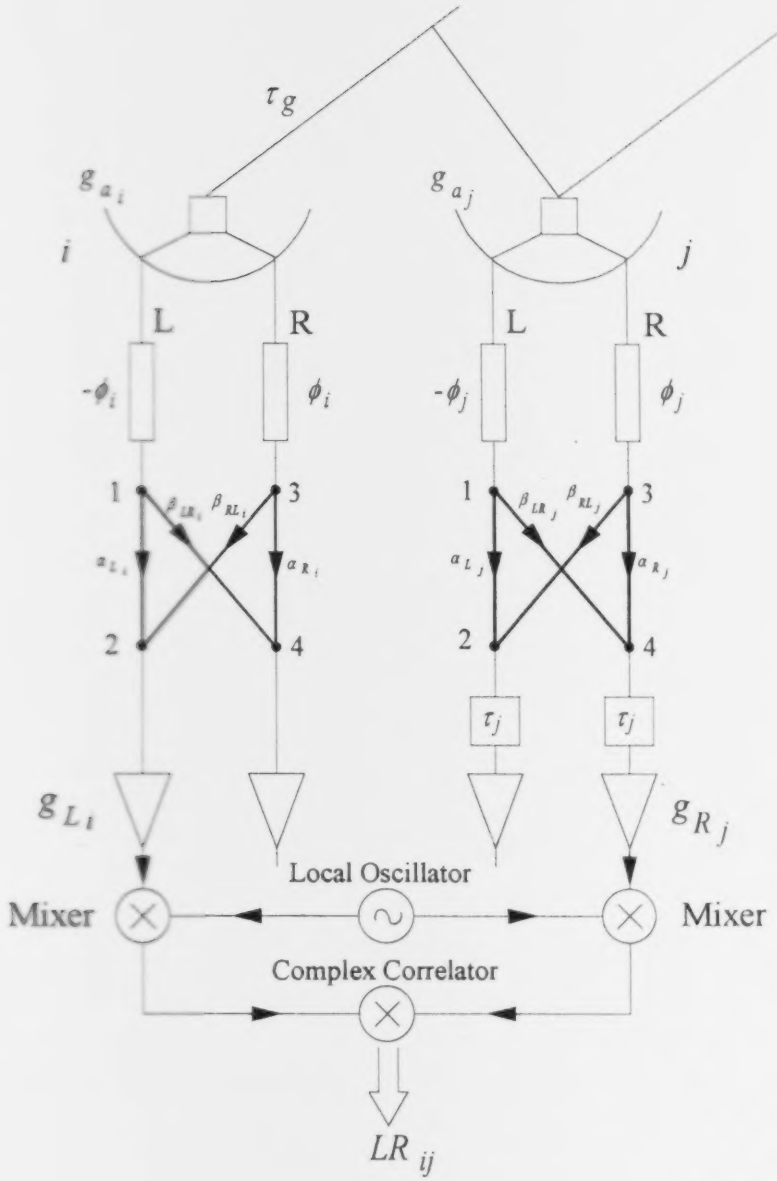

Figure 2.7: A block diagram of the synthesis telescope model.

Chapter 3

Telescope Calibration

The kind of science addressed by this telescope assumes partial linear polarization for sources and requires knowledge of the position angle to an accuracy of about 5° and the polarized fraction to within 1% or better of the total source intensity. This chapter demonstrates that the uncalibrated telescope cannot attain this goal but after instrument calibration and data correction processes developed in this thesis are applied, these demands can be met.

The problems encountered in calibrating the DRAO synthesis telescope are unique in that (a) the equatorial mounts do not permit the antenna radiation pattern to rotate with respect to the sky, (b) the entire array consists of circularly polarized antennas on equatorial mounts, and (c) the feed antennas are far from ideal and far from being identical. For these reasons, calibration techniques unique to this instrument had to be developed to meet the scientific objectives.

This chapter demonstrates that, when predominantly circularly polarized antennas are employed and the polarized part of the observed radiation is linearly polarized, it is not necessary to know the exact polarization characteristics of the antennas to perform successful polarimetry. However, the orthogonality of the antennas, while it need not be perfect, needs to be carefully calibrated. Moreover, it is noted that calibrating the array for orthogonality only, as opposed to referencing to an antenna of unknown polarization, makes optimum use of the available information and yields more reliable results.

The techniques developed in this chapter can find application in other telescopes, especially those with antennas whose polarization properties are far from ideal.

3.1 Calibration and Correction of Instrumental Effects

Creation of a map which is representative of the physical brightness and polarization of sources in the observed field depends on the instrument providing visibilities that

1. are proportional with a known constant of proportionality to the intensity of radiation intercepted by the antenna elements,

2. correspond to known spacings (i.e. antenna and track positions) and

3. are products of channels corresponding to respective polarizations that are both known and orthogonal to each other as described in chapter 2.

In general the complex gain factor relating intensity of incident radiation to the quantity that is actually recorded at the output of the correlator is unknown, the two polarization channels are not orthogonal to each other and uncertainties exist in the knowledge of antenna polarization and u-v co-ordinates. Moreover these quantities may vary in an unknown manner across the field of view.

The instrument response can be deduced approximately from knowledge of the instrument's design and a model established as was done in the latter part of chapter 2. In the case of the telescope at DRAO, for example, the polarizations are assumed to be orthogonal left and right circular and constant across the field of view. The formulation of the map making process and Stokes parameters are based on this idealised (and reasonably close to reality) model. Correction, in this context, is the modification of gain and polarization coefficients of the model so that the model more accurately reflects the true response of the instrument and thereby meets the criteria of the three points listed above. Calibration refers to the process whereby these model coefficients are established and involves the application of a known input (i.e. observation of a source with known properties), recording the response and then solving for the model coefficients.

Calibration and correction as dealt with in this chapter will apply to point sources at the centre of the field. This follows the premise that the prevalent instrumental characteristics will be constant over the field of view with smaller order effects increasing in magnitude with distance from the map centre. Moreover these procedures are applied on a routine basis as an integral part of normal telescope operation. The antenna gain pattern contribution to the channel gain is an obvious example of field dependent instrumental characteristics and is commonly applied, with certain limitations, in radiotelescope observations at a later stage of image processing. Calibration for antenna patterns is dealt with by a special process outside the normal operational mode of the telescope. Correction for field dependent polarization properties has not yet been attempted and must await further investigations.

The instrument response is frequency dependent and this dependence is taken into account by applying the procedures of this chapter to all four continuum frequency bands of the instrument.

3.1.1 The need for interferometer response correction

Expressions developed in chapter 2 yield the response of an interferometer to input visibilities. This response is expressed as a function of several parameters such as the channel gains, cross-channel coupling coefficients and co-channel coupling coefficients that pertain to the directional coupler model also presented in that chapter. Ideally the ST products should represent the observed visibilities expressed in orthogonal circular components and would do so in the special case where the channel gains are unity, each of the antennas of the interferometer responded to both RHCP and LHCP radiation and the feed position angle of both antennas was identical. This situation is not true in general and this idealisation can be violated

in a number of ways. Each affects the response with varying degrees of severity. Moreover it will become apparent that the correction and calibration process is most effectively implemented in practice by attacking each of these violations individually, and to some extent, independently. These violations to the ideal situation are:

1. The channel gains are not unity but are the product of factors representing amplification, losses and scale factors to provide an instrument output that expresses visibilities in desired units of flux.

2. The channel gains associated with both polarizations of a given antenna are not identical.

3. The channel gains of all antennas are not identical.

4. Both polarizations of each antenna are not circular.

5. The polarizations of the two outputs of an individual antenna are not orthogonal to each other.

6. Both antennas of an interferometer do not have identical polarization characteristics.

These expressions will now be examined to demonstrate how failure in meeting this ideal will affect the response of the instrument.

The output products provided by an interferometer of the synthesis telescope at DRAO are expressed by

$$LL_{ij} = I_T l_{L_i} l_{L_j} \left(2\rho^*_{LL} + 2\rho^*_{RR} \frac{r^*_{L_i}}{l_{L_i}} \frac{r_{L_j}}{l_{L_j}} + 2\rho^*_{LR} \frac{r_{L_j}}{l_{L_j}} + 2\rho^*_{RL} \frac{r^*_{L_i}}{l_{L_i}} \right) \tag{3.1}$$

$$RR_{ij} = I_T r_{R_i} r_{R_j} \left(2\rho^*_{LL} \frac{l^*_{R_i}}{r_{R_i}} \frac{l_{R_j}}{r_{R_j}} + 2\rho^*_{RR} + 2\rho^*_{LR} \frac{l^*_{R_i}}{r_{R_i}} + 2\rho^*_{RL} \frac{l_{R_j}}{r_{R_j}} \right) \tag{3.2}$$

$$LR_{ij} = I_T l_{L_i} r_{R_j} \left(2\rho^*_{LL} \frac{l_{R_j}}{r_{R_j}} + 2\rho^*_{RR} \frac{r^*_{L_i}}{l_{L_i}} + 2\rho^*_{LR} + 2\rho^*_{RL} \frac{r^*_{L_i}}{l_{L_i}} \frac{l_{R_j}}{r_{R_j}} \right) \tag{3.3}$$

$$RL_{ij} = I_T r_{R_i} l_{L_j} \left(2\rho^*_{LL} \frac{l^*_{R_i}}{r_{R_i}} + 2\rho^*_{RR} \frac{r_{L_j}}{l_{L_j}} + 2\rho^*_{LR} \frac{l^*_{R_i}}{r_{R_i}} \frac{r_{L_j}}{l_{L_j}} + 2\rho^*_{RL} \right) \tag{3.4}$$

which are essentially equations (2.87) to (2.90) except that

1. the second order terms (that is terms involving products of cross-channel coupling coefficients) and the co-channel coupling coefficients have been retained,

2. the phase factor corresponding to the feed position angle is included within the channel gains and cross-coupling coefficients,

3. the visibility has been replaced with corresponding coherency matrix elements since only sources at the phase centre are considered and

4. the co-channel coupling coefficients are now considered the only contributors to the channel gain (the electronic systems, the feed position angle and antenna are not considered).

The above expressions apply in general to antennas of any polarization, contain no approximations and represent the polarimeter performance for a source at field centre. The above expressions exclude gain factors that are not affected by the coupling of power between channels of opposite polarization. The co-polar coupling coefficients that differ from unity as a result of a loss of power from one channel into the channel of opposite polarization appear in the channel gain as an attenuation in that particular channel. These are retained as the only contributors to channel gain since they are a function of coupling between channels. It is assumed, at least for this section, that the channel gain factors due to mechanisms other than this basic coupling such as amplifiers, antennas and frequency converters are somehow known and are therefore set to unity in the following discussion.

3.1.2 Uncertainty due to unknown RHCP-LHCP phase difference

The channel gain is a complex quantity, but for the purpose of forming an image, its phase is unimportant providing all antennas of the array exhibit the same. Both LHCP and RHCP channel phases are independent so far as total intensity imaging is concerned since the total intensity is the sum of both LL and RR products each of which involve the gains associated with one polarization. However, the linearly polarized radiation that appears in the Stokes Q and U maps is formed from the LR and RL cross-products so that the phase difference between left and right channels of the array must be known. Uncertainty in this phase difference will manifest itself as an uncertainty in the value of the position angle associated with the linear part of the observed flux. This can be demonstrated by substituting the RL coherency element for visibility in equation (2.90), substituting the result in equation (2.43) and considering only the predominant RL term. Solving for the position angle, τ yields

$$\tau = \frac{1}{2}\left(\arg(RL) - \arg(g_R) + \arg(g_L)\right) \tag{3.5}$$

where g_R and g_L are the right and left channel gains for the array.

The error in position angle will be $\frac{1}{2}$ of the phase difference that exists between RHCP and LHCP channels of the array. One of the contributing factors to channel phase is that of the antenna feed system itself. If antenna polarization is expressed in circular components, these components will be a product of circular components as would be measured in a reference co-ordinate system and a phase factor that varies correspondingly to a rotation of the antenna within the system. The phase of the LHC component will have an opposite sign to the corresponding phase change experienced by the RHC component. Equations (2.87) to (2.90) include this phase as a factor ahead of the cross-coupling coefficients as well as part of the complex channel gain. This feed position phase, ϕ, contribution can be separated from the channel gains as

$$LR = e^{-j(\phi_i+\phi_j)}LR' \tag{3.6}$$

$$RL = e^{j(\phi_i+\phi_j)}RL' \tag{3.7}$$

where the primed quantities are the unrotated products and the unprimed are the products represented in the previous expressions. The feed antennas in the instrument at DRAO are fixed to the main antenna system, and as discussed earlier, the antenna co-ordinates are fixed to the sky co-ordinates due to the equatorial mounting system. Hence the position phase is constant with hour angle and can be conveniently included with the channel gains. Moreover, from this point on, the position phase will also be considered part of the cross-channel coupling coefficients unless otherwise noted. Another way to state this is that the feed position will be an integral part of the feed polarization. The underlying assumption is that the co-ordinate system in which the feed polarization is specified is known.

3.1.3 Errors due to uncertainty in antenna polarization

The total flux and the total polarized part of the flux can be determined if the antennas of the array are identical and provide outputs responding to orthogonal polarization vectors as discussed in chapter 2. Unity channel gain is assumed. However, even though an accurate measurement of total polarized flux can be made, the polarization properties of this radiation (i.e. fraction of linear, position angle and fraction of circular) depend on knowledge of the antenna polarization. Antennas of the adopted principal polarization, circular in this case, would result in a perfect measurement. The Stokes parameters determined from visibilities provided by an instrument with arbitrary but assumed circular polarizations are found by converting the visibilities of equations (3.1) to (3.4) into measured Stokes parameters, I, Q, U and V , and

1. expressing the coherency elements in terms of source (true) Stokes parameters, I_o Q_o, U_o and V_o ,
2. applying the antenna orthogonality condition of equation (2.82) and representing the coupling in general by the coupling of right to left channels,
3. and making the corresponding coupling coefficients of all antennas of the array identical, i. e. $i = j$.

Thus

$$I = I_o \tag{3.8}$$

$$Q = Q_o\left[1 - |r_L|^2\right] - \mathrm{Re}\left[I_o m_l e^{j2\tau}\,(r_L)^2\right] - 2I_o m_c\,\mathrm{Re}[r_L l_L] \tag{3.9}$$

$$U = U_o\left[1 - |r_L|^2\right] + \mathrm{Im}\left[I_o m_l e^{j2\tau}\,(r_L)^2\right] + 2I_o m_c\,\mathrm{Im}[r_L l_L] \tag{3.10}$$

$$V = V_o\left[1 - 2\,(r_L)^2\right] + 2\,\mathrm{Re}\left[I_o m_l e^{j2r}\,(r_L l_L)\right] \tag{3.11}$$

where I_T, m_L, and m_c are the total flux, the fraction of linear flux and the fraction of circular flux respectively. Recall that

$$r_L r_L^* = 1 - l_L^2 \tag{3.12}$$

The co-channel coupling coefficient, l_L, is near unity for small right to left channel coupling which is the case for practical instruments of this type. The observed Stokes parameters are equal to the source Stokes parameters when right to left channel coupling is zero as expected. Consider, for illustrative purposes, an instrument in which the right to left channel coupling, r_L is real and the position angle of any linearly polarized part of the incident radiation is zero. All of the power associated with this linear part of the radiation will appear in both the Q and V maps. The severity of this coupling is represented by the fraction of RHCP power that appears in the LHCP channel and is expressed in terms of circular polarization ratios as discussed in the next section. The measured polarized flux in percent of total flux for radiation that is 50% linearly polarized is plotted in figure (3.1) against the fraction (in percent) of RHCP power present in the left hand channel due to coupling. Stokes Q contains 50 percent of the power associated with the total intensity measurement, I, as expected when there is zero coupling from the right to left channel. The power in Stokes Q is converted to V as coupling increases. The true polarized intensity is given by (2.36) so that error in the linearly polarized flux measurement is given by

$$e_p = 1 - \frac{\sqrt{Q^2 + U^2}}{m_l I_o} \tag{3.13}$$

Conversion of circular polarization in Stokes V will likewise appear in Stokes Q so that the error in the linear flux measurement will depend on the amount of circular polarization present. This error is plotted in figure (3.2) for various levels of circular polarization present in the incoming radiation against the fraction of RHCP power present in the LHCP channel. Similar plots can also be generated for the measurement of circular polarization in the presence of linear.

3.1.4 Errors due to non-orthogonality and non-similarity

Good fidelity of the polarized image and accurate determination of the total polarized fraction require both orthogonality between polarizations of a given antenna and similarity of polarizations between two antennas of an interferometer. A small amount of non-orthogonality in the presumably LHCP and RHCP channels associated with a given antenna will impart significant polarization to an otherwise unpolarized source. This bogus polarized flux appears as an additive offset to the true value as opposed to a fractional error as in the last section and whereas small deviations from the assumed circular polarization result in an acceptable uncertainty in the linear fraction of polarized flux, non-orthogonality of the polarizations of such antennas will result in levels of instrument generated polarized emission that

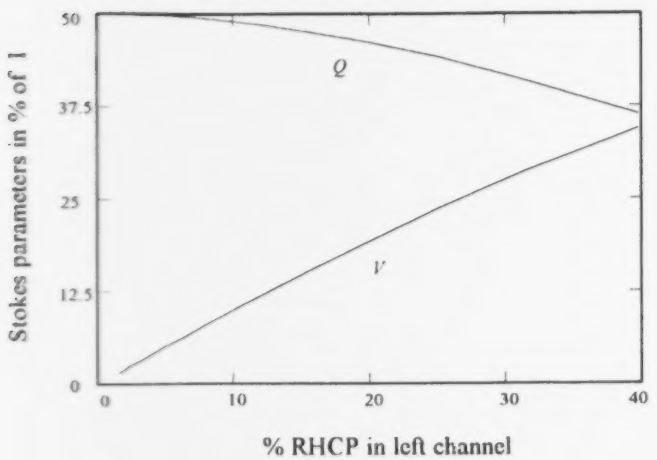

Figure 3.1: Stokes Q and V parameters as a function of RHCP contamination of the LHCP channel.

are similar in magnitude to the levels encountered from real sources. Instrument generated polarized flux that appears in the Stokes Q, U and V maps that is associated with flux in the total intensity (I map) is interpreted as a polarized fraction of this total emission, is indistinguishable from any true polarization of the source, and will be referred to as *instrumental polarization.*

The concept of instrumental polarization is valid for both single antenna telescopes as well as interferometers. However, in the case of an interferometer, correlation products are formed from pairs of different antennas and even though each individual antenna may provide orthogonal outputs the pair of channels involved in measuring the visibilities will not if the antennas are not identical in their polarizations. This is a problem unique to interferometry and affects the formation of a polarized image. Specifically, this problem manifests itself as polarized features appearing in the Q, U and V maps that are not necessarily associated with features in the total intensity map (I) of the source under consideration. This spurious emission can be distinguished from real source polarization by the manner in which it appears in the correlation products and is therefore distinct from instrumental polarization.

The effect on the interferometer products is demonstrated by equations (3.1) to (3.4) and considering the conditions of antenna orthogonality and similarity separately. The use of circular polarization ratios as described in the chapter on antenna measurements is better suited in general for describing the channel polarization than coupling coefficients and its use will be adopted here. The polarization of a given channel, i, can be completely described by the circular polarization ratio, q_i. Thus

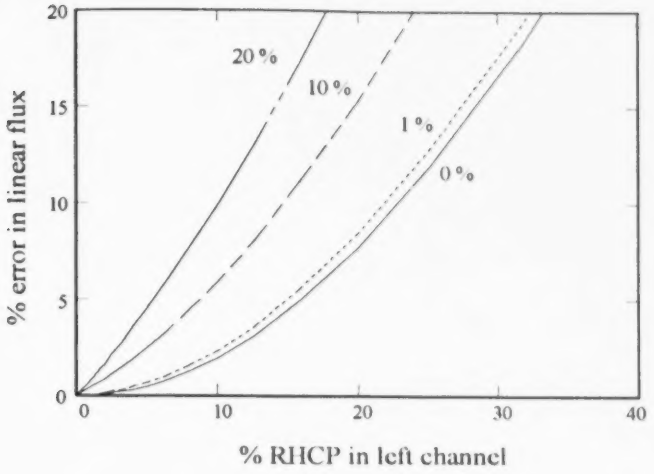

Figure 3.2: Error in linearly polarized flux measurement as a function of RHCP contamination of the LHCP channel. The four traces represent varying amounts of circularly polarized flux present.

$$q_{L_i} = \frac{l_{L_i}}{r_{L_i}} \text{ and } q_{R_i} = \frac{l_{R_i}}{r_{R_i}} \tag{3.14}$$

Recall (equation (2.58)) that the polarization orthogonality in terms of circular polarization ratio is expressed by

$$q_L = \frac{1}{-q_R^*}$$

where, in this case, polarization associated with the principal LHCP channel is orthogonal to that of the RHCP channel. The magnitude of the polarization ratio will be unity for linear polarization with the position angle determined from the phase, arbitrarily large for LHCP and zero for RHCP.

Substituting equations (3.14) into (3.1) to (3.4) yields

$$LL_{12} = 2I_T l_{L_1} l_{L_2} \left[\rho_{LL}^* + \frac{\rho_{RR}^*}{q_{L_1} q_{L_2}^*} + \frac{\rho_{LR}^*}{q_{L_2}^*} + \frac{\rho_{RL}^*}{q_{L_1}} \right] \tag{3.15}$$

$$RR_{12} = 2I_T r_{R_1} r_{R_2} \left[\frac{\rho_{LL}^*}{q_{L_1}^* q_{L_2}} + \rho_{RR}^* - \frac{\rho_{LR}^*}{q_{L_1}^*} - \frac{\rho_{RL}^*}{q_{L_2}} \right] \tag{3.16}$$

$$LR_{12} = 2I_T l_{L_1} r_{R_2} \left[-\frac{\rho_{LL}^*}{q_{L_2}} + \frac{\rho_{RR}^*}{q_{L_1}} + \rho_{LR}^* - \frac{\rho_{RL}^*}{q_{L_1} q_{L_2}} \right] \tag{3.17}$$

$$RL_{12} = 2I_T r_{R_1} l_{L_2} \left[-\frac{\rho_{LL}^*}{q_{L_1}^*} + \frac{\rho_{RR}^*}{q_{L_2}^*} - \frac{\rho_{LR}^*}{q_{L_1}^* q_{L_2}^*} + \rho_{RL}^* \right] \tag{3.18}$$

where the co-polar coupling coefficients are found from

$$l_L = \sqrt{1 - \frac{1}{1 + |q_L|^2}} \qquad \text{and} \qquad r_R = \sqrt{1 - \frac{|q_R|^2}{1 + |q_R|^2}} \tag{3.19}$$

The co-polar coupling coefficients are retained for sake of completeness as they form part of the overall channel gain but have no direct consequence for polarization measurements.

The response of an interferometer consisting of elliptically, but not identically, polarized antennas each providing orthogonal outputs are now considered. The condition of orthogonality is applied between corresponding LHCP and RHCP channels and, to set a worst case example for similarity, the polarization ellipses of one antenna are at right angles to the other. The interferometer polarizations for this situation are expressed in terms of polarization ratios as

$$q_{L_1} = q_0 \qquad q_{L_2} = -q_0 \qquad q_{R_1} = \frac{1}{-q_0^*} \qquad q_{R_2} = \frac{1}{q_0^*} \tag{3.20}$$

and depicted schematically in figure (3.3). Antenna dissimilarity in this case can be expressed by a single quantity, the RHCP contamination of the LHCP channel, which in percent is given by

$$\%RHCP \text{ in LHCP channel } = \frac{100}{q_L} \tag{3.21}$$

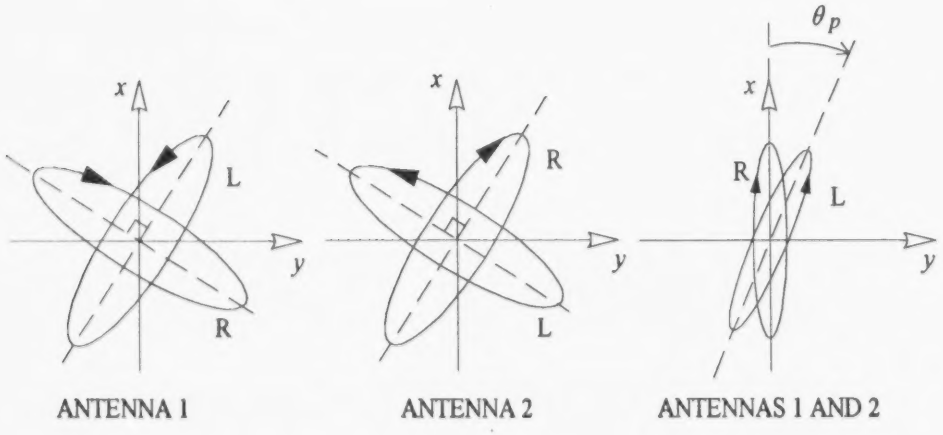

Figure 3.3: Polarization ellipses representing orthogonal but non-identical antennas in an interferometer are shown by the two left diagrams and of identical but non-orthogonal antennas by the right.

The following observations are drawn from the result that follows the substitution of equation (3.20) into (3.15) to (3.18). Discussion will be confined to results that affect the measurement of linear polarization.

1. The RR and LL products contain terms involving ρ_{LR} and ρ_{RL} that contribute an, in general complex, contribution to the total intensity in the presence of linearly polarized flux. This contribution appears as a phase and amplitude error in the total intensity measurement and is a function of the dissimilarity between antenna polarizations. Plots of the ratio of measured to true intensity and phase error versus the RHCP contamination of the LHCP channel are shown in figures (3.4) and (3.5) respectively. In an uncorrected instrument with highly elliptical antennas, this error could contribute to channel phase and amplitude errors that ultimately result in dynamic range limitation and the appearance of spurious features on the map. Moreover, an error in the measurement of channel gains could result following instrument calibration, again, with similar effects on the final map.

2. Terms in the LR and RL products containing ρ_{RL} and ρ_{LR} respectively are conjugates of each other and are therefore indistinguishable from true polarized flux. This contribution represents the ambiguity between circular and linear polarization associated with unknown antenna polarizations as shown in figures (3.1) and (3.2) and is small for near circularly polarized antennas. The most significant effect of dissimilar antennas is apparent in the terms of the LR and RL products involving ρ_{LL} and ρ_{RR}. This contribution to the cross-hand correlation products is due to the non-orthogonality between two different antennas of the interferometer and, as mentioned earlier, is distinct from non-orthogonality of the channels associated with any particular antenna. This contribution will be designated Xb and is given by equations that follow.

$$Xb_{LR} = 2I_T l_{L_1} r_{R_2} \left(\frac{\rho^*_{RR}}{q_{L_1}} - \frac{\rho^*_{LL}}{q_{L_2}} \right) \tag{3.22}$$

$$Xb_{RL} = 2I_T r_{R_1} l_{L_2} \left(\frac{\rho^*_{RR}}{q^*_{L_2}} - \frac{\rho^*_{LL}}{q^*_{L_1}} \right) \tag{3.23}$$

represent the contribution to the cross-hand correlation products due to differences in polarization between two antennas of the interferometer. By inspection

$$Xb_{LR} = -Xb^*_{RL} \tag{3.24}$$

Applying equation (3.24) to the expressions for Stokes parameters results in purely imaginary values for Q and U in contrast to the contributions of the true linearly polarized flux. Linearly polarized flux will contribute to the cross-polarization products as $LR = 2I_T l_{L_1} r_{R_2} \rho^*_{LR}$ and $RL = 2I_T r_{R_1} l_{L_2} \rho^*_{RL}$ with the expected conjugate relationship between them and will therefore contribute to the real parts of Q and U. If a point source is known to reside at the map phase centre, then the

polarization of the source may be determined from the real parts of the Q and U (ignoring the imaginary parts) parameters since their visibility phases are expected to be zero. This implies that, if the individual antennas of an interferometer pair are near circularly polarized (acceptably near being based on the errors in figure (3.1) and (3.2) of section 3.1.3) and provide orthogonal outputs, the polarization of a source may determined even if the antennas are not identical in their polarization characteristics. The spurious polarization as determined from the imaginary parts of Q and U can be significant although the example presented here represents a worst case orientation of the antenna polarization ellipses. A plot of $\mathrm{Im}(Q)$ as a percentage of the total flux is presented in figure (3.6).

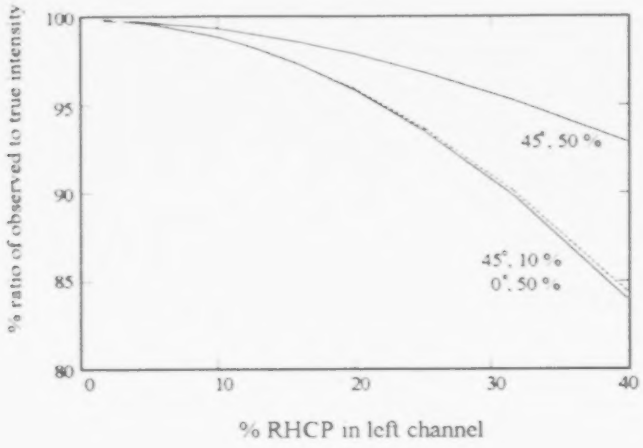

Figure 3.4: The ratio of total intensity observed with an inteferometer consisting of non-identical antennas, each providing orthogonal outputs, to the true value of total intensity. Labels on the curves represent the fraction of polarization and ellipse tilt of the received radiation.

Identical antennas that form an interferometer and provide non-orthogonal outputs are studied by considering polarization ratios given by

$$q_{L_2} = q_{L_1} \qquad q_{R_1} = q_{R_2} \qquad q_{R_1} = \frac{1}{-q_1^* e^{-j2\theta_p}} \tag{3.25}$$

where θ_p is the angle between the two polarization ellipses (90° for orthogonality) as shown in figure (3.3) which, when substituted in equations (3.15) to (3.18), provide the following observations.

1. The LL and RR products are subject to errors from the presence of linear polarization (i.e. non-zero ρ_{LR} and ρ_{RL}). This contribution is in the form of a real number added to the LL product and with opposite sign to the RR

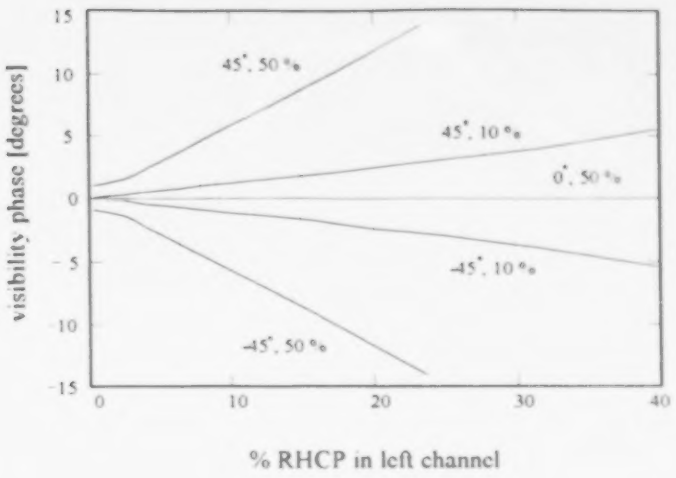

Figure 3.5: The visibility phase as observed by an interferometer consisting of non-identical antennas with orthogonal outputs. The true visibility phase is zero. Labels on the curves represent the fraction of polarization and ellipse tilt of the received radiation.

product (i.e. an instrumental circular component). Although the two contributions cancel upon forming the total intensity, their presence can complicate the calibration of channel gain under certain conditions (such as calibration on a polarized source with highly elliptical antennas).

2. The contributions of terms containing ρ_{LR} and ρ_{RL} to the RL and LR products respectively are small for antennas that are nearly circular. Errors in the determination of linearly polarized flux, due to this contribution, are similar in magnitude to those described in section 3.1.3 and figures (3.1) and (3.2).

3. The terms in the LR and RL products containing the coherency elements, ρ_{LL} and ρ_{RR}, are the most significant contribution resulting from antenna non-orthogonality. This contribution is referred to as instrumental polarization, is designated by IP, and is calculated from equations (3.26) and (3.27). The instrumental polarization contributions to the LR and RL quantities are conjugated with respect to each other and are therefore indistinguishable from true linearly polarized flux. The level of polarized flux which is observed as a consequence of instrumental polarization is dependent only on the total intensity and is added to any polarized flux present from the observed source.

The instrumental polarization is given by

$$IP_{LR} = \frac{1}{q_{L_1}} + q^*_{R_1} \tag{3.26}$$

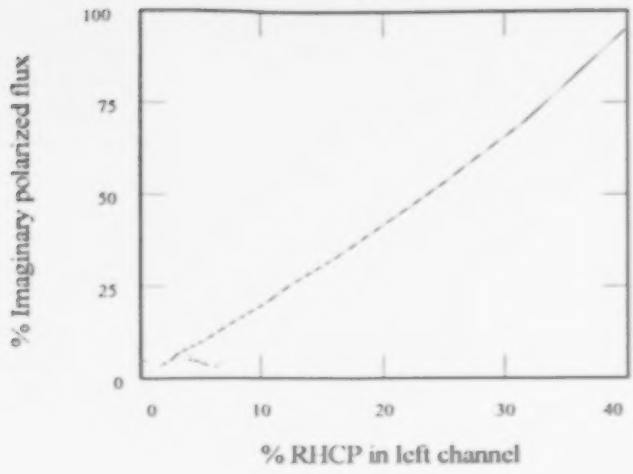

Figure 3.6: The imaginary part of Stokes Q observed for an interferometer consisting of non-identical antennas each providing orthogonal outputs. The polarization ellipses of the opposite hands have the same orientation for both antennas (see figure (3.3)) as a worst case example.

$$IP_{RL} = \frac{1}{q^{*}_{L_1}} + q_{R_1} \tag{3.27}$$

for the LR and RL products. The total instrumental polarization as calculated by

$$IP = \frac{\sqrt{\mathrm{Re}(Q)^2 + \mathrm{Re}(U)^2}}{|I_T|}$$

is plotted in figure (3.7) for various differences in antenna polarization ellipse orientations as specified by equation (3.25). It can be observed from this plot that even moderate amounts of right to left channel coupling (5 to 10 %) can create false measurements of polarization that compete in magnitude with the polarization from natural sources.

3.1.5 Array orthogonality

The similarity and orthogonality conditions considered thus far pertain to antennas forming a single interferometer, and in this case, occur independently of each other. Moreover, non-zero cross-hand correlations do not imply antenna orthogonality nor is the converse true. In an array such as that at DRAO (see 2.2.2 for a description) with n antennas, n sets of $(n-1)$ interferometers may be selected where one antenna of the set is in common with all others except itself (autocorrelation is not supported for cross-hand products). The conditions of similarity, which can be thought of as

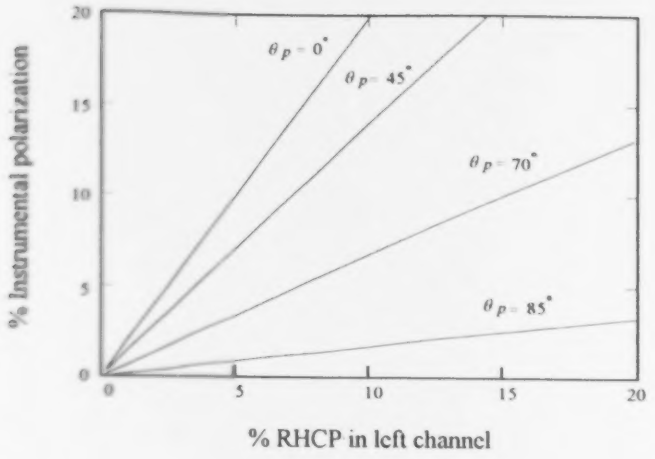

Figure 3.7: Instrumental polarization resulting from an interferometer consisting of two identical antennas each providing non-orthogonal outputs. The two antenna outputs correspond to elliptical polarizations having opposite senses of rotation. Four traces for the difference in orientation of the major axes of the polarization ellipses are shown. (See the right drawing of figure (3.3))

baseline orthogonality, and antenna orthogonality are no longer independent due to the fact that the interferometers of the array are not independent. The following demonstrates that for an array of three antennas, a zero cross-hand correlation product for each interferometer implies both orthogonality and similarity of the individual antenna outputs and of antennas respectively.

Consider correlation products formed from a three element array as follows. For $i = 1, 2$ and $j = 2, 3$ and $i \neq j$ correlator products $LR_{ij} \propto v_{L_i} v^*_{R_j}$ and $RL_{ij} \propto v_{R_i} v^*_{L_j}$ are formed where v_L and v_R are the left and right channel outputs respectively. Adopting the notation exemplified by $X \perp Y$ which is read as '*polarization X is orthogonal to polarization Y*', the following two statements are made without rigorous proof.

1. Given X there is a unique value for Y in which $X \perp Y$ where orthogonality as defined by equation (2.58) is true.

2. $X \perp Y, X \perp Z \Rightarrow Y = Z$ from (1).

Consider the situation where unpolarized flux results in zero cross-hand correlation products. The conditions of channel polarizations required are tabulated in table (3.1) for all three baselines of this three element array.

By inspection of table (3.1) it is seen that:

LR_{13} and LR_{23} and (2) $\Rightarrow q_{L_1} = q_{L_2}$ and LR_{12} and (1) $\Rightarrow q_{R_2} \perp q_{L_2}$

	1,2	1,3	2,3
$LR = 0$	$q_{L_1} \perp q_{R_2}$	$q_{L_1} \perp q_{R_3}$	$q_{L_2} \perp q_{R_3}$
$RL = 0$	$q_{R_1} \perp q_{L_2}$	$q_{R_1} \perp q_{L_3}$	$q_{R_2} \perp q_{L_3}$

Table 3.1: The first and second rows consist of the polarization conditions required to result in zero LR and RL products respectively. The column entries represent the three baselines of the three element array.

$q_{L_1} = q_{L_2}$ and RL_{12} and (1) $\Rightarrow q_{R_1} \perp q_{L_1}$
RL_{12} and RL_{13} and (2) $\Rightarrow q_{L_2} = q_{L_3}$ and LR_{23} and (1) $\Rightarrow q_{R_3} \perp q_{L_3}$

Hence, the polarizations provided by the individual antennas are orthogonal. Moreover, the above clearly shows that the polarization of the principal LHCP channels is identical for all three antennas and by statement (1), the principal polarization of the RHCP channels is likewise identical for all antennas. This principle is extended to larger arrays providing that triplets of antennas form interferometers in this way. Hence, in the array at DRAO, a zero value for both LR and RL for all interferometers of the array can only occur if the antennas are identically polarized with each providing orthogonal outputs.

3.1.6 Summary

The most significant points of the above discussion are summarised as follows.

1. Non-zero cross-hand correlation products occur for unpolarized flux in the case of an interferometer involving non-similar antennas or for antennas with non-orthogonal outputs or both. In the former case, the LR product is the negative conjugate of RL and is distinct from the true polarized intensity from the source in which the two products form a complex conjugate pair. The instrumental correlation products that result from the lack of orthogonality between antenna outputs are referred to as instrumental polarization, form a conjugate pair and therefore cannot be distinguished from true source polarization.

2. All interferometers of an array of the type considered here can only exhibit a zero cross-hand correlation if all antennas involved are identical in their polarization characteristics and provide orthogonal outputs.

3. Given an orthogonal, homogeneous array as described in (2) above, the fraction of total polarized flux density measurement will be correct. If the antenna polarizations are unknown but near circular the error associated with polarization measurement, in the presence of linearly polarized flux density only, will be small as described in section 3.1.3 and figure (3.2).

4. Accurate measurement of circular polarization in the presence of linear, or conversely linear polarization in the presence of circular, requires exactly circularly polarized antennas (or antennas of known polarization).

5. Determination of position angle of the linearly polarized part of the flux requires zero phase difference between LHCP and RHCP channels of the array.

This array, in reality, does not possess the above qualities so that corrections must be applied to the measured visibilities in order to achieve a high level of performance. The correction process will be dealt with later.

3.2 Calibration Methodology

The polarization ratios and channel gains form, either individually or as some combination, a set of constants referred to as *calibration coefficients* that are applied to the raw instrument data in order to relate these data to the true visibilities associated with the source. The calibration coefficients are determined by essentially applying a set of known coherency elements and intensity to equations (3.1) to (3.4) and solving for the polarization ratios and gains associated with the various channels. The coherency terms are obtained by observing one or more *calibration sources* of known polarization and intensity at the map phase centre. A complex system of $2n(n-1)$ equations with $2n$ unknowns is formed but sufficient information may not be available to allow a complete determination of these unknowns or at least may not be available simultaneously to allow a solution to be performed in a single operation. Moreover, practical considerations such as the existing flow of data within the system, stability with time of some of these coefficients and time required to obtain complete data for their determination dictate the need for a calibration procedure in which complete determination of the coefficients occurs over several operations. Complete knowledge of the calibration coefficients is not required for some forms of observation such as the total intensity or linear polarized intensity which alleviates the need to invest the time in procuring all the calibration data required for their solution. This flexibility is an advantage of this incremental approach. The general telescope calibration procedure is composed of four distinct operations each obtaining some information on the total set of calibration coefficients to some reasonable level of approximation. Potential exists to improve the accuracy associated with these components by successive iterations of the basic calibration operations, although at the time of this writing only a single pass calibration is performed.

3.2.1 Channel gain calibration

Data required for calibration of the channel gains is obtained by observation of an unpolarized calibrator and recording the resulting LL and RR products. The cross-polar coherency elements, ρ_{LR} and ρ_{RL} , in this case are zero and the co-polar elements are equal. Replacing the co-channel coupling coefficients, l_L and r_R, with the channel gains and substituting the appropriate coherency elements in equations (3.1) and (3.2) yields

$$LL_{ij} = I_T g_{Li} g^*_{L_j} \left(r^*_{L_i} r_{L_j} + 1 \right) \simeq I_T g_{Li} g^*_{L_j} \left(\frac{1}{q^*_{L_i} q_{L_j}} + 1 \right) \tag{3.28}$$

$$RR_{ij} = I_T g_{R_i} g^*_{R_j} \left(1 + l^*_{R_i} l_{R_j}\right) \simeq I_T g_{R_i} g^*_{R_j} \left(1 + q^*_{R_i} q_{R_j}\right) \tag{3.29}$$

where I_T is the total intensity of the calibrator source.

For nearly circularly polarized antennas, the terms containing the opposite hand polarization are small and are dropped from the first pass of this calibration operation. Dividing the left hand side by the total flux yields

$$\frac{LL_{ij}}{I_T} = g_{L_i} g^*_{L_j} \tag{3.30}$$

$$\frac{RR_{ij}}{I_T} = g_{R_i} g^*_{R_j} \tag{3.31}$$

from which the individual gains associated with each channel can be solved.

The right and left channel gains are solved for independently because they appear only in the equations involving the products RR and LL respectively. It can be seen by inspecting equations (3.30) and (3.31) that multiplying either the right or left channel gains for the entire array by a complex gain of unity magnitude and arbitrary phase cannot affect the solution. In order to provide a unique solution, the phase associated with one of the antennas is set to some arbitrary number. This phase is the *array reference phase* associated consistently with one antenna of the array and usually set to zero. There will be a separate reference phase for both right and left channels since the two are independently determined.

In anticipation of later discussion, it is required to have only one of these channels as the phase reference and in order to accommodate this requirement, the quantity hereafter referred to as the *cross-polar reference phase* is introduced. This phase is the difference between two channels of opposite polarization associated with an arbitrarily chosen reference antenna of the array. Thus,

$$\theta_{xref} = \arg\left(g_{R_{ref}}\right) - \arg\left(g_{L_{ref}}\right) \tag{3.32}$$

where the subscript *ref* refers to the reference antenna of the array. The single channel reference gain for any antenna of the array can now be expressed in terms of those, G_R and G_L respectively, with independent right and left reference phases. Using the LHCP channel as the single phase reference,

$$g_{R_i} = G_{xref} G_{R_i} \tag{3.33}$$

or using the RHCP channel as the single phase reference,

$$g_{L_i} = G^*_{xref} G_{L_i} \tag{3.34}$$

where G_{xref} is the *cross-polar reference gain*, a complex number of unit magnitude and phase, θ_{xref}.

The number of complex unknowns is n, the number of antennas, while the number of equations is $n(n-1)$. The system of equations (3.30) and (3.31) is solvable for three or more antennas and is overdetermined so that there is no exact solution.

The procedure adopted here will seek the least squares solution to the system. That is to say that channel gains are found such that the residuals, d are minimised in

$$\Delta d = \sum_{i=1}^{n}\sum_{j=1}^{n} W_{ij}\left(G_{X_i}G^{*}_{X_j} - \frac{XX}{I_T}\right)^2 \tag{3.35}$$

where X designates either R or L and W is a weighting factor to account for baselines that are either noisy or missing from the solution. The level of the residuals should be consistent with the thermal noise of the system.

3.2.2 Channel orthogonality calibration

The strategy employed in determining coefficients that affect the polarization orthogonality between channels of the array involves observing an unpolarized calibrator as in section 3.2.1 and solving equations (3.3) and (3.4) for coefficients that result in the observed LR and RL products. This operation is referred to as *orthogonality calibration* since non-zero cross-polar correlation is a result of non-orthogonality of either antennas or baselines.

Dividing the left hand side of equations (3.3) and (3.4) as applied to an unpolarized calibrator by the channel gains and total intensity yields

$$\frac{LR_{ij}}{I_T G_{L_i} G^{*}_{R_j}} = \frac{G^{*}_{xref}}{q^{*}_{L_i}} + G^{*}_{xref} q_{R_j} \tag{3.36}$$

$$\frac{RL_{ij}}{I_T G_{R_i} G^{*}_{L_j}} = \frac{G_{xref}}{q_{L_j}} + G_{xref} q^{*}_{R_i} \tag{3.37}$$

where the baselines are numbered as described in section 2.2.2. Antenna 1 is the westmost antenna of the array.

The quantities IX , the instrumental contribution to the cross-hand products, and x_U , the cross-polar calibration coefficient associated with an unpolarized calibrator, are introduced to simplify notation. The subscript U will designate association with an unpolarized calibrator. The above two equations now become

$$IX_{lr_{ij}} = x^{*}_{U_{rl_i}} + x_{U_{lr_j}} \tag{3.38}$$

$$IX_{rl_{ij}} = x_{U_{rl_j}} + x^{*}_{U_{lr_i}} \tag{3.39}$$

where

$$x_{lr} = G^{*}_{xref} l_R \simeq G^{*}_{xref} \frac{l_R}{r_R} = G^{*}_{xref} q_R \tag{3.40}$$

$$x_{rl} = G_{xref} r_L \simeq G_{xref} \frac{r_L}{l_L} = \frac{G_{xref}}{q_L} \tag{3.41}$$

Equations (3.38) and (3.39) taken together form a linear system of equations $IX = \mathbf{A}\mathbf{x}$ which can be solved for the coefficients within certain constraints. The

coefficient matrix, $\mathbf{A}$, is non-invertible and therefore this system has no unique solution unless at least one of the elements of $\mathbf{x}$ is specified and a minimum of three antennas is involved. This is consistent with the findings of section 3.1.5 since zero cross-polar correlation products are nothing more than a special case of the above system of equations. Defining one of the coefficients as a reference and setting it to zero provides a solution for the entire array relative to this reference. The coefficients are directly related to the antenna polarizations by (3.40) and (3.41) so that this solution provides the polarization for each antenna of the array relative to one channel of an arbitrarily chosen antenna.

In the case of the seven element array at DRAO this system of linear equations is overdetermined and may be solved by minimising the rms value of the residuals as was done for the channel gain solutions of section 3.2.1. Thus,

$$d_{LR} = \sum_{i=1}^{n}\sum_{j=1}^{n} W_{ij}\left[\frac{LR_{ij}}{I_T G_{L_i} G^*_{R_j}} - \left(x^*_{U_{rl_i}} + x_{U_{lr_j}}\right)\right]^2 \tag{3.42}$$

and

$$d_{RL} = \sum_{i=1}^{n}\sum_{j=1}^{n} W_{ij}\left[\frac{RL_{ij}}{I_T G_{R_i} G^*_{L_j}} - \left(x_{U_{rl_j}} + x^*_{U_{lr_i}}\right)\right]^2 \tag{3.43}$$

are minimised.

3.2.3 Cross-polarization reference phase determination

Knowledge of the cross-polar reference gain is essential in the measurement of the position angle associated with linearly polarized flux. This information is essentially obtained by applying coherency elements of a linearly polarized calibrator source of known position angle to equations (3.36) and (3.37) solving for G_{xref}. However a somewhat less direct approach is taken in order to work within practical constraints imposed by existing data flows within the existing software. Cross-polar calibration coefficients associated with a polarized calibrator, designated x_P , are obtained in an identical manner to their unpolarized counterparts of section 3.2.2 except for the observation of the polarized as opposed to an unpolarized calibrator. Analogous expressions to (3.38) and (3.39) are respectively,

$$PX_{lr_{ij}} = x^*_{P_{rl_i}} + x_{P_{lr_j}} \tag{3.44}$$

$$PX_{rl_{ij}} = x_{P_{rl_j}} + x^*_{P_{lr_i}} \tag{3.45}$$

Examination of the steps taken to derive equation (3.38) and (3.39) from (3.3) and (3.4) reveal that the baseline cross-polar instrumental contribution associated with the polarized calibrator, PX, is related to its unpolarized counterparts in (3.38) and (3.39) respectively by

$$PX_{lr} = IX_{lr} + 2\rho_{RL} G^*_{xref} \tag{3.46}$$

$$PX_{rl} = IX_{rl} + 2\rho^{*}_{RL} G_{xref} \tag{3.47}$$

Solving (3.46) for the cross-polar reference gain yields

$$G_{xref} = \left(\frac{PX_{lr} - IX_{lr}}{2\rho_{RL}} \right)^{*} \tag{3.48}$$

and similarly for (3.47),

$$G_{xref} = \left(\frac{PX_{rl} - IX_{rl}}{2\rho^{*}_{RL}} \right) \tag{3.49}$$

Equations (3.48) and (3.49) may be combined as an average,

$$G_{xref} = \left(\frac{PX - IX}{2\rho^{*}_{RL}} \right) \tag{3.50}$$

where

$$IX = \frac{IX^{*}_{lr} + IX_{rl}}{2} \text{ and } PX = \frac{PX^{*}_{lr} + PX_{rl}}{2} \tag{3.51}$$

Hence the cross-polar reference gain can be calculated from the cross-polar calibration coefficients of a calibrator pair made from an unpolarized and a polarized observation. Moreover the polarized coefficients are obtained by an identical operation to that of the unpolarized version.

3.2.4 Array polarization calibration

The solution for antenna polarization in 3.2.2 provides circular polarization ratios that are consistent with only orthogonality and similarity constraints. This solution is not unique as any single one of the antennas could have any arbitrary polarization without affecting the solution. Another way to state this is that the polarization of all the antennas of the array are solved for relative to the polarization of a selected reference antenna. This polarization is referred to as the array polarization and can be determined by observation of two polarized calibrators and then solving equations (3.1) to (3.4) for the polarization ratio. The information required for this solution is contained within the second order terms of this expression that were excluded in the first iteration of the calibration process. Contribution from these terms is small if the array polarization is near to circular as demonstrated in section 3.1.3 so that much data is required to achieve a high enough signal to noise ratio to allow its measurement within a reasonable degree of confidence. Calibration of array polarization was not implemented at DRAO at the time of this writing with the result that

1. small errors occur in the measurement of linear flux (see figure (3.2)) and
2. a small amount of circular polarization is observed because linear flux is converted to circular.

The feasibility of calibrating the instrument for array polarization has yet to be investigated but it is expected that the antenna polarization is temporally stable and that enough data could be collected over time to allow an infrequent but periodic calibration of this type to be performed. Observations of cross-polarized calibration coefficients over time attest to the stability of antenna polarization. Such an investigation is of low priority because the errors resulting from lack of array polarization correction are considered acceptably small.

3.2.5 Visibility data correction

The telescope output products are obtained by replacing the product $I\rho$ in equations (3.1) to (3.4) with the source visibility and the co-channel coupling coefficients, l_L and r_R, with the channel gains. This operation essentially restores the visibility products as presented in chapter 2 equations (2.87) to (2.90) except for the presence of the second order terms. The antennas are near circular in polarization so that some of the terms of these equations contribute negligibly and are therefore omitted from further discussion. Since an array polarization calibration is not performed there is insufficient information to solve the entire set of equations for the desired visibilities. However a very good approximation to the true visibilities can be obtained by correcting the channel gains and subtracting the spurious cross-products, due to poor antenna orthogonality and differences between antennas, from the instrument response. Solving (2.87) to (2.90) for the visibilities yields

$$2\vartheta^{\bullet}_{LL}(\mathbf{r}) = \frac{LL_{ij}(\mathbf{r})}{G_{L_i}G^{\bullet}_{L_j}} \tag{3.52}$$

$$2\vartheta^{\bullet}_{RR}(\mathbf{r}) = \frac{RR_{ij}(\mathbf{r})}{G_{R_i}G^{\bullet}_{R_j}} \tag{3.53}$$

$$2\vartheta^{\bullet}_{LR}(\mathbf{r}) = G_{xref}\left(\frac{LR_{ij}(\mathbf{r})}{G_{L_i}G^{\bullet}_{R_j}} - I_T(\mathbf{r})\,IX_{lr_{ij}}\right) \tag{3.54}$$

$$2\vartheta^{\bullet}_{RL}(\mathbf{r}) = G^{\bullet}_{xref}\left(\frac{RL_{ij}(\mathbf{r})}{G_{R_i}G^{\bullet}_{L_j}} - I_T(\mathbf{r})IX_{rl_{ij}}\right) \tag{3.55}$$

with the gains as described in section 3.2.1 and the second order terms ignored. The quantity IX is defined in equations (3.38) and (3.39) of section 3.2.2. The cross-polar reference gain, G_{xref}, applies to the selection of the RHCP channel for the phase reference of the array. According to equation (3.33) this quantity should be conjugated in the above expressions if the LHCP channel is selected. The total intensity is calculated by

$$I_T = \frac{1}{2}\left(\vartheta^{\bullet}_{RR}(\mathbf{r}) + \vartheta^{\bullet}_{LL}(\mathbf{r})\right) \tag{3.56}$$

The cross-polar instrumental contribution, IX can also be derived from calibration coefficients of polarized calibrators according to equations (3.46) and (3.47) and then be applied to (3.54) and (3.55) above. The cross-polar reference phase is

required in order to subtract the calibrator source polarization, but a close approximation based on the previous calibration may be used with an acceptably small error.

3.2.6 The implementation details

The calibration and data correction methods described above were programmed into system software. Many of the data paths and related structures were already in place before the development of the polarimetry related software, which determined, to some extent, the overall form of the latter. The calibration of channel gain and correction to the LL and RR visibilities were already in routine use (at least for the older four element system that existed before the instrument upgrade) leaving the orthogonality calibration, the cross-polar reference phase calibration and associated data correction as new development. Some of the highlights of this software are briefly discussed in the following.

3.2.7 Overview of the calibration and correction process

Refer to figures (3.8) and (3.9) for this discussion. The overall software system depicted applies at the time of writing but some components are under final stages of development and subject to change. Figure (3.8) represents data collection and calibration steps and figure (3.9) the data correction (i.e. application of calibration information to the raw data) and map making process. Software modules that perform key processes leading to calibrated visibilities are shown with reference to the associated equations of this chapter. All processes are performed independently for each of the four bands (designated A,B,C,D) up to the point where the u-v data is transformed to the map plane. Data from each band is separately gridded in the u-v plane and one map computed. The process of applying the calibration coefficients to the raw data is traditionally referred to at DRAO as *phase1* while the modules that convert the calibrated visibilities to I, Q, U and V maps comprise *phase2* and are shown collectively by one box in figure (3.9).

The collection of data pertaining to the creation of a map is referred to as a survey. A full survey exploits the complete capabilities of the ST and results in a map meeting the published specifications. A map may be made of an object utilizing less than the full set of survey data but with a compromised signal to noise ratio and possible reduction of image fidelity. A brief description of the full survey follows.

A full survey requires 12 days over which time antennas 2,3 and 4 are moved daily to provide a total of 141 spacings for the entire array. The unit spacing is $\frac{30}{7}$ metres, the minimum physically possible is 3 and the maximum is 144. Spacings formed from fixed antennas are constant throughout the survey at 36, 72, 108 and 144. Spacings 12 and 24 also repeat frequently. Samples are collected at 90 second intervals over 12 hours resulting in 480 samples per survey day. Errors are flagged and the flagged data are excluded in the mapmaking process. Gain calibrators are observed for typically 0.5 to 1.0 hours before and after (if possible) the daily data collection. Both should be unpolarized for best polarization results. Data is averaged for the whole calibration interval after flagging and then normalised to

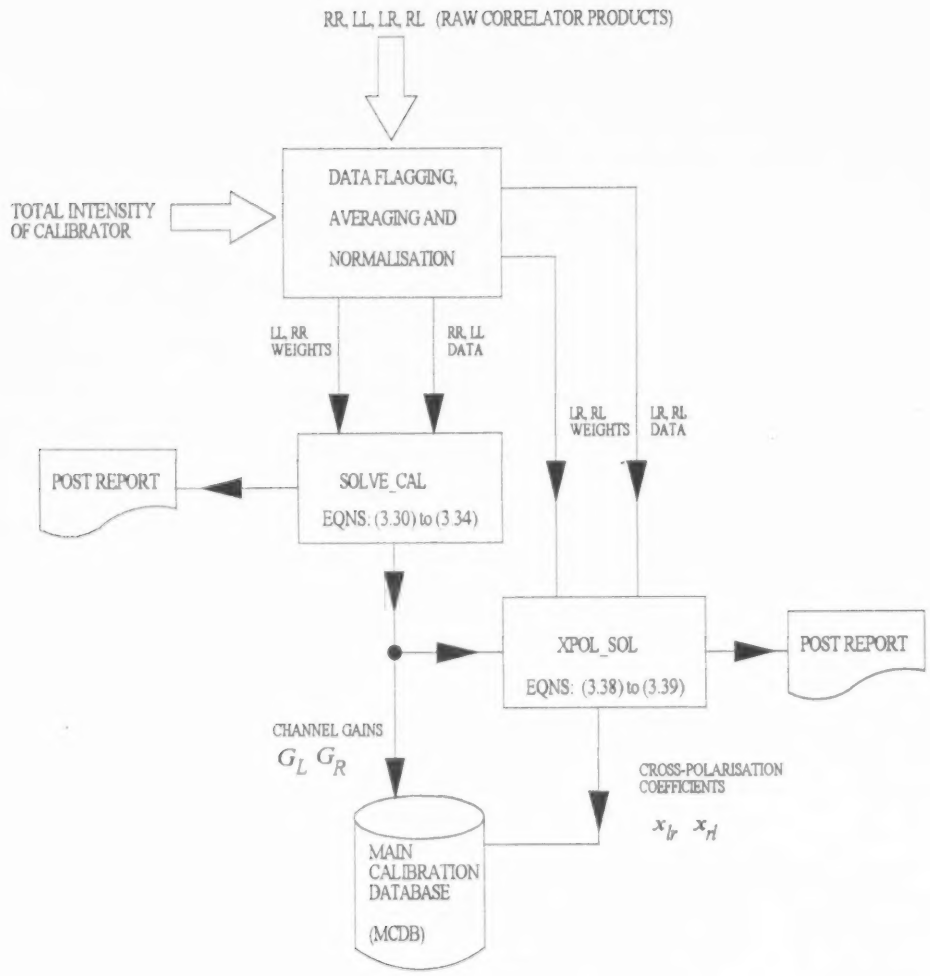

Figure 3.8: A flow diagram of the data collection and telescope calibration steps. The subroutine XPOL_SOL is based on the development described in this thesis.

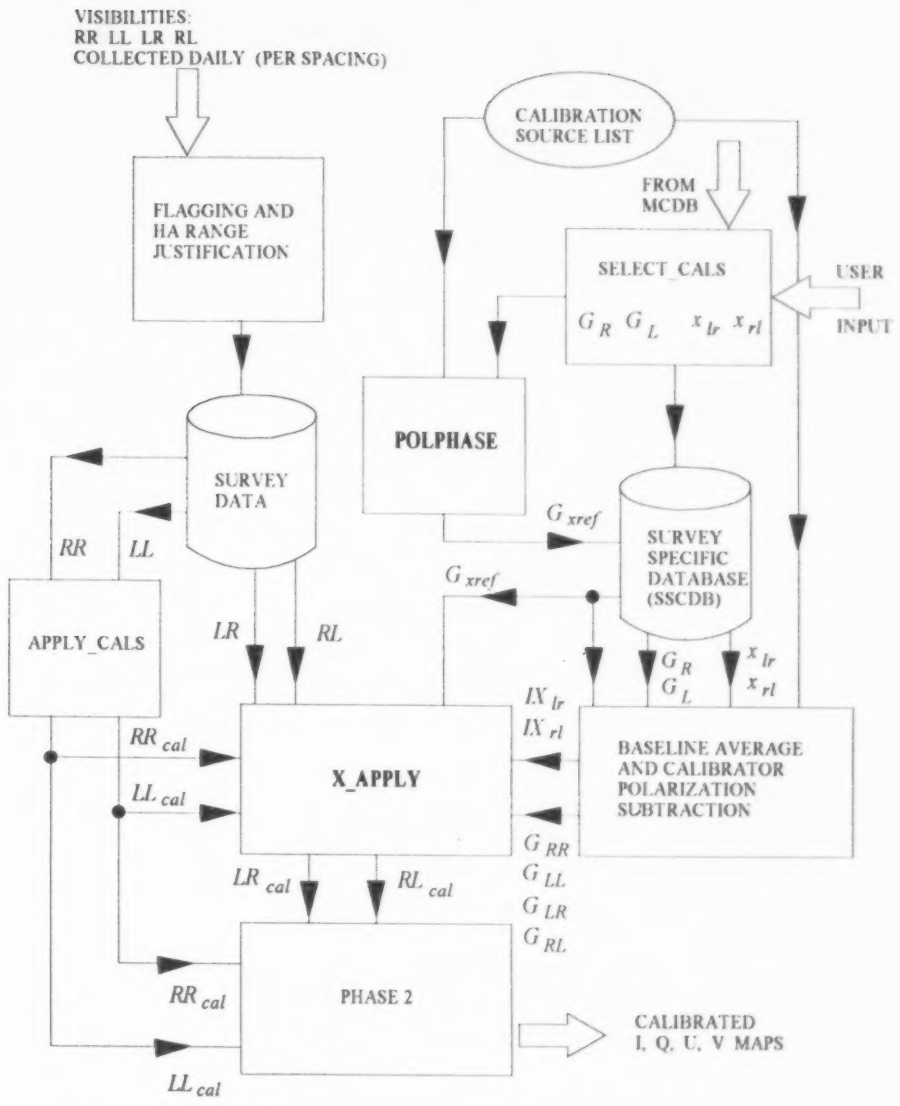

Figure 3.9: Application of calibration coefficients to the data. The subroutines X_APPLY and POLPHASE were developed as part of this thesis. The majority of the other subroutines depicted were modified to accommodate polarimetry.

the known intensity of the calibrator. All calibration coefficients go into the main calibration database which accumulates all calibrations of the ST.

During *phase1* (see figure (3.9)) calibration coefficients are selected and extracted from the main calibration database (hereafter MCDB) according to days pertaining to the survey and this subset makes up the survey specific calibration database. Selection is performed via the module SELECT_CALS which bases its selection on various criteria most notably, a time window encompassing the survey day. SELECT_CALS seeks, if possible, a pair of calibrations that brackets the daily observation. Calibrations are applied to data by forming the gain products and cross-polar sums per baseline and then averaging these for the pair. If the calibrators are polarized then coefficients are corrected by removing the known source polarization according to equation (3.46) and (3.47) before application to data. The principal HA range is 18 to 6 hours as discussed in section 2.2.2 so that data collected outside this range must be processed (HA range justification) according to the procedure in section 2.2.1.

Phase2 places visibilities on a u-v grid and then invokes an inverse Fast Fourier Transform (FFT) algorithm to yield a 1024x1024 element (pixel) map. The Stokes parameter map elements are calculated according to equation (2.40). A facility (WRITEFITS) is included to export u-v data in the form of FITS (Flexible Image Transport System) files. The Stokes U, in this case, is conjugated for compatibility with AIPS which calculates the U elements according to equation (2.41) (see the discussion in section 2.2.1 and 2.2.8).

3.2.8 Channel gain calibration

The channel gain coefficients are determined by the module SOLVE_CAL in figure (3.8) which is based on the CPSLSS (Complex Product System of Equations, Least Squares Solution) algorithm employed at the VLA. This is an iterative scheme which minimises the least squares difference between original data and data recreated from the coefficients as in equation (3.35)(see section 3.2.1).

3.2.9 Channel orthogonality

The cross-polar coefficients are found by an iterative process, similar to that for the channel gains (SOLVE_CAL), applied to equations (3.36) and (3.37) of section 3.2.2. The coefficients provided by the process are described in equations (3.40) and (3.41). A fundamental distinction between the gain calibration (SOLVE_CAL) and cross-polar coefficient solution (XPOL_SOL) is that the latter requires both correlator products, LR and RL, for solution.

The unconstrained solution search results in a solution where an arbitrary constant k is applied to one of the coefficients and $-k^*$ (negative conjugate) is applied to the other. In order to provide a unique solution for diagnostic monitoring, the cross-polar coefficient, x_{lr} of the phase reference antenna is set to zero by subtracting x_{lr} from all of the x_{lr} array coefficients and likewise subtracting $-x_{lr}^*$ from all of the x_{rl} coefficients. The results are written to the MCDB and expressed in percent within the generated *post reports*.

3.2.10 Cross-polarization reference gain

The cross-polar reference gain, G_{xref} (hereafter CPRG) is calculated according to equation (3.50) and is done independently of the survey. When survey data are reduced, SELECT_CAL will seek a list of polarized /unpolarized pairs from the MCDB according to various criteria such as

1. ignoring calibrations involving the shortest baseline (13 m) (coupling between antennas can corrupt the calibration results),
2. allowing for a tolerance on the spacing, days, and other criteria as done with gain,
3. spanning the survey date range.

The module SELECT_CALS invokes POLPHASE (a user interactive facility) to calculate an average of G_{xref} over all 21 baselines providing these values are consistent with each other. The entire survey selections are then averaged and one value for the CPRG is provided to represent the survey and stored in the survey specific database. In addition reasonable defaults are stored in a hardware parameters database and made available to SELECT_CALS if none is available for a particular survey or if the user elects not to invoke POLPHASE. A further default of unity magnitude and 180 degrees phase is used by *phase1* if CPRG calibration is completely bypassed by the SELECT_CALS options.

3.2.11 The calibration database

The MCDB contains various telescope parameters provided by the calibration observations over time and is cumulative. In addition to the channel gains and cross-polar coefficients, as discussed above, the MCDB contains the time of the calibration, the HA start, the exact antenna positions (in x,y, z metres), the time of day of the calibration, the source name, and various other system corrections for both continuum and spectral line modes of operation. The MCDB is a useful tool for diagnostic purposes and for further research into instrument operation.

3.2.12 Calibration sources

Sources suitable for the calibration of channel gain should exhibit low polarization (under 10 %), and for the calibration of orthogonality, should be unpolarized or less than 0.2 % polarized (in order to exploit the full capabilities of the instrument). Unpolarized sources may not be visible for a particular field so that sources with low levels of polarization will, on occasion, be employed for orthogonality calibration. Provisions to subtract the source polarization before correction to data are in place but uncertainties in the polarization properties of many potential calibrator sources and the fact that the CPRG is an integral part of the cross-polarization coefficients increase the potential for error in the calibration process. It is therefore important that one of the calibrators of a pre-observation and post-observation pair is unpolarized, and the other, one whose properties are at least well established.

	position reference	total intensity (Jy)	polarized intensity (% of I_T)	IPA ($degrees$)	RM (rad/m^2)
3C286	1328+307	14.73	9.2 +/- 0.5	33 +/- 1	-1.2 +/- 0.8
3c138	0518+165	8.6	7.2 +/- 0.5	-10 +/- 1	-2.1 +/- 0.7
3C48	0134+329	15.76	0.5 +/- 0.5	119 +/- 9	-66.6 +/- 4.4
3C147	0538+498	20.7	< 0.1	n/a	n/a

Table 3.2: Sources used for polarimeter calibration.

Calibration of the CPRG phase requires two sources; one whose position angle (PA) is well known and a second whose fraction of polarization is zero or at least a very much smaller than that of the polarized companion.

An investigation into the availability of and polarization characteristics of various calibrators is presently under way, but for the research involved in this thesis, the calibration sources in table (3.2) were employed. Source 3C286 provided the most consistent polarization characteristics in the literature particularly in regard to the position angle. 3C147 is completely unpolarized down to the limits of present instruments and is perhaps the best source available for orthogonality calibration.

Some flexibility is afforded in scheduling CPRG calibrations and it should always be possible to use 3C286 as the polarized calibrator. It is not always possible to use 3C147 as a source for both pre-observation and post-observation orthogonality calibrations but 3C48 has been employed as one of the calibrators in these cases. This source is only slightly polarized so that imperfect polarization subtraction will produce usable results at least when averaged with an accompanying calibration with 3C147.

Total intensity values for these sources were obtained from the VLA calibration manual, NRAO (1986), and the polarization properties from Tabara and Inoue (1980). Several measurements were listed in Tabara and Inoue (1980) for the fraction of polarization of 3C286 and 3c138. An average of these is used for table (3.2). The observed position angle as a function of wavelength, $\tau_{obs}(\lambda)$, is given in terms of its intrinsic position angle (IPA) and associated rotation measure (RM) in rad/m^2 by

$$\tau_{obs}(\lambda) = RM\lambda^2 + IPA \tag{3.57}$$

The intrinsic value of 33.0° was employed for 3C286 during many of the CPRG calibrations associated with the observations discussed herein. In future work, the RM at 21 cm wavelength should be used to correct the data accordingly.

Calibrators 3c138 and 3C147 exhibit some variability and, in this case, the latest values in the VLA calibration manual are used.

3.3 Verification of the calibration process

Actual test observations of sources have been used to verify that the calibration process is operating as expected. The maps produced from these tests also provide

an initial indication of the level of performance achieved by this polarimeter. However, accurate specifications can only be drawn after extensive experience with this instrument is accumulated. Comparison of the calibration coefficients obtained from source observations have been made with predicted values from antenna laboratory measurements of the feed antennas in order to demonstrate the relevance of the latter to instrument performance.

3.3.1 Sky measurements

Figures (3.10) to (3.13) are plots of the cross-polar calibration coefficients versus time for a sample set extracted from the main calibration database. Figures (3.10) and (3.11) are amplitude plots while the associated phase plotted in degrees is presented in (3.12) and (3.13). The coefficients were based on 3C147 (essentially unpolarized) calibrations and refer to band B of the interferometer. The time represented by the interval between samples is not constant since the choice of calibrators varies between surveys and the samples were selected according to similar HA ranges and local oscillator frequencies. The configuration with the closest spacing (spacing 3) has been excluded and the observation time spent on this calibrator was either 0.5 or 1.0 hours. Nevertheless, increasing sample number represents increasing time and can yield some information on overall trends and value excursions expected in these quantities. They range from February 2, 1993 to December 14, 1993.

Antenna #7 is the reference antenna for which the cross-polar coefficient of the RHCP channel is set to zero although antenna lab measurements suggest that a value of approximately 0.03 would be more representative of this quantity. In order to obtain the true values for the RHCP coefficients the coefficient of antenna 7 is added vectorially to all others and the LHCP would have the negative conjugate added as according to equations (3.14) and (2.58). A jump in the amplitude of several antennas after about the 10th sample point suggests that the reference antenna underwent a change in its polarization characteristics. With exception of this jump, the coefficients appear to be quite stable over time with no apparent trends. The phase as shown in (3.12) and (3.13) exhibits a slow drift with time. This is likely caused by a drift in the CPRG phase (based on antenna 1 up to and including sample 8 and on antenna 5 thereafter) which shows up in these coefficients because they include the CPRG as a factor (see equations (3.40) and (3.41)).

The amplitudes of the channel gains and their phases associated with representative antennas are shown in figures (3.14) to (3.17). They are shown primarily for completeness as they do not appreciably affect the polarization measurements, relative to the total flux measurement. That is to say, the absolute polarized flux will be subject to the same errors and uncertainties as the total flux and a detailed dissertation on these errors is beyond the scope of this document. It can be seen, however, that long term stability of the channel gains is not as good as that of the cross-polar coefficients. Much of this fluctuation is due to modifications and adjustments of the instrument. The difference between the right and left channel phase is shown in (3.18) and reflects the stability of the CPRG phase. The drift apparent in the cross-polar coefficients is visible here. This quantity appears to be quite stable

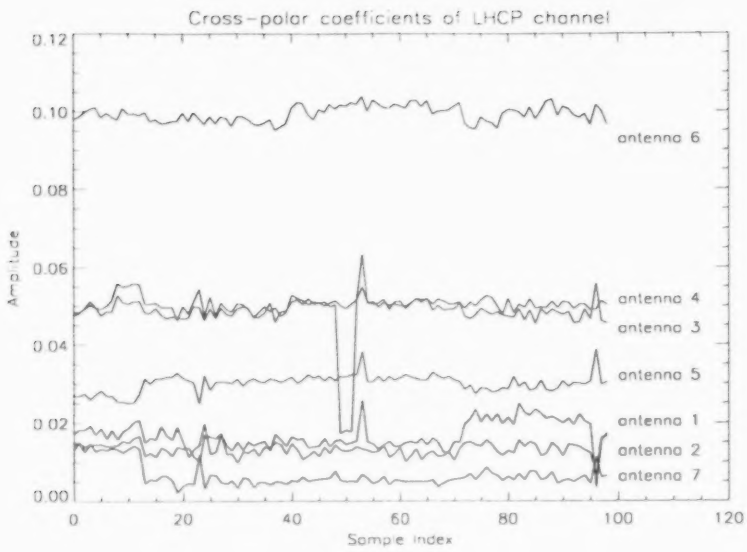

Figure 3.10: A sample of cross-polar coefficients specifying coupling from the RHCP to LHCP channel.

despite somewhat larger fluctuations in the individual channel phases. The channel phases are referenced to antenna 1 up to and including sample 8 and then a switch is made to antenna 5 thereafter as is apparent in (3.18).

Figure (3.19) is a plot of the CPRG phase for band B. Like the previous figures this phase is plotted against sample index as opposed to real time. Two different reference antennas were used between early and recent samples. Samples were selected where the observation of the polarized calibrator was done either well into darkness or well into daylight so that the difference between day and night values of the CPRG could be observed. This difference was anticipated and is due to a change of rotation measure of the ionosphere between day and night. The only other selection criterion was that the shortest spacing was not used. The calibrator pair 3C147 / 3C286 was used for all except for the first six points which used 3C48 / 3C286. An IPA for 3C286 (33°) was assumed whereas a more accurate value would be 30° as suggested in section 3.2.12. A shift of about 10° occurs between day and night observations (5° change in apparent PA). Values from July 24, 1993 to December 10, 1993 are more scattered then others. This could be due to greater variation in calibration parameters such as HA start, since several surveys were observed during this time. It has been observed that local oscillator frequency changes

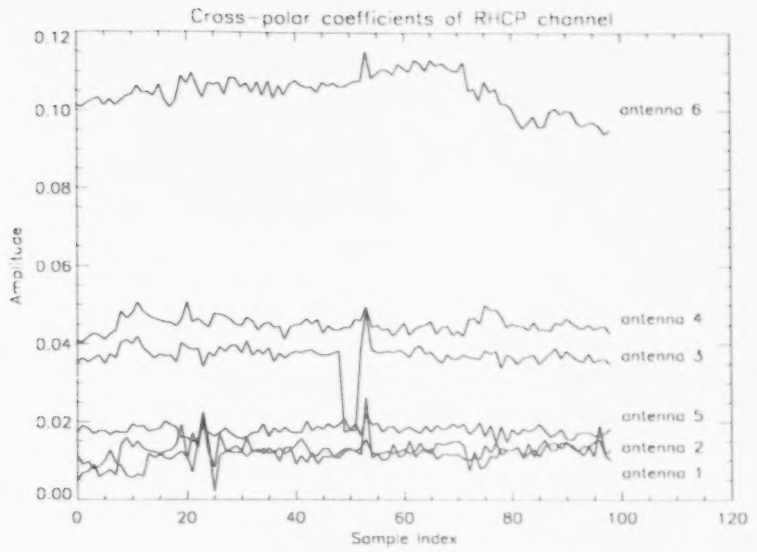

Figure 3.11: A sample set of cross-polar coefficients specifying the coupling from LHCP to RHCP channels. The coupling for antenna 7, the polarization reference antenna, is set to zero.

corresponding to velocity changes greater than 25 km/s result in about a 1 degree phase change (increasing with increasing velocity) in the CPRG which is not significant. HA start time appears to have an effect but this has not been investigated in detail. A programme of instrument adjustment or perhaps greater solar activity during this interval could also be a cause.

Figure (3.20) is an observation taken of the unresolved source 3C380 (1829+487) in order to demonstrate the effectiveness of the calibration and correction procedure and to determine some performance limits of the instrument as a polarimeter. The plots are of the centre 256 × 256 region of the 1024 × 1024 element map since this is where most of the features lie. Contour flux units are in mJy/beam. The instrument was fully calibrated and corrections applied to the top four maps of (3.20). The lower two maps were made with polarization calibration turned off (i.e. only the channel gain calibration was applied). In these cases the I and V maps are unaffected. The DRAO survey name associated with these data is ZJ and was observed for 34.5 hours total over July 15,16 and 17 of 1993, starting in late afternoon and running through the night. A total of 49 different spacings were used. Gain and orthogonality calibration was based on 3C147 observed on July 15 and

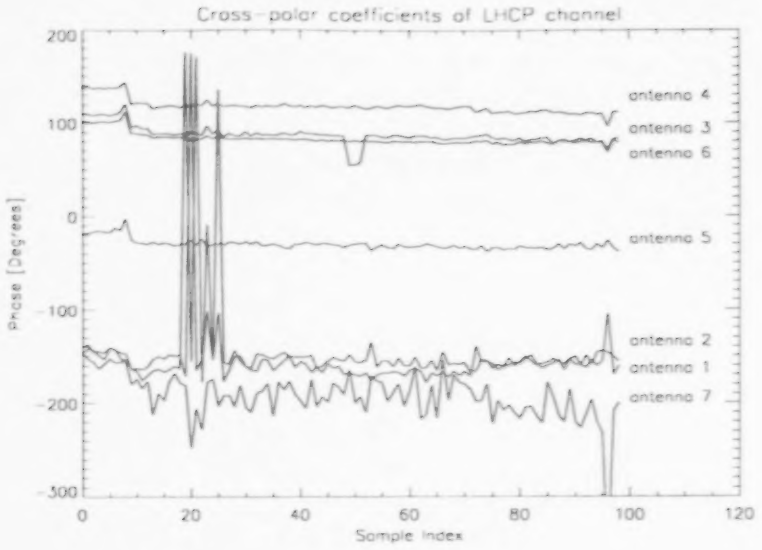

Figure 3.12: Phase of the cross-polar coefficients specifying coupling from the RHCP to LHCP channel.

July 18, averaged and applied to all three days of the survey. The CPRG calibration was based on nearby 3C286 daytime observations. Adding a 5° correction for day - night Faraday rotation yielded -188, -179, -176 and -169 CPRG phases for bands A,B,C and D respectively. The maps were subjected to processing with the CLEAN algorithm to remove artefacts in the image caused by incomplete sampling of the u-v plane. CLEAN is an iterative process in which the effective antenna pattern of the array that results from a particular set of u-v sample points (synthesized beam) is deconvolved from the raw image. The U, Q and V maps were CLEAN'ed until components being removed from the map were less than 2 % of the initial peak value leaving a background noise level in the order of 0.5 to 2.0 mJy/beam depending on the map. The I map was CLEAN'ed somewhat deeper but because of the larger initial peak on the map the background noise was approximately 100 mJy/beam. The specified noise level for a well calibrated, completely CLEAN'ed and fully sampled survey is 0.23 mJy/beam which approaches the thermal noise floor of the system. The peak of the I, Q and U maps at the field centre are 13850, -1.095 and 58.99 mJy/beam respectively.

The source 3C380 exhibits a total flux of 14.2 Jy at 20 cm according to NRAO (1986), a fraction of polarization in the range of 0.6 to 2 %, an intrinsic position

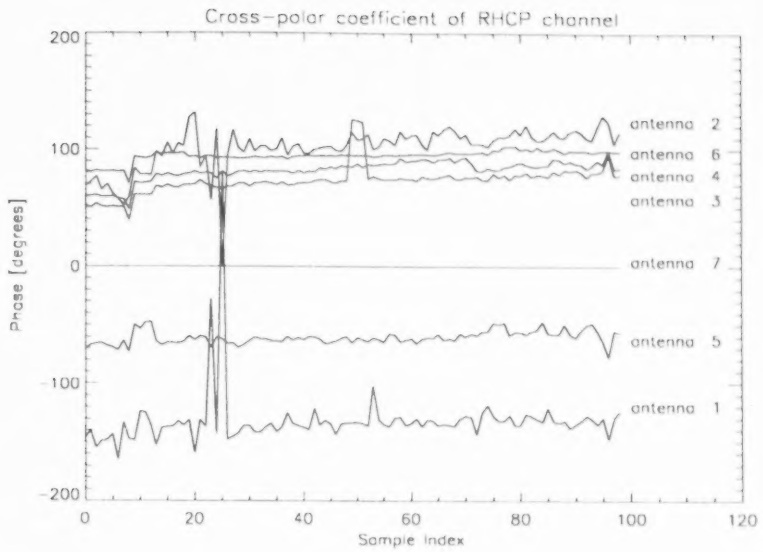

Figure 3.13: Phase of the cross-polar coefficients specifying coupling from LHCP to RHCP channels.

angle of $5° \pm 6°$ and rotation measure of 21 ± 3 rad/m^2 according to Tabara and Inoue (1980). At 21.0 cm wavelength this results in an observed position angle in the range 44° to 72°. The observed PA is 46° (40° to 46° if the associated RM measure and uncertainties of 3C286 are accounted for) and the source is 0.43% polarized. The observed polarized fraction is somewhat lower than the published value and the position angle lies at the lower extreme of the range. The U map is dominated by the source polarization whereas the Q map exhibits the negative symmetry expected from differences between antenna polarizations (baseline orthogonality). The high level of this symmetry suggests that the instrumental effects dominate the source in the Q map and that the level of this spurious product might be an indicator of calibration effectiveness, at least for baseline orthogonality. The magnitude of these levels in the Q map is 10 mJy/beam yielding a spurious instrumental level of 0.1 %. The instrumental polarization, on the other hand, is not as obvious since it appears as polarization added vectorially to the true source polarization. The differences between published and observed flux can be either an error in the published flux, multiplicative errors due to uncalibrated antenna polarizations or additive errors due to residual instrumental polarization. Multiplicative errors much greater than 1.2 are unlikely so that leaves either a residual instrumental contribution or incorrect

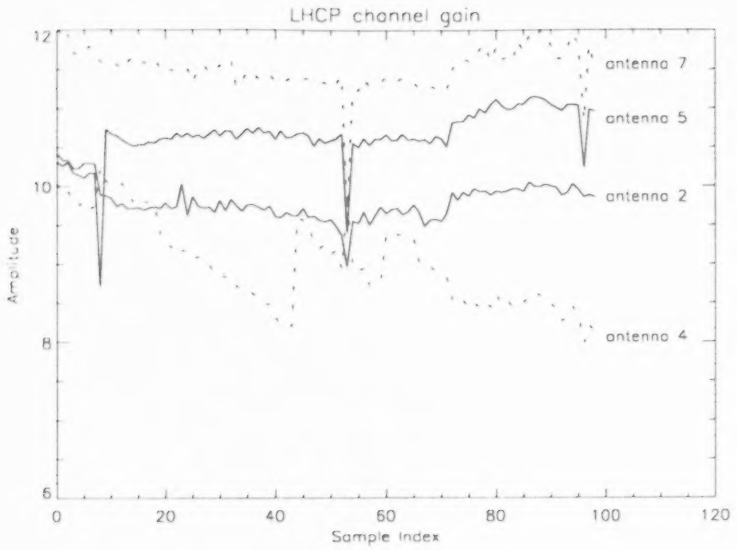

Figure 3.14: Channel gain amplitude for sample baselines.

source polarization as cause of the discrepancy. An instrumental contribution of 0.5% with a 45° phase would place the observed flux and position angle well within the published range. Further discussion of instrument error will be left until section 3.4.

The source is only slightly polarized so nothing is expected in the V map according to the considerations of section 3.1.3. However, since the V map is the difference between calibrated RHCP and LHCP channels, the integrated differences between calibrated left and right channel gains over the course of the observation will cause spurious emission to appear in this map.

The uncalibrated maps demonstrate the need for polarization calibration. Lack of baseline orthogonality completely dominates the source polarization which itself is evident as a small asymmetry in the U map. Although the peak values are only of the order of 1% these effects are distributed over the map so that strong nearby unpolarized sources may have an adverse effect on the observed polarization of weak sources.

Figure (3.21) presents maps of polarized source 3c138 (0518+165). The instrument was fully calibrated and the corrections applied. The maps were created from a single observation, 8.5 hours in duration starting at 0637 PST on the morning of July 18, 1994. Orthogonality calibration was based on a single observation of

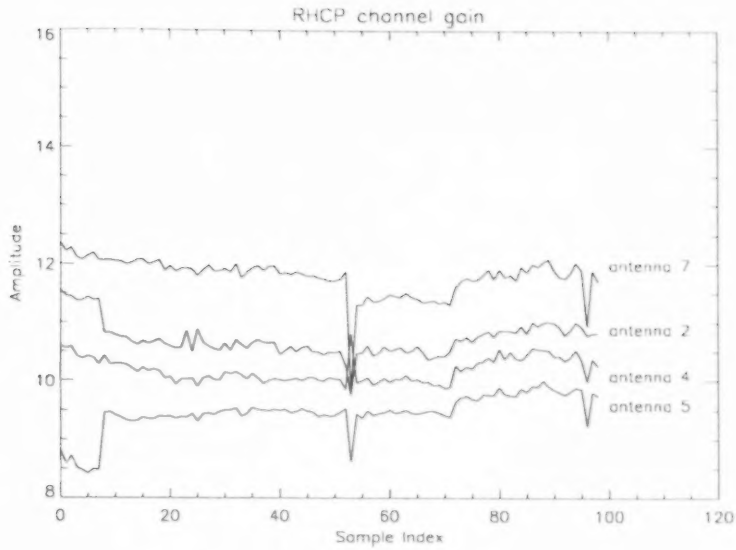

Figure 3.15: Channel gain amplitudes for sample baselines.

3C147 on July 17. PA calibration was based on four daytime observations of 3C147 / 3C286 pairs around this date and provided CPRG phases of -188, -179, -176 and -169 degrees respectively. The object is at a low declination resulting in a highly elliptical synthesized beam due to a foreshortened projection of the track in the north-south direction (v-axis). The image was CLEAN'ed down to a fraction of the starting map peak of 0.5, 2, 5 and 6 % for the I, Q, U and V maps respectively yielding a residual noise level of just under 10 mJy/beam for all maps except the I map for which the level was 100 mJy/beam. The observed fraction of polarization is 7.9% which is 0.2% higher than the upper limit of the published value listed in table (3.2). A PA of $-9.0°$ is obtained from the Q and U maps. Correcting for the RM of the 3C286 calibrator (including the error in PA and RM) according to table (3.2) yields a more accurate figure in the range $-9°$ to $-15°$. The published value for 3C138 is $-12.5°$ to $-18°$ (taking into account RM and associated errors).

Similar tests were performed on source 3C286 as survey H1 observed 1 hour per day for 10 days from June 12 to July 21, 1994 (alternating between 0.8 and 6 HA starts). These observations yielded (for all bands included in the map) 9.27 % as a fraction of polarization. This is well within the published range for this number as tabulated in table (3.2).

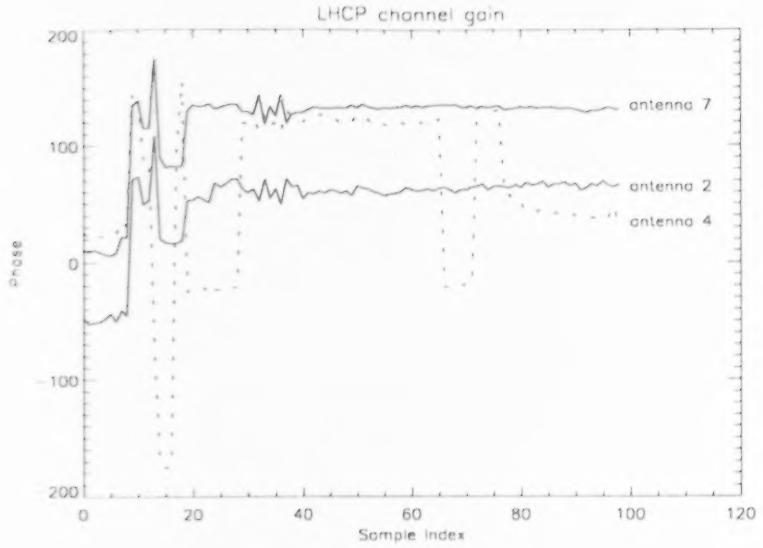

Figure 3.16: Channel phases for sample baselines.

3.4 Noise and Error in Polarization Measurement

An order of magnitude evaluation of errors is attempted bearing in mind that more than two short observations and cursory inspection of the MCDB are required to extract reliable information on polarimeter performance.

Errors resulting from the observation process may be classed according to

1. thermal noise possessing Gaussian statistics;

2. random instrumental noise from non-predictable, non-observation specific variations in instrument parameters due, for example, to random antenna pointing errors (wind and gear train backlash), instrumental changes due to temperature variations, mechanical movement of components such as cables, interference from non-stationary sources;

3. systematic errors which may exhibit a small degree of correlation with observational parameters, for example, inter-antenna coupling, antenna shadowing, solar and fixed position interference, local oscillator frequency settings, and uncorrected systematic errors in antenna pointing.

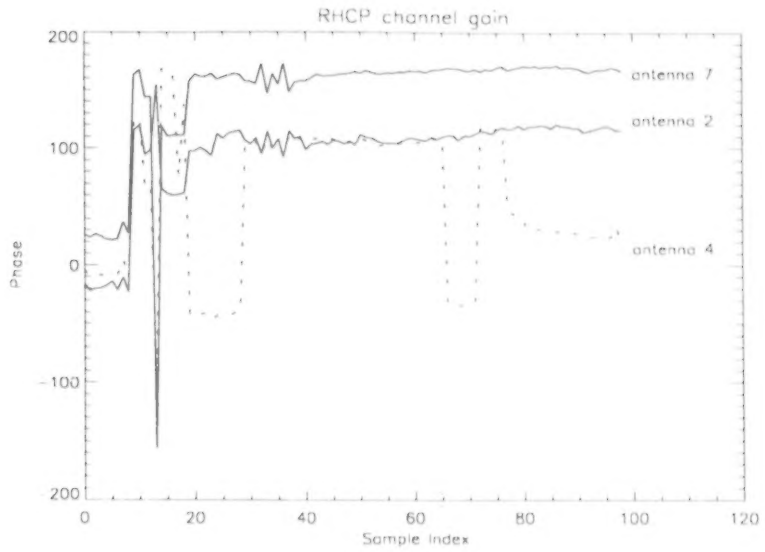

Figure 3.17: Channel phases for sample baselines.

The first two types of errors should decrease with increased observation time, hence, longer calibration times and increasing number of calibrations should reduce the errors in the calibration coefficients used for correction. The third category containing systematic errors is problematical in that these errors may not necessarily decrease with observation time or will vary in some non-obvious manner. Their size is likely dependent on a particular observation and calibrator pair making an overall performance prediction of the instrument difficult. The uncertainty due to thermal noise is predictable and a check of the statistics of the calibration coefficients over a typical survey will suggest some upper limit to the second category of noise related error. Detailed statistical study on a larger number of calibrations, once the MCDB is large enough to support such a study, and other observations similar to those described in the previous section will be required to predict the systematic effects (category three) with any degree of confidence.

Map errors have both an additive and multiplicative component. Consider M to be either the observed Q or U (a fully sampled survey) for a source located near the map centre with total intensity, I_T , and located near a source with peak intensity I_P. The subscript, " o ", signifies the true source quantity. Thus

$$M = e_g e_p M_o + e_{xa} I_T + e_{xb} I_P \tag{3.58}$$

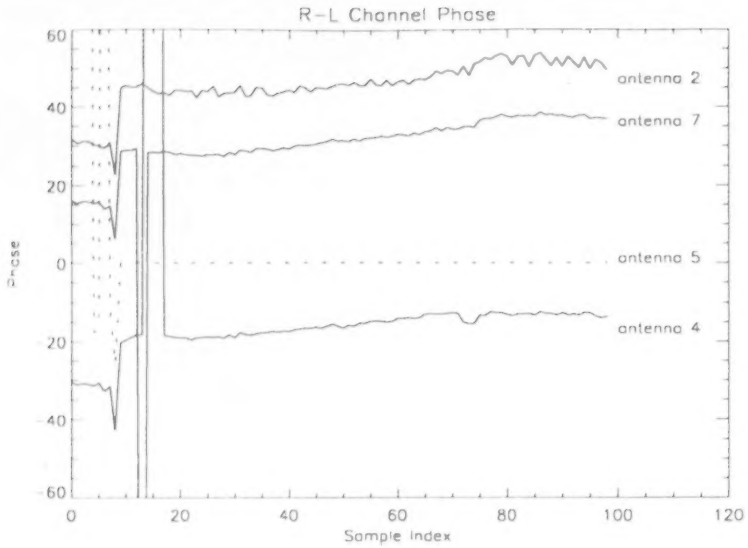

Figure 3.18: The phase difference between the RHCP and LHCP channels for four sample baselines. Antenna 5 is the phase reference and has been set to zero.

Error coefficients e_{xa} and e_{xb} are associated with noise and instrumental instabilities affecting antenna and baseline instrumental contributions respectively. They arise from differences between the true (i.e. that represent the instrument during any point of the survey) and measured cross-polar calibration coefficients that are applied to correct the raw data on a per baseline and sample basis as described earlier. Errors e_p arise from lack of antenna polarization correction and e_g from errors in baseline channel gain products. All three error classifications apply to each of these except for the polarization error which is predominantly constant (with a very small random and systematic variability).

The errors, e_{xa} and e_{xb} dominate in unpolarized sources so that the observation of 3C380 provides an idea as to their size. Bearing in mind that survey ZJ of 3C380 is a three day observation, and that noise and other random contributions to errors will be scaled by a factor $\sqrt{\frac{3}{12}}$ for a full survey, the errors exhibited by this test survey will be approximately, $2e$, or twice the full survey error. The observation of 3C380 suggests that e_{xb} (for a full survey) is on the order of 0.002 (0.2% of the total flux).

The stability of antenna orthogonality is expected to be better than baseline orthogonality, if different at all, on the basis of physical arguments. If antenna

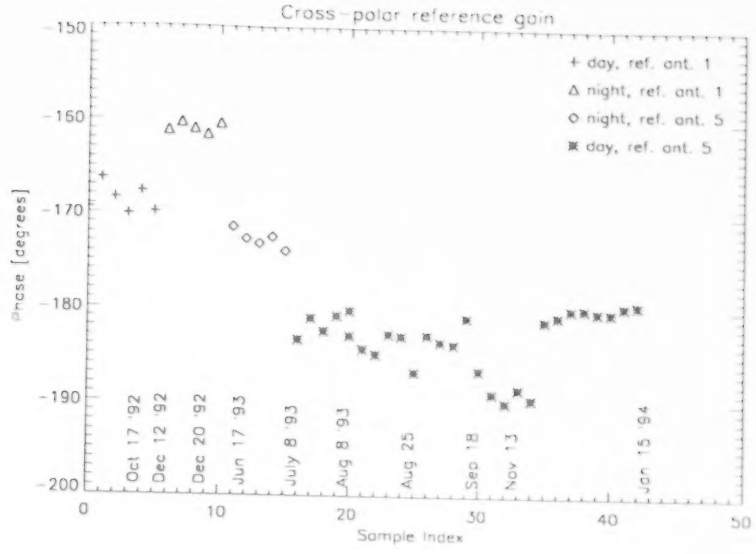

Figure 3.19: The cross-polar reference phase over approximately one year. Distinct night and day observations were selected.

orthogonality is typically better, then of the two quantities, e_{xa} will be smaller. Antenna orthogonality is typically better than its baseline counterpart as can be seen by inspection of figure (3.22) which is a magnitude plot of equation (3.38). For a single antenna this quantity represents the instrumental polarization and would be the fraction of total flux present in a cross-hand correlation while observing an unpolarized calibrator. Data for this plot is derived from the MCDB using the same sample set as plots (3.10) to (3.13) and is believed to represent typical levels. This plot implies that the two lower curves of figure (3.7) represent typical levels of instrumental polarization. In comparison figure (3.6) represents the instrumental contribution due to a worst case, but realistic, level of baseline orthogonality. Levels of spurious instrumental products due to poor baseline orthogonality, represented by e_{xb}, are potentially higher than the antenna based counterpart, e_{xa}. A conservative estimate of error would assume that $e_{xa} = e_{xb}$ and that instrumental polarization is 0.2% of the total flux.

A magnitude of instrumental polarization of 0.2% in both Q and U would result in 0.3% for total polarized flux error. This error just barely enters the published range (0.6 to 1.4). Based on this discrepancy between published and observed flux of 3C380 and accepting the above reasoning there could be a significant systematic

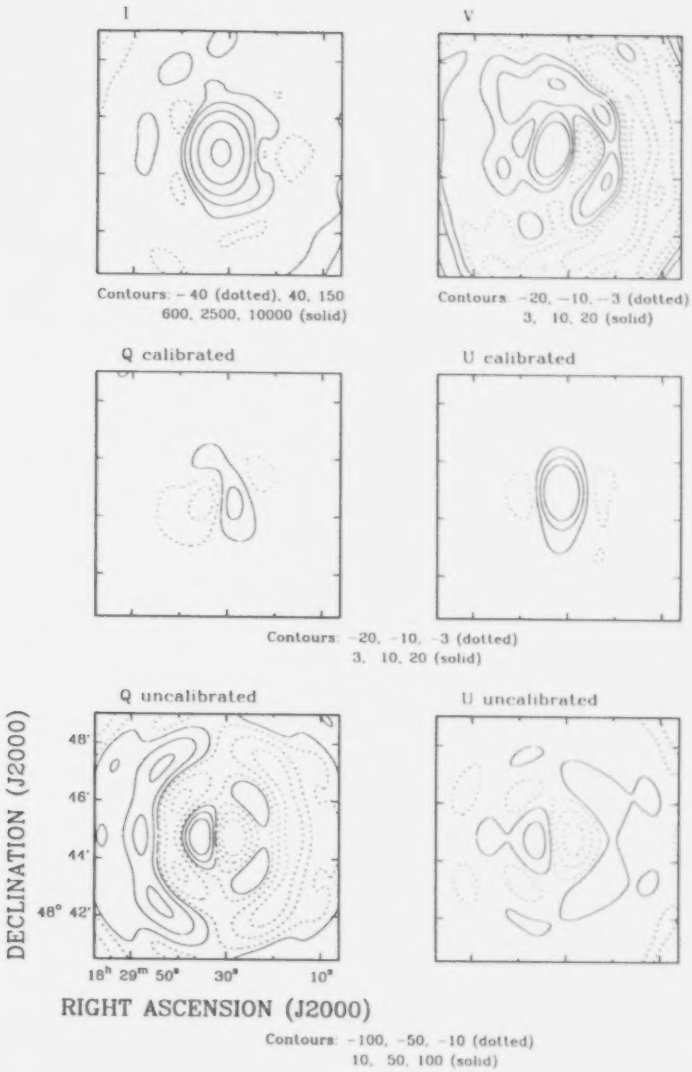

Figure 3.20: Test observation of source 3c380. The polarization calibration was disabled for the lower two boxes. Contour levels are given in units of mJy/beam.

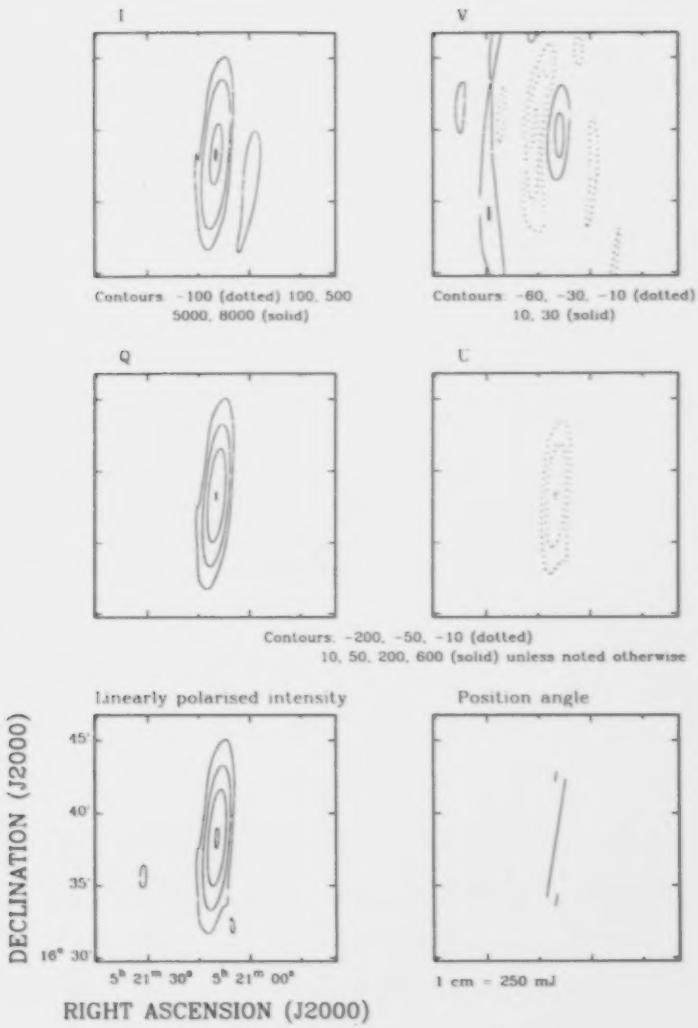

Figure 3.21: Test observation of polarized source 3c138. Contour levels are given in units of mJy/beam.

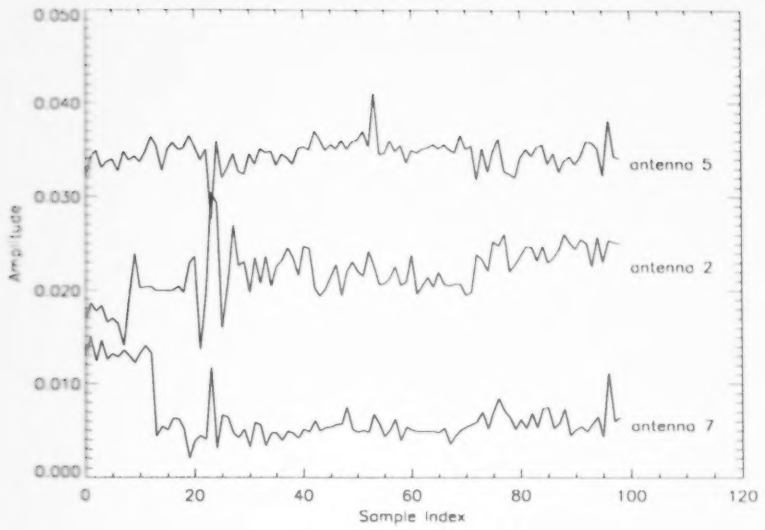

Figure 3.22: A plot of the orthogonality between opposite hand channels of three selected antennas. The best and worst are represented here.

error that affects both e_{xa} and e_{xb} , in this case, decreasing the magnitude of e_{xb}. Until further work is done an error of 0.5% residual flux is placed on these measurements yielding a total polarized flux residual of about $\pm$ 0.7%. That is to say that any source could have Q and U flux added to it that is $\pm$ 0.5% of either its own unpolarized part or the unpolarized part of a source located nearby, whichever is higher. In extended objects, 0.5% of the peak unpolarized intensity of the object should be used. This error is similar to error bars typically placed on published polarization fractions.

The polarization error, e_p can be deduced from considerations of section 3.1.3. Assuming 10% (based on antenna lab measurements) unwanted component in a given channel results in about 1% error in linear flux per baseline according to figure (3.2). Most sources of interest are less than 20% polarized so that 1% of this yields 0.2% of the total flux which is smaller than errors due to residual instrumental polarization. Since,

1. polarization correction is not applied in this instrument, the polarization error for the entire map will be made from all baselines in an operation closely resembling an average and

2. 10% is higher than the typical opposite hand contamination,

the polarization error of the map, e_p, should be much less than 0.01 (or 1% of the polarized flux).

If full polarization correction were applied this error would be determined solely by the reference antenna which, if atypically high and uncalibrated for polarization, could result in higher error than experienced with the present scheme.

The error e_g represents errors in the baseline gain products. The individual channel gains are by their nature expected to exhibit greater variability with time than the cross-polar coefficients and this expectation is justified by inspection of the various gain plots of section 3.3.1. The fraction of polarization is scaled by a factor containing these gains as ratios and products and the consequences of such variations, whether random or systematic, are not readily obvious. Inspection of the gain plots of figures (3.14 and 3.15) suggests that typical fluctuations in channel gain amplitude are confined to less than 5% of the nominal value. Moreover this error is consistent with that required to bring the observed total intensities in agreement with published values. Assuming this variability to be random, the error exhibited by a full survey will be smaller. This notion is supported by the residual flux in the Stokes V map of 3C380 which is seen to be on the order of 1% of the total intensity and, for an unpolarized source, can only be due to variations in the channel gains. Using this value as an initial guess at e_g yields errors in the order of 5% of the Q and U map intensities which is about 0.7% of the total flux in the case of a 10% polarized source or about the same level as the residual instrumental errors. The difference between the published and observed polarized fractions of 3C138 (less than one day observation) is about 0.7% and may be accounted for entirely by the residual instrumental polarization. There is not enough data in the observations presented here to improve the initial estimate e_g.

The position angle errors are determined primarily by the ability of the calibration process to account for ionospheric Faraday rotation. The PA measurement of 3C138 is within 3° of the published value if a simple day - night rotation offset is applied. Without this correction, the error could increase by another 5°. The most significant threat to PA measurement accuracy is anomalous fluctuations in ionospheric Faraday rotation due to enhanced solar activity. The statistics of such events have not been investigated in regard to calibrating this instrument. First order models of this rotation mechanism under normal conditions could be invoked to interpolate rotation between the calibrations and improve the PA measurement accuracy. Error based on PA calibration with simple day - night offset correction is, at present, considered within 5° and within 10° without such correction, barring anomalous solar activity.

3.4.1 Conclusions

1. The calibration process developed in this thesis works as expected and is required to generate acceptable polarization maps.

2. The calibrated instrument functions as an imaging polarimeter and can gen-

erate Stokes Q and U maps with a multiplicative error of 5% of the Q and U flux values and an additive error or instrumental component that is 0.5% of the peak total flux within an extended object or cluster of sources. The PA can be determined within 5° when a simple day - night offset correction for ionospheric Faraday rotation is applied.

3. The frequency of calibrations employed for channel gain calibration is adequate for polarization since the instrumental parameters affecting polarization performance are typically more stable than channel gain.

4. Accuracy sufficient to meet astronomical objectives is achieved by applying orthogonality calibration to the array. Calibration of the array polarization is not required if the antenna polarization is predominantly circular (i.e. less than 10% unwanted hand present).

5. Implementing complete polarization correction for the array is undesirable unless the polarization of the reference antenna is known or can be calibrated. The present scheme of allowing the polarization error for all baselines to contribute makes optimum use of the calibration information available.

Chapter 4

Antenna Measurements

The calibration and data correction techniques described in the previous chapter were based on the assumption that the antennas exhibited polarization that is very nearly circular. Special laboratory measurement techniques were developed specifically to perform high accuracy polarization measurements on the feed antennas at DRAO prior to their installation on the reflectors in order to assure that the prescribed condition of circular polarization was met. A description of the technique together with test results to establish confidence in the implemented measurement system are presented and the utility of this method for polarization measurements, especially under the conditions met at DRAO, is clearly demonstrated.

The technique described is a novel application of an established antenna measurement method, the phase-amplitude method. This method has been extended to permit the use of probe antennas whose polarizations are both arbitrary and unknown.

The laboratory measurements provide absolute polarization of feed antennas and their patterns as opposed to the relative polarization obtained from observations of the sky as obtained with the current instrument. Consistency between measurements obtained from the laboratory and from sky observations is demonstrated.

4.1 Antenna Measurement Programme at DRAO

The feed antennas were individually removed from their respective reflectors, refurbished and adjusted from mid December of 1990 to mid March 1991 as part of a major facility upgrade. The addition of polarimetry was included as part of this upgrade and the adjustment of antennas for polarization measurement was required. Moreover, as there is no programme of regular removal of feed antennas for service, this upgrade provided a unique opportunity to perform individual pattern measurements, including polarization, on many of the feeds. Difficulties, unique to this situation, faced in this endeavour are as follows.

1. The integrated feed and focus box assemblies are rather large, about 1 m^3 in size and 100 kg mass, making measurements in conventional antenna laboratories impossible. Off-site antenna laboratories capable of handling these

large assemblies were inaccessible at the time of this upgrade. Moreover the logistics of scheduling feed removal, a major undertaking, and coordination with a third party made off-site measurements impractical.

2. The antenna measurements were performed outdoors during the winter so the time available for each antenna was short, about six hours, during which the antennas were installed in the test range, measured and then removed in preparation for reinstallation on the reflector. These time constraints, complications due to winter weather and difficulty in repeating measurements once an antenna was reinstalled, made a simple, quick and reliable setup and measurement procedure mandatory.

3. Good polarization performance was demanded of the test range. Striving for 1% sensitivity levels of corresponding instrumental polarization requires the test range to reliably record polarization ratios of magnitude $\pm$ 40 dB.

An outdoor antenna test range was constructed from readily available materials. The feed antenna polarization was then obtained by the *phase-amplitude method* described in section ??. Three antennas were added to the array before the antenna laboratory measurements were considered leaving the original four, antennas 1, 2, 4 and 7, available for antenna tests. By establishing the performance of these four antennas by antenna range measurements it was hoped that similar adjustment procedures applied to the other three would yield similar results. Moreover the polarization of these antennas can be obtained from sky measurements relative to the other four.

A drawing of the feed antenna and quarter wave plate appear in figure (4.1). The quarter wave plate and probe matching were adjusted for a compromise between low return loss, inter-probe coupling and rotational symmetry of the electric field within the waveguide as sampled by a movable test probe. The waveguide was then installed on the focus box and the feed attached to it. The antenna range measurements will include the total effect of the waveguide, quarter wave plate, feed aperture and coupling to the focus box. Insufficient time was available to allow optimization of the feed adjustment by repeating the adjustment-measurement cycle. Therefore any feed exhibiting a polarization ratio of $\pm$ 20 dB (corresponding to an unwanted component of 10 %) or better over the frequency range of interest was deemed acceptable.

The polarization of the feed is determined primarily by the quarter wave plate so that the polarization ratio on boresight as a function of frequency was the primary quantity of interest. Gain, phase and polarization patterns (i.e. as a function of antenna co-ordinates) were obtained in the interest of future research on instrument performance.

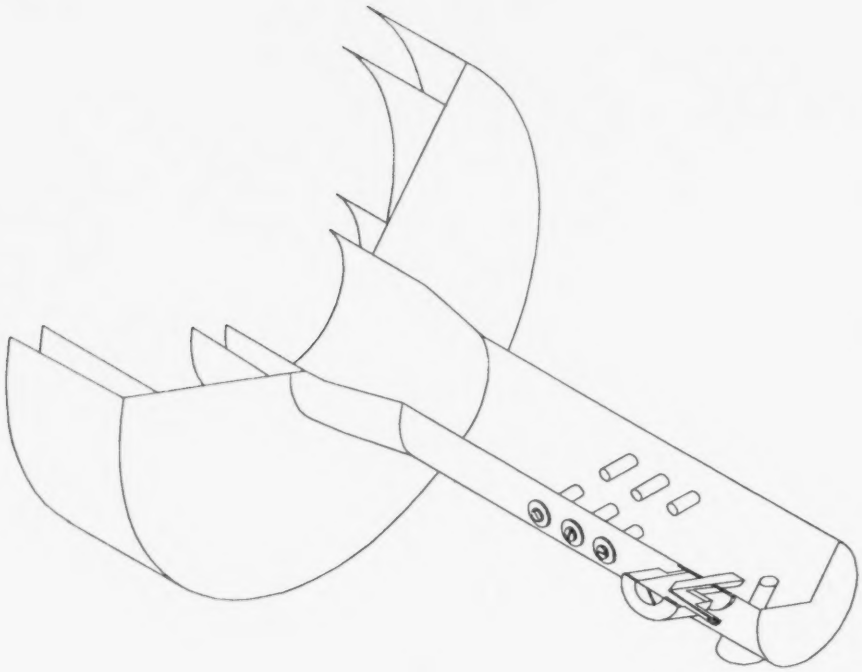

Figure 4.1: A cross section diagram of the feed antenna. The waveguide section which includes the $\lambda/4$ plate and output probes is also shown.

4.2 Antenna Measurements Using the Phase-amplitude Method

Use of the phase-amplitude method for measuring the far field polarization of an antenna is well established (this technique and others are documented in IEEE (1979)) but in the past has not been heavily exploited because of the difficulties in performing phase measurements at the frequencies of interest. Modern computer controlled vector network analysers lay this problem to rest and allow this method to be used routinely in general antenna radiation as well as polarimetric measurements. As part of an antenna pattern measurement system this technique provides the ability to generate both co-polarized and cross polarized gain and phase patterns. Of the various schemes for measuring antenna properties, particularly in regard to obtaining polarization information, the phase-amplitude technique is the only one that provides a total description of the antenna's radiated field including field strength (magnitude and phase), axial ratio and tilt of the polarization ellipse and sense of rotation of any circular component that may be present. Since complete vector information is collected on the unknown field generated by an AUT (*Antenna Under Test*) this system offers additional advantages, overlooked in the literature

and includes the following:

1. The potential exists for off-line correction of data corrupted by noise and spurious range reflections by collecting sufficient data (over a wide range of frequencies and with perturbation to the range layout) and applying techniques such as time domain gating, averaging and modelling with a priori information. The sophistication of the corrections would depend on the software available for analysis of the data after collection.

2. The polarization of the radiated field results from contributions of components other than the principal radiating structures of the antenna such as, in this case, the quarter-wave plate and waveguide defects. With the application of a priori information, the contributions of these components may be separated.

The phase-amplitude method, as described in IEEE (1979), measures the radiated field of the AUT by two probe antennas of nearly orthogonal and known polarization. Software is generally required to convert the voltage measured at these probes to the desired quantities (field strength , phase and polarization). Effects due to lack of probe orthogonality are accounted for either in this software after the data has been collected or with polarization correction networks following the probes. The problem of determining polarization with probes of arbitrary but known polarization has been treated in the literature (see Lee, Okubo, Ling (1988)). If the probe antenna polarizations are unknown than an independent method such as the three antenna method described in IEEE (1979) is invoked to determine their characteristics before the phase-amplitude measurement can be applied. An alternative technique, developed during the course of this research and presented in section 4.2.3, allows for unknown probe polarization and calibrates the probes with a procedure performed easily as part of the measurement set-up.

The phase-amplitude measurement addresses the problems faced by the measurement described in section 4.1 by dividing the measurement programme into two distinct phases. The data collection phase, when resources are at a premium, is a simple operation in which a series of mechanically executed steps provides all information required to characterize the AUT and the range. This is followed by the somewhat more involved task of data interpretation which can be performed when convenient and when computing and manpower resources are available. Considerable flexibility is afforded as all radiation characteristics of the antenna can then be generated as required and in the desired format. Moreover, fidelity and sensitivity may be enhanced with further data processing.

The description of polarization will be in terms of the circular polarization ratio, q as introduced in section 2.2.3 which is a complex quantity formed by the ratio of the LHCP over the RHCP field component (and from which tilt and axial ratio are readily obtained). Since the antennas to be tested were all circularly polarized, the use of the circular polarization ratio is natural since the cross-polarized and co-polarized fields are related to this quantity by simple division. This facilitates the presentation of the field in terms of these two orthogonal components. Much

of the notation used in this thesis follows Mott (1986) and the reader is referred to this reference for more detail on representing waves in this manner.

4.2.1 Theory of the method

Consider an AUT located at the origin of the rectangular coordinate system depicted in figure (4.2). A distant pair of probe antennas receive what is effectively a plane wave travelling in the $+z$ direction. The wave can be described in terms of its total field strength, E_o and orthogonal circular components normalised according to the scheme introduced by equations (2.56) and (2.57) of section 2.2.3. Thus

$$\mathbf{E}_o = E_o \left(l_o \hat{\mathbf{u}}_L + r_o e^{-j\gamma} \hat{\mathbf{u}}_R \right) e^{-jkz} \tag{4.1}$$

where $|l|^2 + |r|^2 = \frac{1}{2}$ and γ is the phase difference between the LHCP and RHCP components.

The polarization of an antenna will be defined by the polarization ratio of the wave that it transmits in the $+z$ direction so that the desired quantity is the conjugate polarization ratio of the wave incident on the probe antennas. The observable is the ratio of the two probe antenna voltages. The voltage at the output of the $i'th$ probe antenna while receiving wave $\mathbf{E}_o$ is given by

$$V_i = \mathbf{E}_o \cdot \left[G_i \left(l_i^* \hat{\mathbf{u}}_L + r_i^* e^{-j\gamma_i} \hat{\mathbf{u}}_R \right) \right] \tag{4.2}$$

where G_i is the gain factor which includes the probe effective height, cable loss and gain of the apparatus used to measure the voltage. The subscript i designates quantities associated with probe antenna i. Substituting (4.1) into (4.2) and expressing the result in terms of polarization ratios yields

$$V_i = 2E_o e^{-jkz} G_i l_o l_i^* \left(1 + \frac{1}{q_o q_i^*} \right) \qquad |q_o q_i^*| \neq 0 \tag{4.3}$$

$$V_i = 2E_o e^{-jkz} G_i r_o r_i^* \left(1 + q_o q_i^* \right) \qquad |q_o q_i^*|^{-1} \neq 0 \tag{4.4}$$

The polarization ratio of the incoming wave may be obtained by taking the ratio of the two probe voltage as described by (4.3) and (4.4) and solving for q_o. Thus

$$q_o = \frac{r_2^* - \Gamma r_1^*}{-l_2^* + \Gamma l_1^*} \tag{4.5}$$

where

$$\Gamma = \frac{V_2}{V_1} \frac{G_1}{G_2} \tag{4.6}$$

The *antenna voltage gain*, G_A, of the AUT is found by measuring its radiated field intensity, E_o, relative to that generated by a "*standard*" (antenna of known gain), $E_s e^{-jkz}$. Solving equations (4.3) and (4.4) respectively for the antenna voltage gain yields

$$G_{A_L} = \frac{E_o}{E_s} l_o = \frac{V_i}{2G_i l_i^* \left(1 + \frac{1}{q_o q_i^*}\right)} \qquad |q_o q_i^*| \neq 0 \tag{4.7}$$

for the LHCP component and,

$$G_{A_R} = \frac{E_o}{E_s} r_o = \frac{V_i}{2G_i r_p^* (1 + q_o q_i^*)} \qquad |q_o q_i^*|^{-1} \neq 0 \tag{4.8}$$

for the RHCP component. Recalling that $|l|^2 + |r|^2 = \frac{1}{2}$, the voltage gain of the total field is given by

$$|G_A| = \frac{E_T}{E_s} = \sqrt{2\,|E_o|^2 \left(|l_o|^2 + |r_o|^2\right)} \tag{4.9}$$

Hence, the antenna gain is measured by selecting one of the probes and recording the output voltage, as opposed to the polarization ratio, which requires the voltage ratio of two probes.

4.2.2 Channel gain calibration

Probe polarization ratios and gain are either known or determined from calibration procedures. If the probe polarizations are known, only the channel gain ratio is required to complete the measurement, and the calibration procedures become straightforward. The probe is illuminated with a field of known polarization ratio, q_{cal}, such as that generated by a standard antenna and the probe output voltage ratio is recorded. Equation (4.5) is solved for Γ with $q_o = q_{cal}$ and equation (4.6) is then solved for the gain ratio.

A linearly polarized antenna is chosen as a calibration standard primarily because it is possible in practice to develop such an antenna possessing a very high degree of polarization purity. It is accepted by the measurement community at large that, if exceptional care is taken in fabrication, a linearly polarized antenna may be used as a standard for most applications without proof of its polarization. A discussion of standard antennas may be found in IEEE (1979).

A linearly polarized antenna positioned with $\tau = 45^\circ$ provides a convenient calibration standard especially if the probes are aligned along the *x-axis* and *y-axis* of figure (4.2). This provides an electric field with components that are equal in magnitude and parallel with each probe. The polarization ratio of this linear calibration standard is $q_{cal} = -j$; the component magnitudes are $|L_s| = |R_s| = \frac{1}{2}$.

Antenna gain calibration involves the measurement of individual channels as opposed to the channel gain ratio. Substituting the linear antenna characteristics into equations (4.3) and (4.4) and solving for the unknown gain products yields, respectively,

$$G_i l_i^* = \frac{V_i}{\left(1 + \frac{j}{q_i^*}\right)} \tag{4.10}$$

and

$$G_i r_i^* = \frac{V_i}{(q_i^* + j)} \tag{4.11}$$

Hence, providing that the probe polarization is known, the calibration for polarization measurement and gain only requires illumination of the probes with a linearly polarized field of known position angle, which in the case exemplified above, is 45°. The antenna gain as provided by equations (4.7) and (4.8) will be relative to the gain of the standard antenna.

4.2.3 Calibration of probes of unknown polarization

The method about to be described is applicable to situations where the probe polarization is unknown and leads to a practical calibration procedure in which two probe antennas of arbitrary but differing polarizations can be used for polarization measurements. For practical reasons associated with computation of the probe components, the polarization of the probes should not be very close to identical. Similarly, for reliable voltage measurements it is best that probes with a high degree of circular polarization be used for the measurement of predominantly linear fields and vice versa. Consider a plane wave incident on the probes as before but generated by a linear calibration standard antenna of high polarization purity in place of the AUT. Expressing (4.1) in terms of linear components yields

$$\mathbf{E} = E_o e^{-jkz} \left(a_x \hat{\mathbf{u}}_x + a_y e^{j\delta} \hat{\mathbf{u}}_y \right)$$

where $a_x^2 + a_y^2 = 1$, a_x and a_y are real. The linear components may expressed in terms of the circular ones by

$$a_x = |l_o| + |r_o| \, e^{j\gamma} \tag{4.12}$$

$$a_y e^{j\delta} = j \, |l_o| - j \, |r_o| \, e^{j\gamma} \tag{4.13}$$

The circular components are, in general, complex quantities while the linear components are real. Hence the polarization state of a wave is represented by a unique set of linear components whereas, in the case of circular components, the polarization ratio is unique and the phase of the components, l_o and r_o simply contributes to the phase constant of the wave. The polarization and amplitude (for gain measurements) of the polarization components are of interest and since absolute phase of the wave received by the probes is not meaningful in this context, the phase of l_o and r_o is unimportant.

The voltage output from the two probes and the above linear polarization components of the calibration field can be related by the polarization distortion matrix (PDM) introduced by Barnes (1986). Thus

$$\begin{bmatrix} V_1 \\ V_2 \end{bmatrix} = E_o e^{-jkz} \begin{bmatrix} P_{11} & P_{12} \\ P_{21} & P_{22} \end{bmatrix} \begin{bmatrix} a_x \\ a_y e^{j\delta} \end{bmatrix} \tag{4.14}$$

Substituting equations (4.12) and (4.13) into (4.14) and dividing both sides by $|r_o| e^{j\gamma}$ yields

$$\frac{1}{|r_o e^{j\gamma}|} \begin{bmatrix} V_1 \\ V_2 \end{bmatrix} = E_o e^{-jkz} \begin{bmatrix} P_{11} + jP_{12} & P_{11} - jP_{12} \\ P_{21} + jP_{22} & P_{21} - jP_{22} \end{bmatrix} \begin{bmatrix} q_o \\ 1 \end{bmatrix} \tag{4.15}$$

where the elements of the PDM now refer to circular components.

Substituting the voltage ratio formed from (4.15) into (4.6) and then solving the result for q_o yields

$$q_o = \frac{-P_{21} + jP_{22} + \Gamma \frac{G_2}{G_1} (P_{11} - jP_{12})}{P_{21} + jP_{22} - \Gamma \frac{G_2}{G_1} (P_{11} + jP_{12})} = \frac{r_2^* - \Gamma r_1^*}{-l_2^* + \Gamma l_1^*} \tag{4.16}$$

from which the probe polarization ratios are derived (by inspection). Thus

$$q_1 = \frac{l_1}{r_1} = \frac{-P_{11} + jP_{12}}{-P_{11} - jP_{12}} \tag{4.17}$$

$$q_2 = \frac{l_2}{r_2} = \frac{-P_{21} + jP_{22}}{-P_{21} - jP_{22}} \tag{4.18}$$

In order to solve for the elements of the PDM, consider voltage vectors X, Y, and F measured for three different illuminating fields, each linear but with ellipse tilts in the coordinate system of figure (4.2) of 0°, 45° and 90° respectively. Then, by substituting the appropriate linear components into equation (4.14),

$$X = \begin{bmatrix} V_2 \\ V_1 \end{bmatrix}_{\tau=0°} = E_o e^{-jkz} \begin{bmatrix} P_{11} \\ P_{21} \end{bmatrix}$$

$$Y = \begin{bmatrix} V_1 \\ V_2 \end{bmatrix}_{\tau=90°} = E_o e^{-jkz} \begin{bmatrix} P_{12} \\ P_{22} \end{bmatrix}$$

$$F = \begin{bmatrix} V_2 \\ V_1 \end{bmatrix}_{\tau=45°} = \frac{E_o e^{-jkz}}{\sqrt{2}} \begin{bmatrix} P_{11} + P_{12} \\ P_{21} + P_{22} \end{bmatrix}$$

Arbitrarily setting $P_{11} = 1$ will allow a solution for the other three elements relative to P_{11} but will not affect the polarization ratios as determined by equations (4.17) and (4.18). The remaining elements of the PDM can then be expressed in terms of the voltage ratios corresponding to the three illuminating fields. Thus,

$$P_{21} = \frac{X_2}{X_1} \tag{4.19}$$

$$P_{22} = \left(\frac{\frac{F_2}{F_1} - \frac{X_2}{X_1}}{1 - \frac{Y_1}{Y_2} \frac{F_2}{F_1}} \right) \tag{4.20}$$

$$P_{12} = \frac{Y_1}{Y_2} P_{22} \tag{4.21}$$

This PDM solution can be applied to equations (4.17) and (4.18) to determine the probe polarization ratios.

4.2.4 Implementation of the phase-amplitude measurement range

The set-up is shown in figure (4.2) and is a basic outdoor, far field antenna range design as outlined in IEEE (1979). The AUT is mounted on a computer controlled turn-table that rotates in azimuth (θ). The turn-table is mounted on a track riding carrier that provides for motion along the z-axis , a useful tool in the removal of spurious range responses (see chapter 8 of Rudge, Milne, Olver and Knight (1986)). The AUT was driven by an RF source internal to the Hewlett-Packard HP8753 vector network analyser. The fields radiated by the AUT were received by the two probes whose outputs are fed to the receiver inputs of the network analyser through 12 metre lengths of coaxial cable. Care was taken to ensure that the cables were cut to the same length and were installed in a like manner to minimize differences in phase due to temperature and other environmental changes. The output of the analyser and receivers are phase-locked to a common reference. The power levels of the reference and received signals were maintained according to the manufacturer's recommendations for maximum phase measurement accuracy. Measurement speed was compromised somewhat in the interests of accuracy.

The probe antennas consisted of a solidly constructed, multi-mode circular horn fed by a 0.7λ circular waveguide. Power was coupled out of the waveguide by two physically orthogonal, linear probes which exhibit a high degree of polarization purity. The probes are nevertheless treated as having unknown polarization in the calibration phase. Calibration consists of replacing the AUT by a linear calibration standard of high polarization purity mounted in a fashion that allows accurate positioning for tilt angles 0°, 45° and 90°. A low taper pyramidal horn fed by a length of rectangular waveguide was used as the standard. It is expected, according to various literature sources such as Mott (1986), that a well constructed horn of this type will provide cross-polarization levels of less than -40 dB. The probe was illuminated and calibration data collected for each of the three tilt angles over the range of frequencies used in the antenna measurement. This operation was performed during convenient times of the measurement session.

The physical layout of the range as shown in figure (4.4) consists of two towers approximately 12 meters apart and 6 metres high. One tower held a platform containing the turn-table and the other supported the probe antenna. A metal trailer was used to house the electronic equipment and ran along side of, but at an acute angle to the range, the closest point being approximately 3.5 metres from the probe tower. Absorbing mats were distributed sparingly along the ground between the two towers during measurements in an attempt to reduce ground reflections. Figure (4.4) and (4.5) contain photographs of the antenna range and the feed antennas as discussed in the next section. The +20 dbm output of the network analyser provides ample signal to noise ratio and the sweep averaging feature of the analyser and narrow IF bandwidths were employed. The measurement of polarization is little affected by wind induced tower movement (estimated up to a wavelength at times during the measurement session) owing primarily to the fact that the ratio between the probe signals is measured.

The software is made up of three separate modules. A data collection programme

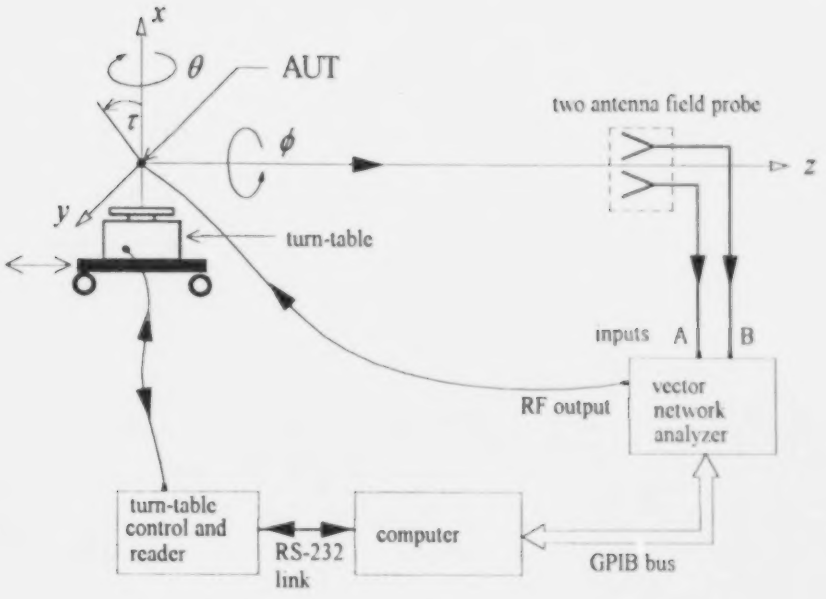

Figure 4.2: A schematic representation of the measuring system. The antenna range co-ordinates are shown above the turn-table and the AUT is placed at the origin of this system. The spherical co-ordinates, θ and ϕ refer to the antenna radiation pattern.

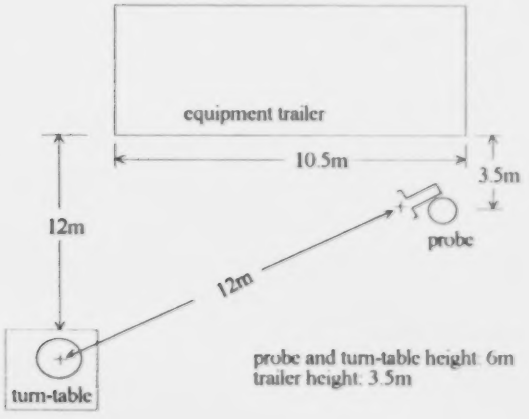

Figure 4.3: A plan view of the antenna range.

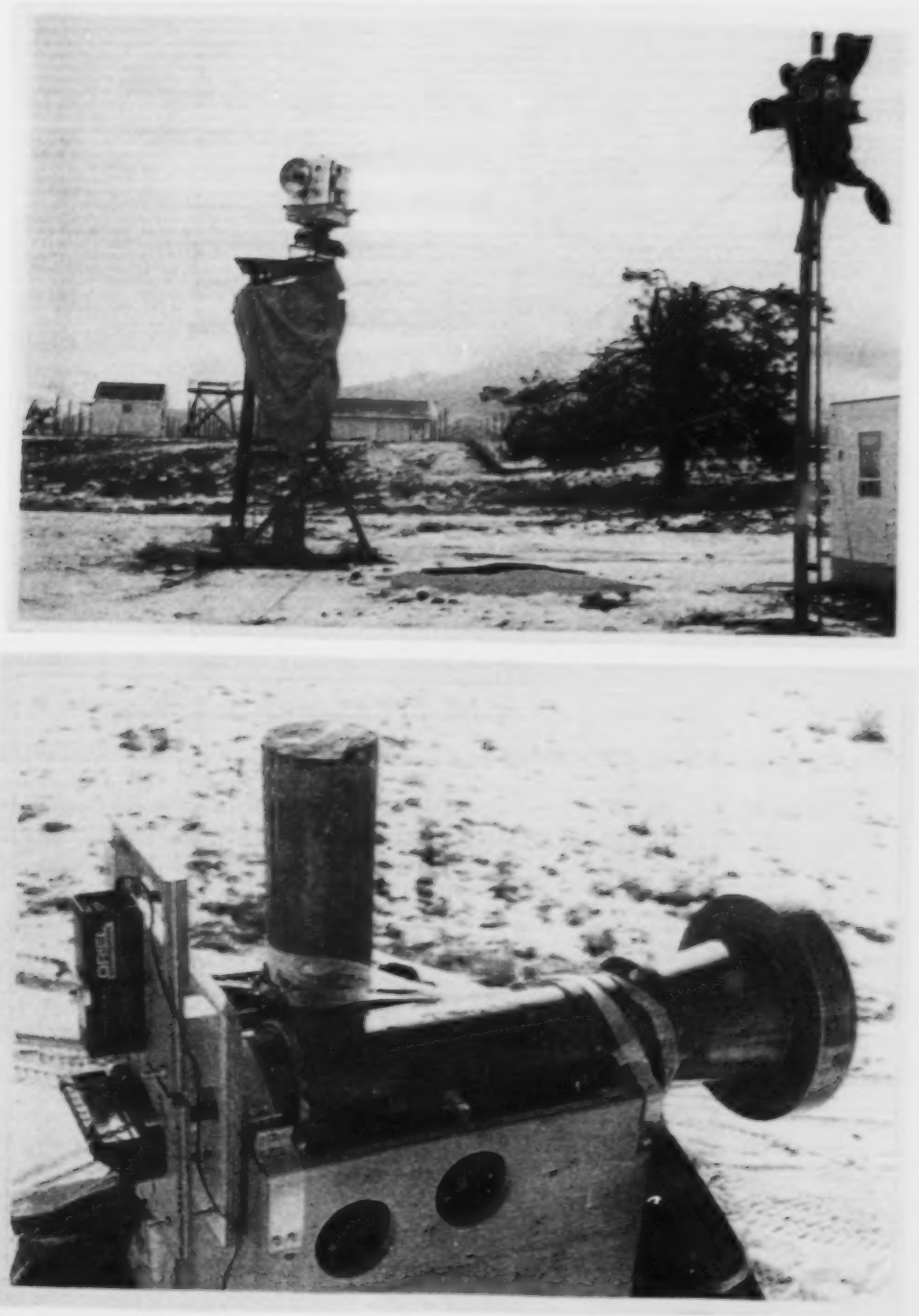

Figure 4.4: Photo of the antenna range (top) and the probe (bottom).

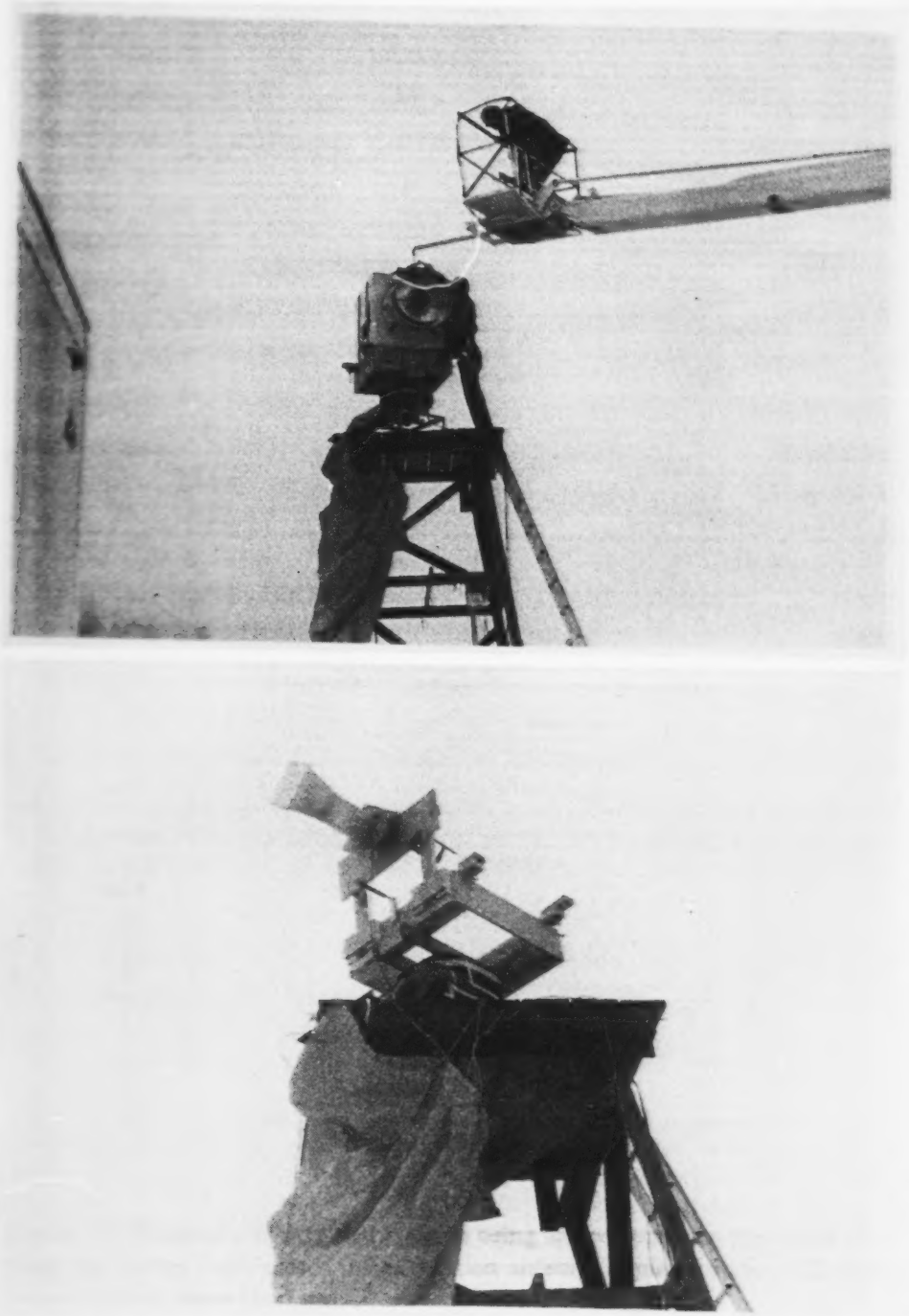

Figure 4.5: Photo of a DRAO feed antenna being lowered onto the turn-table of the range for testing (top) and of the calibration antenna in place of the AUT during the calibration phase (bottom).

orchestrates the set up for calibration and pattern measurement, sets up and collects data from the network analyser over a GPIB instrument bus, controls and reads the antenna turn-table position. Data are collected in the form of complex voltage for the two network analyser channels for each frequency and turn-table position in the ranges specified. If probe polarization is not assumed a second module generates probe polarization ratios from the raw calibration data collected by the previous module. A third programme accepts the raw data and probe polarization ratios and provides the co-polarized (either LHCP and RHCP) field magnitude, phase and the polarization ratio. These quantities are provided as a function of either frequency or antenna position. Various commercial or public domain programmes can be invoked after this stage to clean up the measurements and convert them to the desired form such as pattern plots.

4.3 Measurement Results

This section presents the results of the feed measurement programme undertaken during the winter of 1990 / 1991. The feed measurements attain the objective of providing the polarization properties of the waveguide and quarter wave plate as a function of frequency and, in addition, provide antenna radiation patterns of gain, phase and polarization. The results of the former are compared with antenna polarization as determined from calibration data of the telescope. A test was also conducted to verify the operation of the probe calibration procedure developed for this measurement programme and described in section 4.2.3. The test results appear in section 4.3.3.

4.3.1 Feed measurements

The LHCP port of the AUT was excited and the cross-polarized gain of feed antenna #7 (in this case RHCP) relative to the co-polarized gain on boresight plotted as a function of azimuth angle θ in figure (4.6). The polarization designation refers to that of the feed and must be exchanged when referring to the polarization of an array antenna to account for the reversal of polarization sense upon reflection. Both principal plane cuts (designated by $\phi = 0°$ and $\phi = 90°$) are shown. Symmetry in the pattern of the aperture radiated field is compromised by the cross-polarization contribution of the quarter wave plate and spurious range reflections although the effects of the latter were reduced considerably by averaging the measurements over two AUT-probe separations. A slight correction, increasing as the antenna was rotated from the boresight position, was applied to the azimuth angle to account for the fact that the feed aperture and phase centre were far removed from the mechanical axis of rotation.

Figures (4.7) to (4.10) are plots of magnitude and phase of the circular polarization ratio on boresight as a function of frequency. A 3.3° beam squint was observed and accounted for when rotating the antenna from $\phi = 0°$ to $\phi = 90°$ so that boresight refers to the electrical or beam centre. These plots represent the contribution of the quarter wave plate and waveguide components to the overall polarization

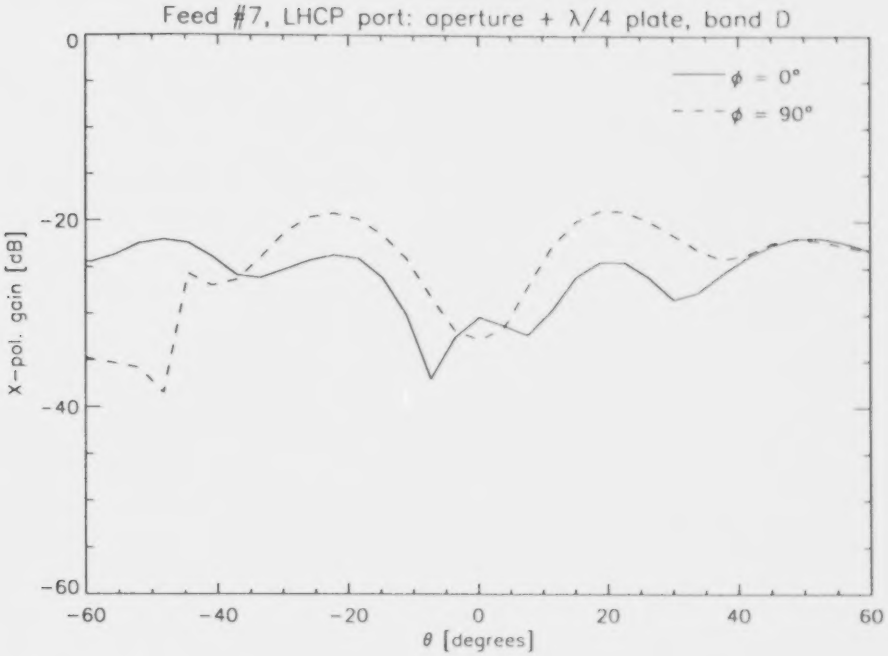

Figure 4.6: The cross-polarisation gain (normalised to the peak value of the co-polarisation gain) as a function of azimuth angle, θ for feed #7. This plot contains contributions to the polarization by both the feed aperture and waveguide components.

since these will dominate on boresight for a physically symmetrical antenna. The variation of the magnitude between the two pattern cuts bears witness to the presence of spurious range reflections. The magnitude of the polarization ratio should remain constant with the rotation from $\phi = 0^\circ$ to $\phi = 90^\circ$and phase should change by exactly 180 degrees (twice the tilt angle of the polarization ellipse). This fact was employed to subtract the contribution of the quarter wave plate from the total field plot of figure (4.6) and yield the pattern of the radiating aperture alone. Letting the subscripts 0 and 90 designate the $\phi = 0^\circ$ and $\phi = 90^\circ$ pattern cuts respectively, the radiation pattern due to the aperture alone (the contribution of the quarter wave plate is subtracted) is a_L and a_R for the left and right channel respectively and is calculated by

$$a_{R_0}(\theta) = q_{R_0} - \left(\frac{q_{R_0} - q_{R_{90}}}{2}\right) \tag{4.22}$$

$$a_{R_{90}}(\theta) = q_{R_{90}} + \left(\frac{q_{R_0} - q_{R_{90}}}{2}\right) \tag{4.23}$$

$$a_{L_0} = \frac{q_{L_0}\,(q_{L_{90}} - q_{L_0})}{q_{L_0} + q_{L_{90}}} \tag{4.24}$$

$$a_{L_{90}} = \frac{q_{L90}\,(q_{L_0} - q_{L_{90}})}{q_{L_0} + q_{L_{90}}} \tag{4.25}$$

where q_L and q_R are the left and right boresight polarization ratios as depicted in figures (4.7) to (4.10). The quarter wave plate contribution subtracted in equations (4.22) to (4.25) is the average of those in the $\phi = 0^\circ$ and $\phi = 90^\circ$ positions. The results are presented in figure(4.11). The pattern shows good symmetry about boresight for both cuts. The discontinuity around $\theta = -45^\circ$ for the $\phi = 90^\circ$ pattern cut is due to an intermittent connection to the AUT during measurement and is present in a number of the plots.

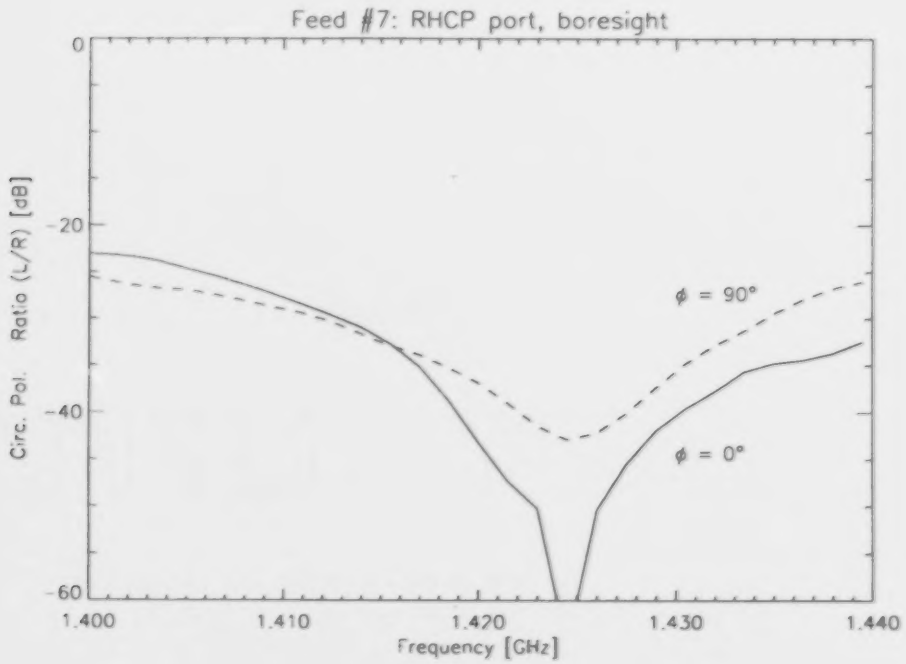

Figure 4.7: The amplitude of the circular polarization ratio on boresight (electrical) as a function of frequency for the RHCP port.

A theoretical pattern was calculated with available software (see Bridges, Shafai, Kishk (1990)) which employs the method of moments to solve for the scattered and reflected fields of a rotationally symmetric object composed of a combination of dielectrics and conductors. This calculated pattern is superimposed on figure (4.12) and is in satisfactory agreement with the measurements. Features present in the

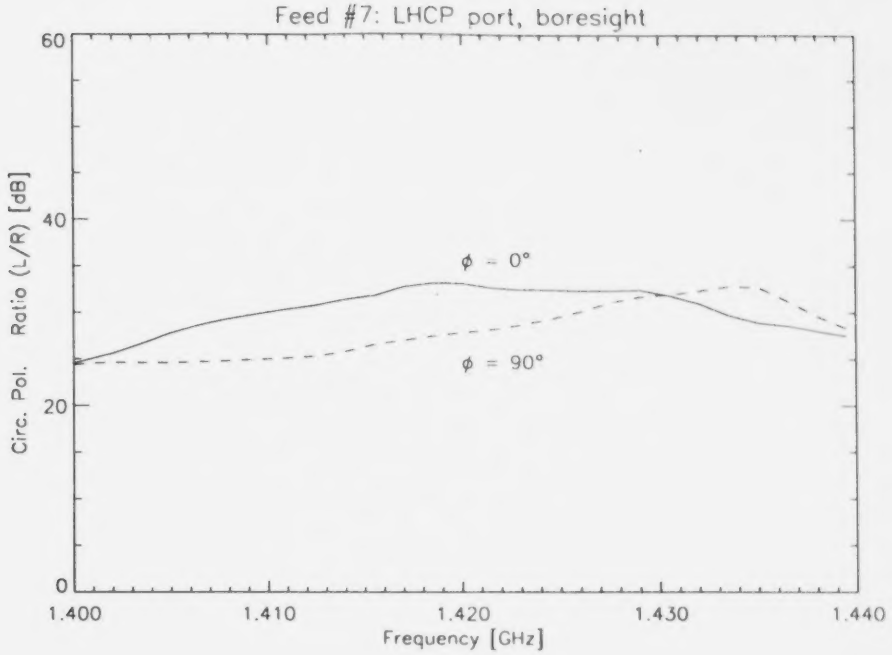

Figure 4.8: The amplitude of the circular polarization ratio on boresight (electrical) as a function of frequency for the LHCP port.

measured fields but not in the theoretical prediction may be due to interaction of the feed with structural members such as the focus box or of range equipment such as the turn-table and tower. A discussion of antenna range errors is presented in section(4.3.2).

Figure (4.13) is a normalized plot of the co-polarized gain of the AUT (measured and calculated) and is included for completeness. Rotational symmetry of the pattern, a mandatory requirement for low cross-polarization contribution of the reflector, is implied.

The feed antenna should possess a well defined phase centre, a point about which rotation through azimuth angle, θ , results in a constant phase, if the prime focus reflector antenna is to perform as expected according to geometric optics. A constant phase is a special case of symmetry so that the interests of low cross polarization are served with this requirement. Measurements were made to verify the existence of a distinct phase centre and locate its position. Phase plots of the feed antenna are complicated by the fact that, for practical reasons, the mechanical axis of rotation for the focus box assembly is far removed from the electrical phase centre. Attempts at determining phase from raw phase data taken at 1.444 GHz yielded the plot of figure (4.14). A phase centre which is displaced radially (along the z-axis) by D and

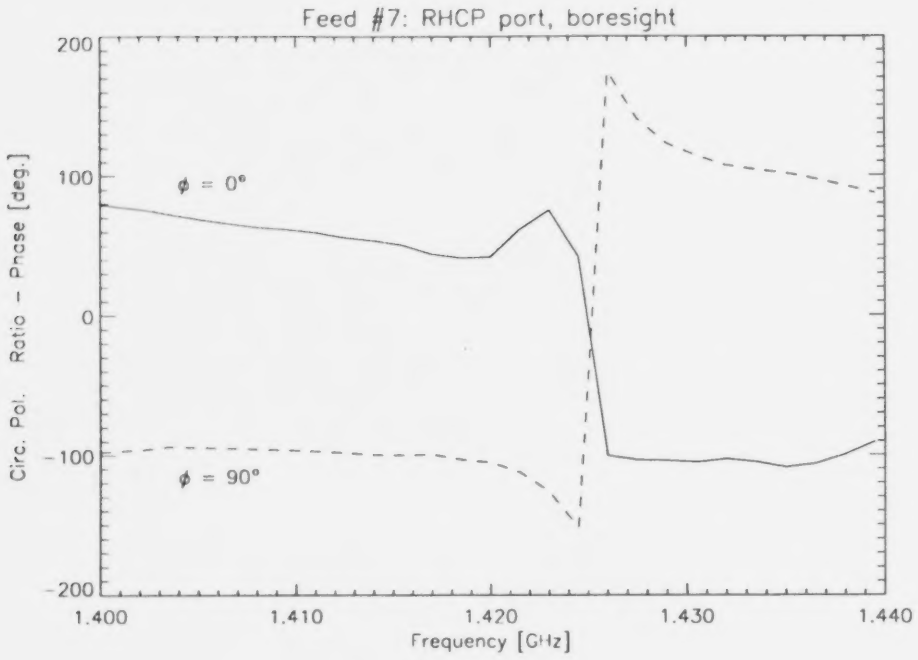

Figure 4.9: The phase of the circular polarization ratio on boresight (electrical) as a function of frequency for the LHCP port.

laterally (perpendicular to the z-axis) by d from the mechanical axis of rotation will exhibit a phase according to Rudge, Milne, Olver and Knight determined by

$$\psi' = \frac{\lambda}{2\pi}\left(k^2 + D^2\right)\left[1 - \cos\left(\theta + \arctan\left(\frac{D}{d}\right)\right)\right] \tag{4.26}$$

A fit of equation (4.26) to the data of figure (4.14) yields a value of $D = 78.5$ cm and $d = 0.2$ cm. The residual phase resulting from this fit is shown in figure (4.15) and it is apparent that a distinct phase centre does exist over the illumination angle required by the reflector.

4.3.2 Antenna range errors

Errors in the measurement of antenna gain and polarization exist in any practical antenna range due to interaction of the radiated field of the AUT with the environment in which radiation reflected from nearby objects interferes with the direct radiation from the AUT to the probe. If some fraction of this reflected radiation undergoes a change from the principal polarization to the opposite hand it will affect the measurement of polarization. Possible paths within the geometry of this

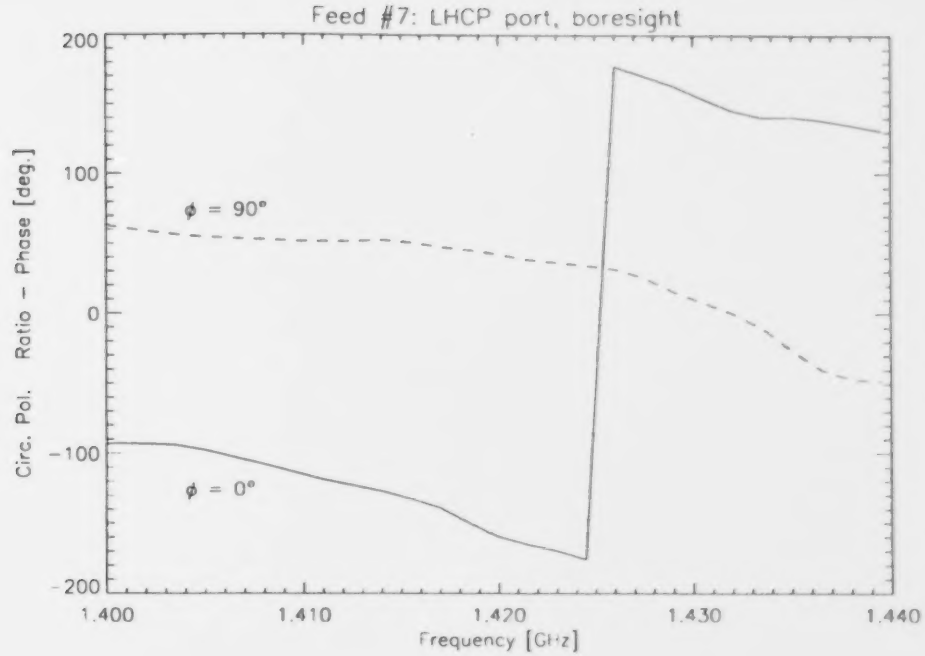

Figure 4.10: The phase of the circular polarization ratio on boresight (electrical) as a function of frequency for the RHCP port.

particular range include specular reflection from the ground between the probe and AUT, from the support structures for the AUT and from the metallic equipment trailer. Efforts to diagnose specific mechanisms of such reflections by covering up possible reflectors led to inconclusive results indicating, perhaps, that the errors contain contributions from a combination of the above. However, it was determined that significant reflection did occur from the ground and that this was reduced by at least a factor of two (in power of the interfering signal) by placing absorbing mats on the ground midway between the towers. Errors could be further reduced (by a factor of two) by averaging the data that was recorded with the AUT separated from the probe by two different distances approximately $\frac{1}{2}\lambda$ apart. Unfortunately time constraints allowed this extra data to be collected for antenna 7 only.

Polarization measurement errors due to spurious range reflections are identified by variations in the magnitude of the polarization ratio as the antenna is rotated from $\phi = 0°$ to $\phi = 90°$. This should, ideally, be constant on boresight but since the cross-polarized or unwanted hand component from the AUT and the interfering ray (derived from the co-polarized ray of the AUT) undergo a 90° phase shift in opposite directions, a significant change in the composite signal is expected. The worst case differences between the two curves in both figures (4.7) and (4.8) yield

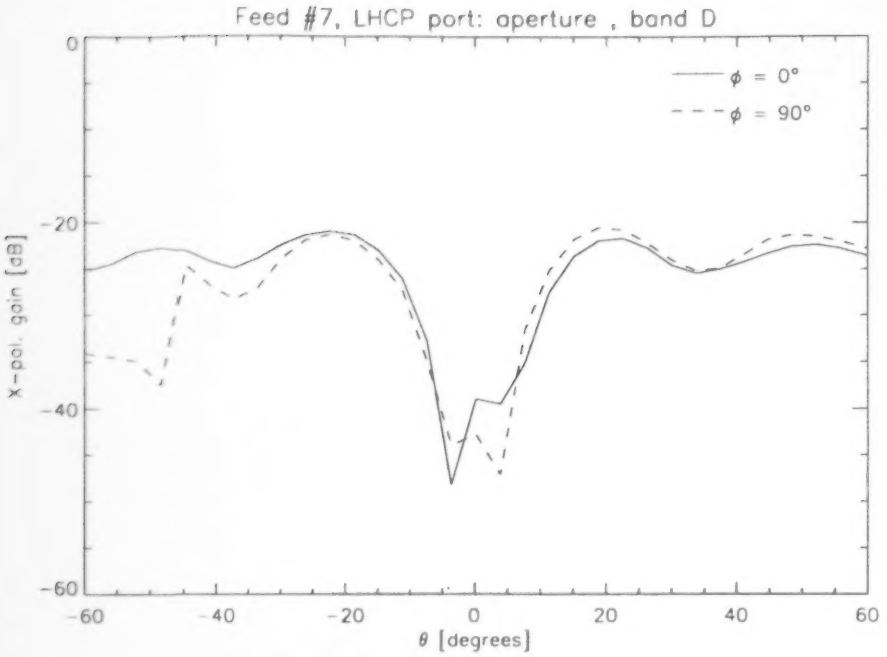

Figure 4.11: The cross-polarization pattern of the aperture made from vectorially subtracting the boresight cross-polarization from the total pattern.

an estimate for the level of spurious reflections interfering with the cross-polarized component of the direct ray. Since the polarization ratio in figure (4.7) represents the level of unwanted hand power in the principal channel (the reciprocal in the case of figure (4.8)) error in this measurement is the *polarized range clutter*. Taking samples from figures (4.7) and (4.8) and applying them to

$$\%clutter = \frac{100}{2}\left|10^{-\left|\frac{\sigma_{max}}{20}\right|} - 10^{-\left|\frac{\sigma_{min}}{20}\right|}\right| \tag{4.27}$$

where σ is the magnitude circular polarization ratio, in dB, which is the worst case difference between the $\phi = 0°$ and $\phi = 90°$ curves, yields error levels under $\pm 1.5\%$. There is no guarantee that the data in this plot were subject to the worst case interference so that the range clutter could be somewhat higher than this. Moreover it is observed to be higher, possibly due to the single track position measurements, in some of the other antenna measurements. For purposes of the remaining discussion, the range clutter is set at 2% or -34 dB. That is to say that the polarization ratio, or the level of unwanted hand component present in a given channel, as determined by the antenna lab measurements will have an uncertainty of 2% associated with it. The worst case error in phase depends on the level of the unwanted hand component

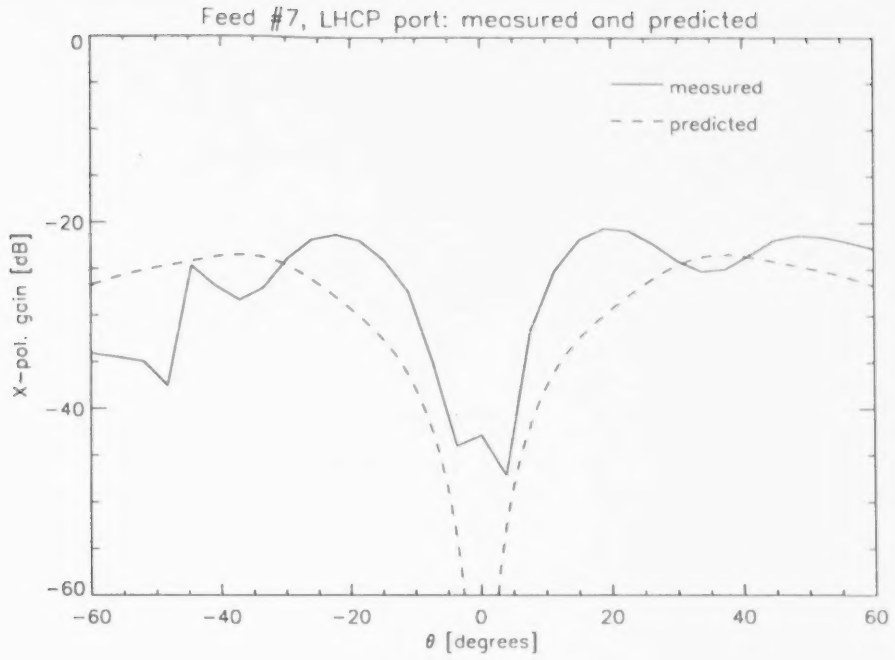

Figure 4.12: A plot of the cross-polarization gain for $\phi = 0°$ (aperture contribution) superimposed on a corresponding calculated pattern.

present in the signal radiated by the AUT and can be crudely estimated by

$$\Delta\theta = \sin^{-1}\left(\frac{\%clutter}{\%unwanted}\right) \tag{4.28}$$

An in-depth discussion of estimating antenna range errors may be found in chapter 8 of Rudge et al. (1986).

4.3.3 Probe calibration test

The probe antennas exhibited high linear polarization purity in their original state and were very much orthogonal to one another. In order to test the calibration techniques discussed above the probe polarization purity and orthogonality were spoiled by inserting a metallic obstruction in the aperture. The probe was calibrated in the normal way and a measurement of an unknown antenna performed. The obstruction was then removed and the measurement taken a second time. As seen in figure (4.16) there is up to 20 dB difference between the circular polarization ratio as measured with the normal probe and spoiled probe (for the same calibration set). Corresponding phases are shown in figure (4.17). The probe was then re-calibrated

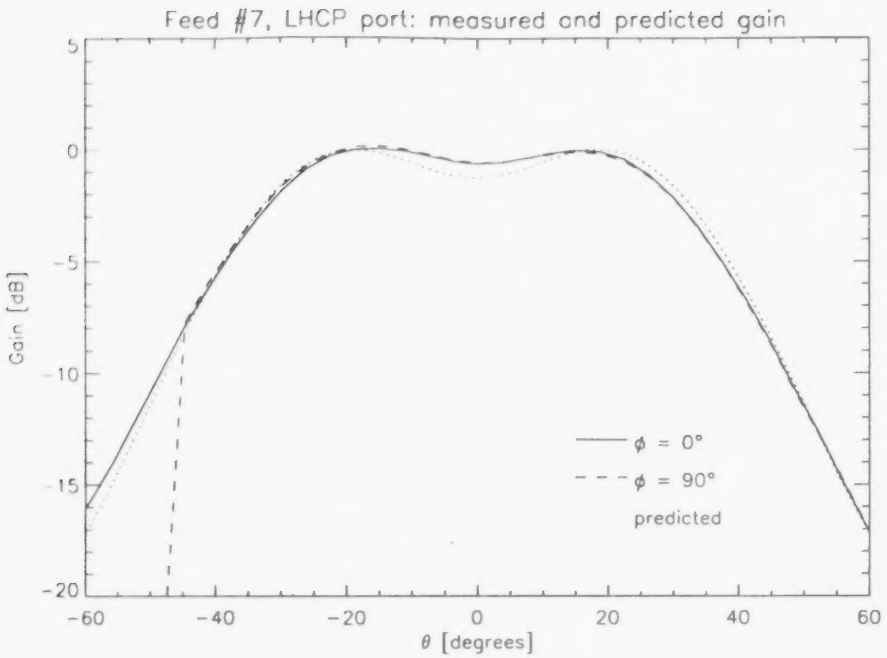

Figure 4.13: The co-polarization gain normalised to its peak value as a function of azimuth angle θ. A calculated pattern is superimposed for comparison.

in its normal state and the measurements taken for a third time. It can be clearly seen from figures (4.16) and (4.17) that the two properly calibrated cases compare well with each other. The discrepancy at the low frequency end is likely due to range reflections (implied by the deep null at about 1407 MHz).

4.3.4 Comparison with telescope observations

Antenna polarization properties as determined from telescope observations of celestial objects are represented by the cross-polarization calibration coefficients stored in the MCDB as discussed in section 3.2.2. These calibration coefficients are a product of the cross-polar reference gain (section 3.2.1) and polarization ratio *relative to a selected reference antenna* to a good approximation providing that the antenna polarization is near circular ($|q_L| > 10$ or $|q_R| < 0.1$).

The antenna polarization obtained from these coefficients is compared to the antenna range measurements by first setting the coefficients of the reference antenna to the reference polarization.The reference polarization is that which is measured for the reference antenna in the antenna range. Comparison may then take place between laboratory and sky based measurements for the other three. Figure (4.18)

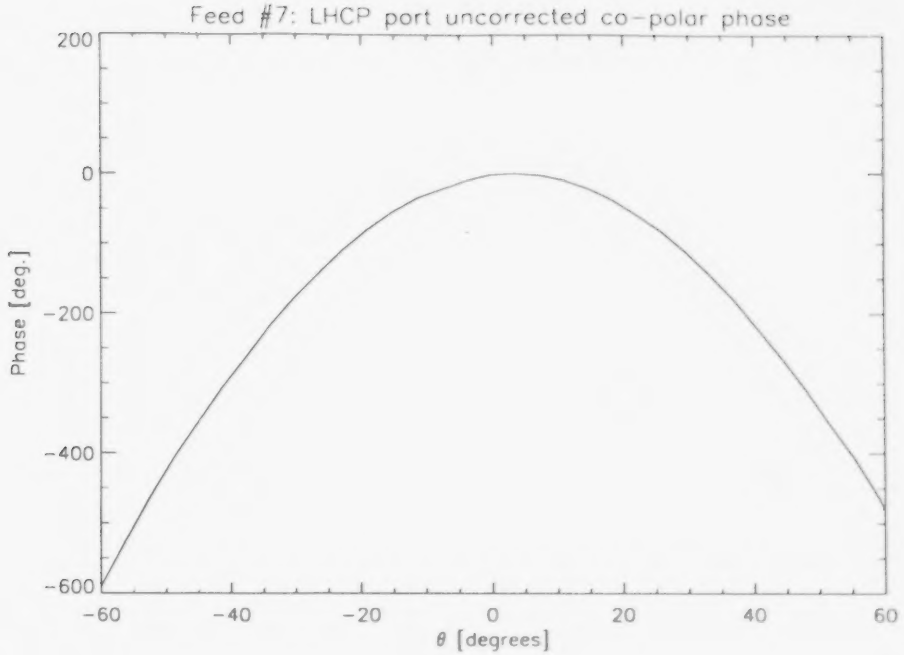

Figure 4.14: The phase as measured for the feed antenna. The large excursion is due to the difference between the mechanical axis of rotation and the antenna phase centre.

depicts the feed antenna in the relative orientation of $\phi = 0^{\circ}$ and $\phi = 90^{\circ}$ for the antenna laboratory measurements and the reference coordinate system (figure(2.2)) for the ST. The $\phi = 0^{\circ}$ represents the position where, ideally, a zero degree phase difference between voltage measured at the two oppositely polarized ports results when illuminated with a linearly polarized wave of position angle zero degrees (or, in the case of ellipse tilt, $\tau = 0^{\circ}$). Using this range reference for comparison, the ST coefficients will have an approximately 180° phase difference between the two ports under the same conditions. This is evident in the cross-polar reference phase (see figure (3.19)). This phase difference will not contain the rotation due the ionospheric Faraday rotation, although the phase of the CPRG in figure (3.19) does. Hence it would be unwise to apply a correction to the data based on the CPRG as determined by observations of 3C286. However differences in phase between channels of the electronic systems following the antenna are included in the calibration coefficients stored in the MCDB and represent an unknown factor. An assumption is made that good engineering practices prevail and that the phase constant added to both left and right channels be equal. A CPRG phase of 180° is assumed.

The coefficients are prepared for comparison by

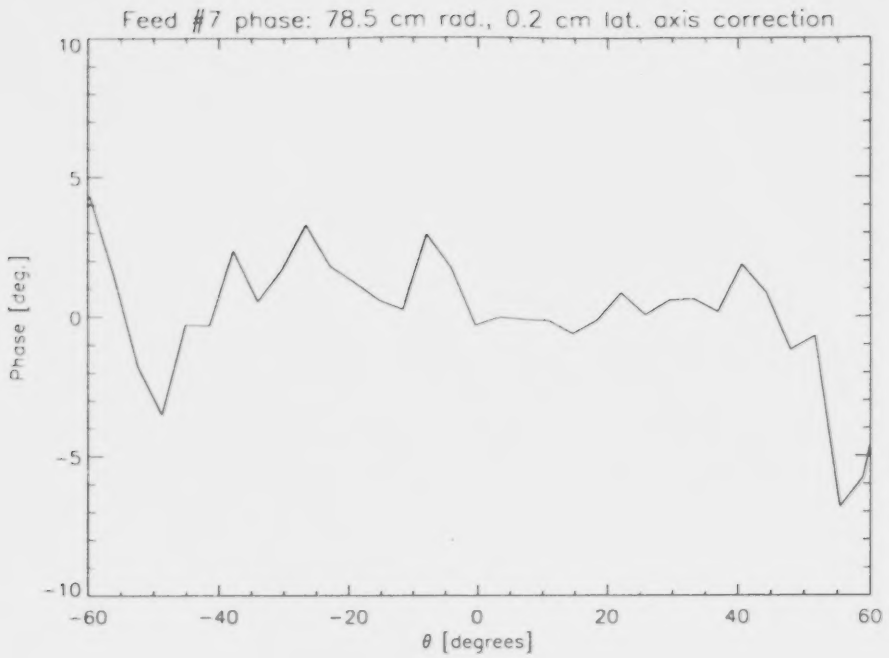

Figure 4.15: The residual phase variation after correcting the phase pattern data for the offset of the rotation axis.

1. re-referencing (assuming a zero value for) the cross-polar coefficients of the MCDB for the reference antenna selected for comparison,

2. multiplying the coefficients by the conjugate of the cross-polar gain, assumed to be 180°, to effectively rotate the feed into the $\phi = 0^\circ$ position of the antenna lab co-ordinate system,

3. changing the polarization description for waves propagating in the $-z$ direction (figure (2.2b)) to the $+z$ direction (the antenna range co-ordinates of figure (4.2)) and

4. vectorially adding the polarization of the RHCP channel of the reference antenna as obtained from antenna range measurements to all antennas of the array.

Applying the above steps to equations (3.40) and (3.41) of section 3.2.2 yields

$$l_R = G_{xref} x_{lr}^* + x_{ref}^* \simeq q_R \tag{4.29}$$

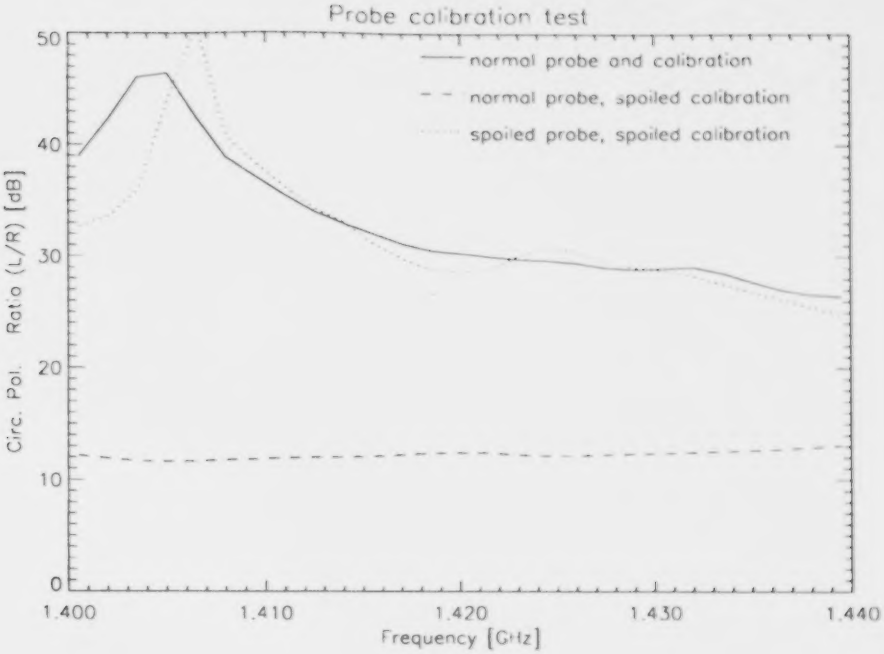

Figure 4.16: The circular polarization ratioof an antenna taken with the setup under two vastly different conditions. The correct calibration was applied to the corresponding data for two of these and mismatched in the third to test the probe calibration method.

$$r_L = G''_{xref} x^*_{rl} - x_{ref} \simeq \frac{1}{q_L} \tag{4.30}$$

$$x_{ref} = \frac{1}{q_{L_{ref}}} \tag{4.31}$$

where the polarization components, l_R and r_L, now refer to waves propagating in the $+z$ direction of the antenna range co-ordinate system of figure (4.2). The change of polarization due to the presence of the reflector is accounted for by the use of the LHCP channel polarization ratio in equation (4.31). Antenna #7 is selected as the reference antenna as more thorough polarization measurements performed on this antenna result in a greater degree of confidence. The earliest suitable calibrations available from the MCDB involved source 3c147. Twelve calibrations during the period from September 12 to September 25 1992 were selected and averaged together for the sky measurement sample. To make comparison of the polarization more palatable the modified coefficients of (4.29) and (4.30) are multiplied by 100 to yield (approximately) the percent contamination of the opposite polarization to the

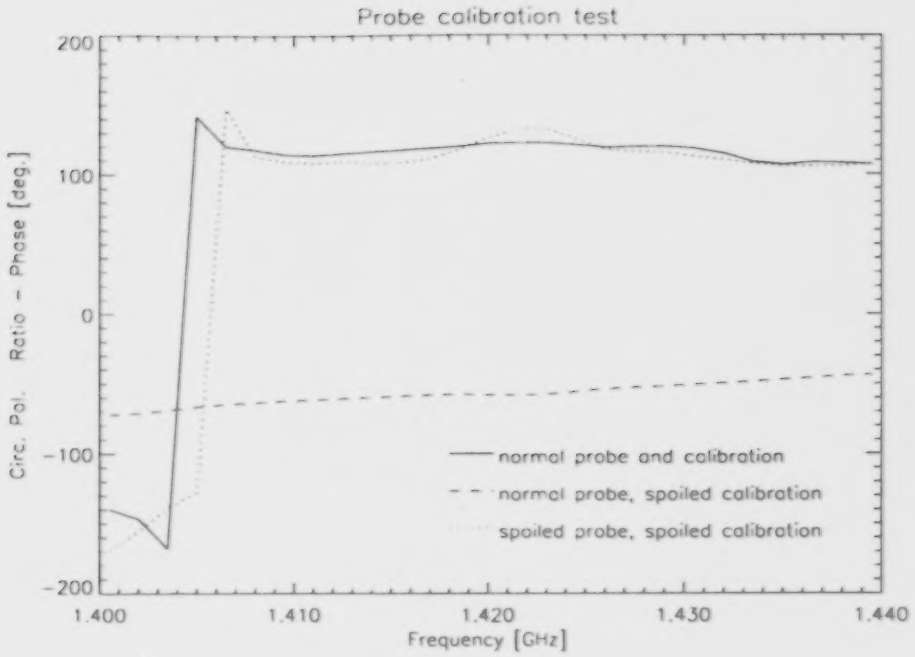

Figure 4.17: The accompanying phase plot for the probe calibration test.

principal one. Uncertainties associated with the antenna laboratory measurements are ±1.5% for antenna #7 and ±2.0% for the others as discussed in section 4.3.2. A small additional uncertainty of ±1.0% is adopted for the sky measurements to account for effects due to the presence of the reflector, focus box support struts and mismatch due to the electronic systems connected to the antenna ports. The sky measurements are referenced (for this comparison) to antenna #7 and , therefore, inherit any error associated with #7. A worst case uncertainty in any comparison between antenna laboratory and sky based measurements could be as high as the sum of the above which exceeds ±4%. Comparing these two measurements would seem to be of little value, even if error prediction is pessimistic, given that the expected level of cross-polarization in most of the antennas is expected to be very small (a few percent).

The results are tabulated in table (4.2) and are within the uncertainties predicted. The phase error according to equation (4.28) could be as high as ±45° and it was not considered useful to include them. The orthogonality between two channels of a given antenna is calculated from equation (3.38) and shown in table (4.1). Physically the values in table (4.1) are the percentage of total intensity present in the RL and LR correlations of a given antenna (if this were provided) when observing an unpolarized calibrator.

Band	Antenna polarization orthogonality (%)							
	Antenna	**1**	**2**	**3**	**4**	**5**	**6**	**7**
A	**Sky**	0.9	3.0	1.2	4.3	3.1	2.8	1.2
	Lab	0.7	2.5	-	3.8	-	-	0.8
	Antenna	**1**	**2**	**3**	**4**	**5**	**6**	**7**
B	**Sky**	2.0	2.4	2.3	1.6	2.8	0.1	1.4
	Lab	1.0	2.7	-	3.8	-	-	1.2
	Antenna	**1**	**2**	**3**	**4**	**5**	**6**	**7**
C	**Sky**	1.0	4.7	1.2	3.6	1.0	2.7	0.9
	Lab	3.8	1.5	-	3.5	-	-	2.5
	Antenna	**1**	**2**	**3**	**4**	**5**	**6**	**7**
D	**Sky**	2.0	2.4	2.3	1.6	2.8	0.1	1.4
	Lab	1.0	1.6	-	3.7	-	-	2.6

Table 4.1: Polarization orthogonality per antenna in percent. Values based on both telescope calibration with sky data and antenna range measurements are presented.

Ant. #	Pol.	Band A		Band B		Band C		Band D	
		Sky	Lab	Sky	Lab	Sky	Lab	Sky	Lab
1	L	3.2	2.3	4.3	1.0	3.5	0.8	4.9	2.4
1	R	2.5	2.8	2.9	1.6	2.6	3.0	2.9	1.8
2	L	4.3	5.1	4.5	3.9	6.2	1.6	4.9	0.3
2	R	4.4	5.4	4.1	5.2	2.3	1.9	2.8	1.3
3	L	9.2	-	8.2	-	6.4	-	5.3	-
3	R	8.9	-	7.1	-	6.8	-	5.1	-
4	L	9	7	8.5	6	6.3	4.3	6.6	2.6
4	R	9.5	7.5	7.6	6.8	3.0	3.9	5.2	2.8
5	L	4	-	1.3	-	3.4	-	2.7	-
5	R	3.4	-	3.6	-	2.9	-	4.6	-
6	L	14	-	13	-	12	-	9.2	-
6	R	14	-	13	-	13	-	9.1	-
7	L	5.1	5.1	4.4	3.7	3.7	0.4	4.3	1.9
7	R	4.9	4.9	3.2	3.7	2.9	2.9	2.9	2.9

Table 4.2: Percent contamination of the opposite to principal polarization associated with the feed antennas for both sky and laboratory based measurements.

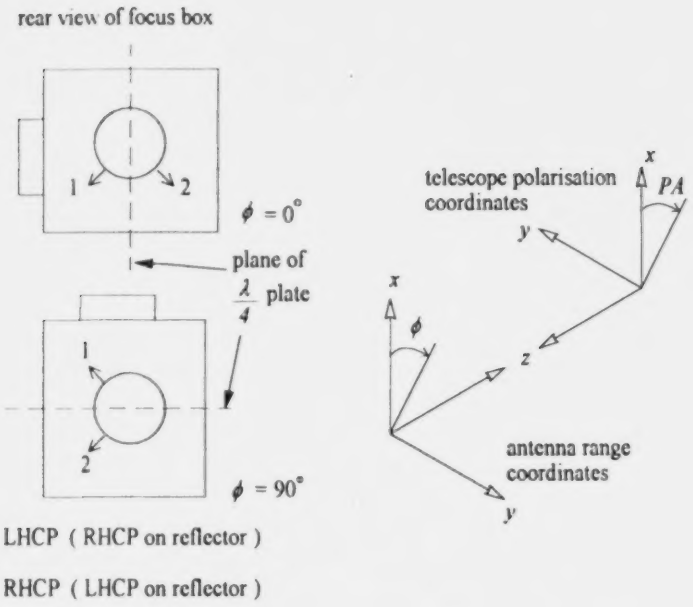

Figure 4.18: The focus box position in terms of the antenna range co-ordinate, ϕ, (left) and the relation between antenna range co-ordinates and the ST co-ordinates (right).

4.3.5 Conclusions

Conclusions reached during the course of the antenna measurements follow.

1. The simple outdoor antenna range described in this chapter is inadequate for high accuracy performance evaluation of the feed antennas due to uncertainties created by spurious range reflections relative to the low level of cross-polarization associated with a properly adjusted feed. Nevertheless, it can establish that the feed antennas were adjusted to a performance level adequate for use in a polarimeter that is calibrated by methods described in chapter 3.

2. The phase-amplitude method is a useful tool in the measurement of antenna radiation characteristics in general. This method requires a data collection procedure that is only slightly more involved than that associated with an accurate gain pattern measurement, yet provides the maximum amount of information on antenna radiation characteristics attainable with far field measurements. This additional information allows complete polarization determination and provides considerable flexibility in the reduction, correction and interpretation of data.

3. The calibration scheme developed here works as expected and is a viable way to implement the phase-amplitude method without the need for probe antennas of known polarization. The spoiled probe experiments of section 4.3.3 demonstrate that the use of probes with arbitrary polarization for antenna measurements, notably polarization measurements, is possible.

4. The feed antennas work as expected and exhibit cross-polarization levels that allow polarimetry with this telescope.

Chapter 5

DA530 : A Test Observation

A complete survey was made of DA530, a supernova remnant of known polarization properties, to test the new polarization facility of the DRAO synthesis telescope. The resulting maps are consistent with those, previously published, of instruments with lower resolution and are in excellent agreement with recent high resolution images of the VLA (unpublished). This comparison also demonstrates the utility of higher resolution offered by the DRAO ST over single antenna polarimeters (low resolution) and the benefits derived from the wide field of view offered by this instrument over those with higher resolution but smaller fields (the VLA for example).

A usable field width of at least 1.5° is demonstrated by an observation of DA530 that is offset from the field centre of the telescope.

5.1 Introduction

A complete survey was made of an extended source in order to evaluate the instrument's performance as an imaging polarimeter. The objectives of this observation were:

1. to determine whether any significant distortion in the observed polarization is apparent over a field of view typically observed with this instrument and
2. to demonstrate that the maps made are consistent with what is known about the object.

In order to execute the first objective the object was observed, in two independent surveys, with the map phase centre located on the centre of the object and then with the phase centre displaced from the object. The polarization of corresponding features of the object in both fields could then be compared.

DA530 (G93.3+6.9) was selected as the test object. The first high resolution observations ($2'.0 \times 2'.4$) of DA530 were made at 21 cm with the DRAO ST by Roger and Costain (1976). They demonstrated the source to have a highly symmetrical brightness distribution of diameter 27 arcminutes with bright rims on the northwest and southeast section of the object. This morphology combined with an observed

spectral index (α, where $S \propto \nu^{-\alpha}$) of 0.51 identified this source as a supernova remnant. The total integrated intensity of the object was reported to be 6.9 Jy. Polarimetric observations with single antenna telescopes were made at 1720 MHz and 2700 MHz (Haslam, Pauls and Salter (1980)) with resolutions of $7'.6$ and $4'.4$ respectively. These early polarization measurements suggest very high levels of polarization present within the object particularly in the bright rims where the percentage polarization ran as high as 45 to 55 % at 2700 MHz and levels exceeding 40 % at several points within the remnant. Polarimetric observations at 4.7 GHz were made by Lalitha, Mantovani, Salter and Tomasi (1984). Recent (unpublished) polarimetric observations by aperture synthesis with the VLA, in addition to those noted above, are presented in section (5.2.2).

This object was selected as the test case for reasons that follow.

1. The edge of the ST field for reliable total intensity imaging is, at present, advertised to be 75 arcminutes from the field centre (2.5° diameter). DA530 is about 30 arcminutes in size allowing two observations of the object, displaced from each other, to cover a significant portion of the usable field. This coverage is required to investigate the field distortion referred to in the second point above. Moreover, DA530 is representative in size and spatial power distribution of typical objects observed with this telescope and provides a convincing demonstration of the polarization imaging capabilities.

2. DA530 has a previous observation history that present observations could be compared to.

3. The total flux obtained by previous observations of DA530 with the DRAO ST (Roger and Costain (1976)), using a minimum spacing of 17.1 metres, agree well with single antenna measurements indicating that the ST does not seriously underestimate the broad structure of DA530.

4. The polarized flux intensity is high enough to allow for easy discrimination between thermal noise and systematic errors of the type described in chapter 2. The brightness in a 1 arcminute beam was predicted , on the basis of Roger and Costain, to be approximately 25 mJy/beam. A polarized fraction of 6% will be 5 σ (standard deviation) above the anticipated noise in the DRAO maps of $\sigma = 0.3$ mJy/beam. The expected levels of polarization, from Haslam et al. (1980), of 30 % will yield an easily detectable level of polarized emission in the map.

5. Lalitha et al. (1984) report low levels of rotation measure in the southern rim of the source. This is convenient for comparing the position angle as determined from the present observations with those previously published at other frequencies.

5.2 Observations and Analysis

Two full survey observations were made of DA530 with DRAO survey codes HI and HJ representing the source at field centre (RA 20H 52M 24.00S, DEC 55° 21′ 15.0″) and offset by 30′ southeast of the field centre (RA 20H 49M 39.00S, DEC 55° 40′ 7.0″) respectively. Data were collected for the offset observation from September 11, 1992 to September 28, 1992 and for the centred observation from October 9 to October 22 of the same year.

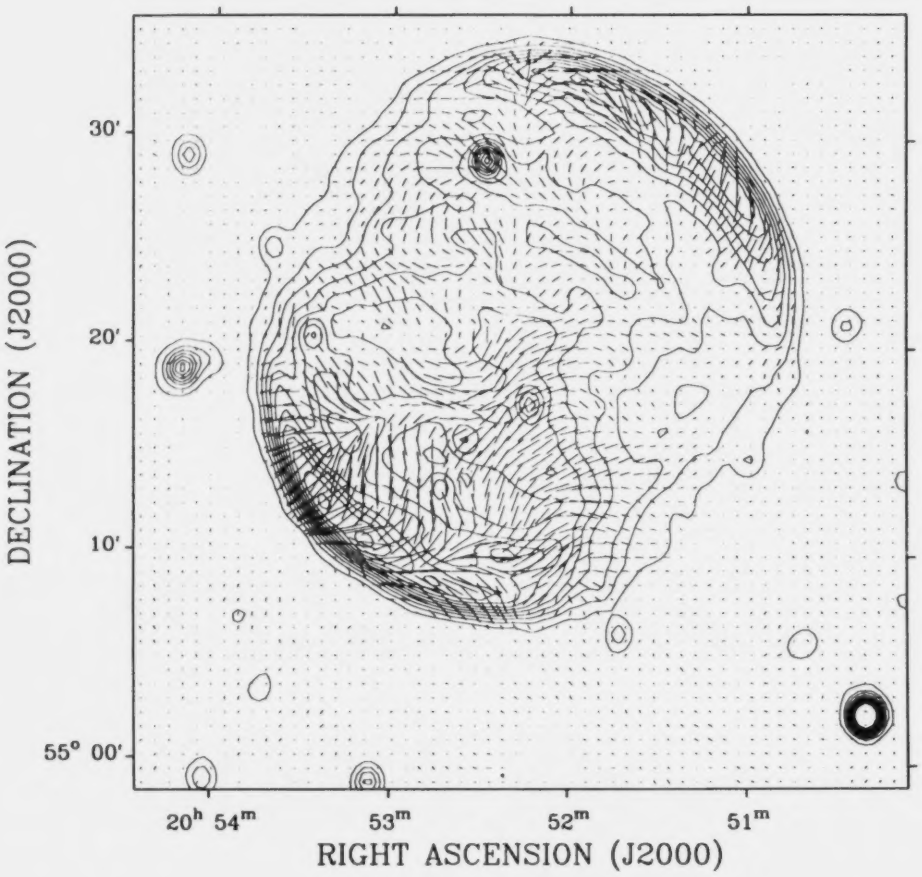

Figure 5.1: DA530 as observed with the new ST polarimeter at DRAO. The contours represent total intensity of levels 2, 6, 10, 14, 18, 22, 26, 30, 34, 38, 42, and 46 mJy/beam. The polarization lines are aligned with the electric field and their length represent polarized intensity amplitude such that 10 arcminutes = 80 mJy/beam.

Unpolarized source 3C147 was used for both pre-observation and post-observation calibration in both observations. Polarized sources 3C286 and 3C138 were employed

for calibration of the cross-polar reference gain (CPRG of section 3.2.3), yielding day and night values respectively. The cross-polar reference phases used in the correction of data were those of the 3C138 (night) calibrations which for bands A, B, C and D respectively were -166°, -159°, -163°and -166°. The sampled u-v plane for the centred survey is weighted by an elliptical Gaussian which is tapered such that the 20 % level represents spatial frequencies corresponding to the largest projected spacings (the largest physical spacing being 617.76 metres). The weighting function is set to zero for spatial frequencies higher than this. The resulting synthesized beam in the image plane is an elliptically shaped, Gaussian that is $1^{'}$ $10^{"}.46$ by $0^{'}$ $58^{"}.20$ wide with major axis positioned -84.7° from the ξ direction of figure (2.5). The synthesized beam for the offset observation is $1^{'}$ $11^{"}.01$ by $0^{'}$ $58^{"}.98$ with major axis at 88.8°. The I, Q and U maps were subjected to the CLEAN algorithm and a correction for the antenna radiation pattern applied.

The resulting map for the offset case is depicted in figure (5.1). The total intensity (I map) is represented as contours while the source polarization, obtained from the Q and U maps, is represented by lines whose amplitude corresponds to the polarized intensity and orientation align with the electric field component of the polarized radiation. The centre of the polarization line corresponds to the point on the image whose polarization is represented.

The background map noise appears unpolarized as do the point sources in the vicinity of DA530. However, several points within DA530 exhibit high degrees of polarization. Samples found by integrating the polarized intensity over (approximately) beam sized patches reveal percentage polarization levels exceeding 60 % on the southeast rim and 50 % for points within the remnant itself (for example RA 20H 53M 7.09S, DEC 55° $13^{'}$ $46^{"}.5$). The background point sources serve as convenient reminders of the approximate size of the synthesized beam.

The polarization lines are observed to be grouped in cells or local regions over which the orientation of the lines are either constant or slowly changing. However, abrupt changes in position angle can occur between adjacent cells. This behaviour is indicative of a highly ordered magnetic field within the remnant and also attests to the absence of severe depolarization within the remnant itself or depolarization due to differential Faraday rotation within the interstellar medium. The latter is not surprising since this object is situated well off the plane of the galaxy and removed from much of the interstellar density and magnetic field variations that would cause differential Faraday rotation along the line of sight. The average scale size of this polarization structure is larger in angular size than the beam implying that the observed polarization across the source is determined by physical properties of the source itself as opposed to the integrated polarization over the beam area. That is to say, that this map approaches (or has reached) the resolution limit for polarization structure within this particular source and that higher resolution would not likely provide proportionately increased information on polarized structure. However, the lower resolution afforded by single antenna polarimeters will miss much of this structure so that this observation alone is a dramatic demonstration of the importance of high resolution (as obtained by synthesis telescopes) polarimetric imaging of extended sources. Examples of maps made with a resolution of $3^{'}$ are shown in figure

(5.8) and discussed further in section 5.2.2.

5.2.1 Comparison of centred and offset observations

These observations were made shortly after the ST returned to service following its upgrade and suffer from instrumental problems not detected at that time. Data collected by the instrument was corrupted by an irreversible truncation error very early in the data processing chain. This error manifested itself as an asymmetric, non-point source of 10 mJy magnitude located in the centre of all the maps. The raw, i.e. not subjected to the CLEAN algorithm, map of the offset observation is shown in figure (5.2). The defect lies within DA530 for the centred observation and results in a severely distorted image. The corruption to the map was not confined to the bogus source but also distributed, at a lower level, over the entire map in the form of asymmetric rings. These rings were of sufficient intensity that the integrated flux over a region in the offset field map containing a large part of one or more of these rings, especially at the levels encountered in the Q and U maps, could be significantly affected. Moreover, the offset maps, for reasons unknown, contained a large number of artefacts in the form of asymmetric rings around point sources in the field. Attempts made to remove these defects, through standard map processing, failed. In summary neither field represents typical ST map quality and each exhibits a high level of background noise. They are, however, useful for the tests required for this instrument. Furthermore the data from one of these observations will be used in scientific analysis. Atomic hydrogen spectral line data collected simultaneously are unaffected by the field centre artefact and provide useful information on the interstellar medium surrounding DA530. A paper describing these results is in preparation.

Many of the severely corrupted data were identified, marked as bad and excluded from any comparison between the two maps in order to attempt analysis of the fidelity of polarization over a large field. The magnitude of the artefacts was observed to be somewhat data dependent but the locations of these points are not significantly affected by the data. Hence points identified as corrupted data in the total intensity maps would also be suspect for the corresponding Q and U maps. The corrupted data were identified by converting the offset maps to ones about the map centre, subtracting the total intensity maps of the two fields and examining the structures that remained. Obvious ring like features well above the expected 0.3 mJy/beam thermal noise floor could be identified along with the central defect. The map that remained after excluding data with magnitude greater than 1.5 mJy/beam appeared to be quite featureless although it exhibited levels in excess of the 0.3 mJy/beam. A list of corrupted points was established and used to mask bad data from further analysis. These points are shown as shaded regions overlaid on a polarized intensity map of DA530 in figure (5.3).

The mean and standard deviation, σ_n, of the background noise were established over regions adjacent to DA530 which are shown as shaded regions D1 to D4 in figure (5.3). The results are tabulated in (5.1). The standard deviation is approximately twice that expected from thermal noise and is likely due to the map problems

	centred observation		offset observation	
Region	Q	U	Q	U
D1	0.41	0.58	0.50	0.54
D2	0.50	0.45	0.52	0.47
D3	0.43	0.41	0.52	0.54
D4	0.50	0.50	0.61	0.62

Table 5.1: The standard deviation in mJy/beam of the background noise for four sample regions.

discussed above.

A set of nine beam-sized test regions and five larger regions was selected over the object in order to execute a polarized flux comparison between the two fields. Areas with large amounts of bad data or areas of particularly weak emission were avoided; otherwise the selection was arbitrary. The two sets of test regions are designated by 'A' and 'B' and are shown as shaded patches in figure (5.3). The total intensity, I, and total polarized intensity, L, (both determined from the centred field) associated with each region are tabulated in table (5.2) along with the percent error calculated from

$$\% \, \Delta L = 100 \left(\frac{L_{centred} - L_{offset}}{L_{centred}} \right) \tag{5.1}$$

where L designates the total linearly polarized intensity and ΔL is the normalized difference in percent. The polarized intensity was calculated by two different methods. One involved calculating the polarized intensity on a pixel by pixel basis and then integrating this quantity over the region R to get L_p (in units of mJy). Thus,

$$L_p = \frac{1}{A_B} \sum_{i=1}^{N_R} \sqrt{U_i^2 + Q_i^2} \tag{5.2}$$

where A_B is the beam area in number of pixels and N_R is the total number of pixels in the region.. Alternatively, the polarized intensity for region R can be determined by integrating the U and Q flux values over the region and then calculating the polarized intensity. The polarized intensity obtained by this method is designated by L_R and found from

$$L_R = \sqrt{\left(\frac{1}{A_B} \sum_{i=1}^{N_R} U_i \right)^2 + \left(\frac{1}{A_B} \sum_{i=1}^{N_R} Q_i \right)^2} \tag{5.3}$$

Calculating the polarized flux obtained by both methods is motivated by the notion that errors apart from the background noise may be present to the Q and U maps, that these errors could be statistical in nature and large enough that a significant bias (see equation (5.7) ahead) to the polarized intensity would be accumulated by the summation of equation (5.2). Equation (5.3) is expected to provide a more reliable result in this case. The position angle difference between

Region	N_R	I (mJy)	L (mJy)	$\sigma_{\Delta L}$ (%)	ΔL_p (%)	ΔL_R (%)	$\Delta\tau^\circ_R$
A1	39	75	44.9	0.8	12.4	2.2	2.2
A2	39	92	48.8	0.8	2.2	2.0	0.9
A3	31	51	23.5	1.4	12.0	-1.1	1.2
A4	34	70	37.8	0.9	5.7	-4.6	0.6
A5	31	84	42.9	0.8	0.0	-3.0	-2.6
A6	35	103	36.1	1.3	6.9	-1.4	0.1
A7	47	112	36.4	1.1	-0.3	-8.5	-2.5
A8	38	117	45.8	0.8	-5.6	2.2	0.4
A9	42	98	41.0	1.0	-1.9	-6.5	1.8
B1	173	363	122.3	0.8	5.6	1.7	1.0
B2	231	440	108.0	0.8	17.1	1.3	1.2
B3	163	305	151.6	0.6	4.1	5.6	1.1
B4	274	693	188.0	0.6	8.5	7.2	0.8
B5	246	660	207.6	0.4	6.1	-0.4	0.8

Table 5.2: A comparison of polarized intensity for selected regions between the centred and offset fields.

centred and offset maps, $\Delta\tau$, is also evaluated by integrating over the regions first. This is analogous to the calculation of L_R and is presented, in units of degrees, in table (5.2). The position angle integrated over beam-sized patches such as those of regions A1 to A9 are of more interest than the larger regions. An alternative approach to evaluating the errors in the polarization vectors is discussed later (see figure (5.6)).

The total polarized flux obtained for a given region containing N_R pixels can only be obtained within confidence limits set by the background noise of the map. The standard deviation associated with the flux of this region, σ_N, in mJy is given by

$$\sigma_N = \frac{\sigma_n\sqrt{N_R}}{A_B}, \tag{5.4}$$

where σ_n is the standard deviation of the map noise per pixel in mJy/beam and A_B is the beam area in pixels. This relationship between σ_N and σ_n is valid for high signal to noise ratios in the polarized intensity map. Given that the noise in the Q and U maps is Gaussian with standard deviation, σ_n, the probability distribution for the polarized intensity is the somewhat complicated Rice distribution. Chapters 6 and 9 of Thompson et al. (1986) provide a discussion of the noise in amplitude and phase of maps expressed in this manner and also demonstrate that these distributions are approximately Gaussian for high signal to noise ratios with standard deviation, σ_p, given by

$$\sigma_p = \sigma_n\left(1 - \frac{\sigma_n^2}{8L^2}\right) \tag{5.5}$$

for the polarized intensity and

$$\sigma_\tau = \frac{\sigma_n}{L} \tag{5.6}$$

for the position angle. Moreover, the polarized intensity distribution is one sided and results in a positive bias to the map. The mean value of any pixel on the map is increased by the quantity, ΔL_n, in mJy/beam according to

$$\Delta L_n = \frac{\sigma_n^2}{2L_n^2} \tag{5.7}$$

where the subscript, n, refers to the pixel values in mJy/beam. Equation (5.7) is valid for high signal to noise ratios. ΔL_n is a few percent when $L_n = 3\sigma_n$ (Thompson et al. (1986), chapter 6).

Typical pixel values encountered on the polarized intensity maps are of order 10 mJy/beam so that $\sigma_p = \sigma_n$ to a very good approximation. The polarized flux, L, of table (5.2) includes the bias of equation (5.7) although, for the cases considered here, it is of no significance.

Table (5.2) includes $\sigma_{\Delta L}$ which is basically σ_N expressed as a percentage of the polarized flux, L, and is given by (see chapter 4 of Bevington (1969))

$$\sigma_{\Delta L}^2 = \Delta L \left(\frac{2\sigma_N^2}{(L_{centred} - L_{offset})^2} + \frac{\sigma_N^2}{L_{centred}^2} \right) \simeq \frac{2\sigma_N^2}{L_{centred}^2} \tag{5.8}$$

where σ_N is given by equation (5.4).

The values used for σ_N in table (5.2) were based on the map noise, σ_n, as listed in table (5.1) and hence take into account the excess noise of these particular maps. It is observed that the difference in polarized intensity between the two maps based on integrated Q and U regions, ΔL_R , is greater in magnitude than $2\sigma_N$ for most of the regions suggesting that errors other than those of the background map noise are present in the regions. Moreover, the discrepancy encountered between the polarized flux values, L_R and L_p, suggest that an error or excess noise (above the background) exists within these regions and that it varies over a pixel sized scale. No obvious correlation between the magnitude of ΔL_R and size of the selected region, total intensity or polarized intensity level is observed in table (5.2). There is no apparent trend in error level from the northwest to southeast rim of the object implying that, at least relative to other errors, polarization distortion due to observation near the field edge is not an issue.

The overall appearance, in the case of vectors, can provide meaningful qualitative information on the polarization structure of the source and yet may be immune to jitter in position angle and amplitude over small scales. Error in position angle on a pixel basis is of particular interest as vector plots, as opposed to the integrated position angle associated with regions, are typically used to view this quantity. The observed position angle between corresponding pixels on the two maps is compared by calculating this quantity on a pixel by pixel basis and presenting the difference as a probability density function in the form of a histogram. Histograms are presented in figure (5.6) and (5.7) for the 'A' and 'B' sample sets respectively. Separate plots

for samples in north and south regions of DA530 are presented. Large differences approaching 360° were due to phase wrapping and, since they comprised a small subset of the total number of points, were simply ignored. The bin size is 2 °. It is observed that over 80 % of the position angle samples agree between fields to within ±7° of some offset position angle. This offset or bias is primarily due to differences in the CPRG calibration between fields.

A visual comparison of the two fields can be made by examining the polarized intensity contours of figure (5.4) and the polarization vector plots of (5.5). The corrupt data map is overlaid on the centred map as before. Polarized features between the two fields compare favourably outside the corrupted data region despite problems with the maps. Visual agreement between the polarization structure of the vector maps is particularly good.

5.2.2 Comparison with other observations

Published observations of the polarization structure of DA530 have been obtained with single antenna telescopes and at wavelengths other than 21 cm making direct comparison with observations of the DRAO ST difficult. The lower resolution of single antenna polarimeters at frequencies near 1420 MHz (the closest being 1720 MHz by Haslam et al. (1980) with a resolution of 7′ as opposed to 1′ with the DRAO ST) results in substantial depolarization due to integration of the source polarization over the instrument's beam area (beam depolarization) and loss of detail in polarization structure. A closer resolution match to the DRAO observations is obtained with the 4.75 GHz observations presented in Lalitha et al. (1984) where the maps have been smoothed to a resolution of 3′. The difficulty in this case is that some of the polarized structure is influenced by Faraday rotation intrinsic to the source and, unless the rotation measure across the source is known to the same resolution level as the ST, the position angles between observations will be difficult to compare with a high degree of accuracy. Nevertheless, consistency of DRAO observations with some aspects of the published data can be demonstrated with little effort. Lalitha et al. (1984) present a map of rotation measure (see figure (5.8)) based on their 4.75 GHz data and the 2.7 GHz data of Haslam et al. (1980). A striking feature is the zero rotation measure observed over most of the southeast quadrant of the remnant. Hence the polarization lines of figure (5.1) are at right angles to the magnetic field and it is clearly seen that the magnetic field is tangential as claimed.

A more comprehensive comparison could be made with published data by smoothing the DRAO ST maps to a lower resolution. However, unpublished observations of DA530 were recently made with the VLA in the D array (resolution of 45" and field of view of 30′) and provide a much better model of the observation. A FAX of the preliminary maps was obtained through private communication with C.J. Salter and a copy is shown in the bottom box of figure (5.9) beneath a comparable map made from DRAO ST observations. The polarization vector map is overlaid on total intensity contours. The DRAO map is of the offset observation of DA530.

Unfortunately, quantitative comparisons could not be made because the data is

only available in the form of FAX plots at the present time. However excellent visual agreement of polarized structure is observed between the VLA and DRAO maps and is a very convincing demonstration that the ST can produce believable polarization maps of extended objects. This comparison also demonstrates one of the strengths of the DRAO ST. The small antennas of the array allow for short element spacings that more completely sample the lower spatial frequencies of the u-v plane than instruments with larger antennas such as the VLA. The difference is seen in figure (5.9) where the total intensity contours at the outer extremities of the remnant are distorted or missing in the VLA map. Sources larger in angular extent than DA530 cannot be accommodated with the VLA because of that instrument's limited field of view (about $30'$) and the danger of missing flux due to undersampling the u-v plane. The DRAO ST, on the other hand, can map sources that are 300% larger or more in angular extent than DA530.

5.3 Conclusions

Conclusions drawn from the observations of DA530 presented in this chapter are as follows.

1. This instrument does indeed function as an imaging polarimeter and, when calibrated by the methods outlined in this thesis, produces results that are consistent with those from established instruments.

2. No significant degradation of the polarization imaging properties was observed between the centred and offset fields of these observations. Hence, it is demonstrated that the instrument can provide satisfactory images of polarized sources out to at least 45 arcminutes from the map centre.

3. The intricate polarization structure observed in DA530 demonstrates the high utility of combining the facility of polarization measurement with the resolution available from aperture synthesis telescopes.

4. Reliable quantitative measurements of polarized flux over some region of a source are obtained by first performing the integration of flux over corresponding regions of the Q and U maps and then calculating the polarized intensity, as opposed to calculating the polarized intensity on a pixel by pixel basis first and then integrating.

5. Pixel noise, likely dependent on the source brightness, may exist on scales smaller than the beam size and this noise can bias the result of polarized intensity, becoming significant when integrated over an area of the map. This chapter has not demonstrated, beyond reasonable doubt, that this noise and the excess background noise of these particular maps are indeed different quantities. Rigorous tests for the existence of this noise could be performed in the future and, for positive results, the cause could be investigated. However, as

reliable quantitative results involve flux integration over areas of the synthesized beam or greater, understanding the mechanisms that generate this noise may be an academic exercise.

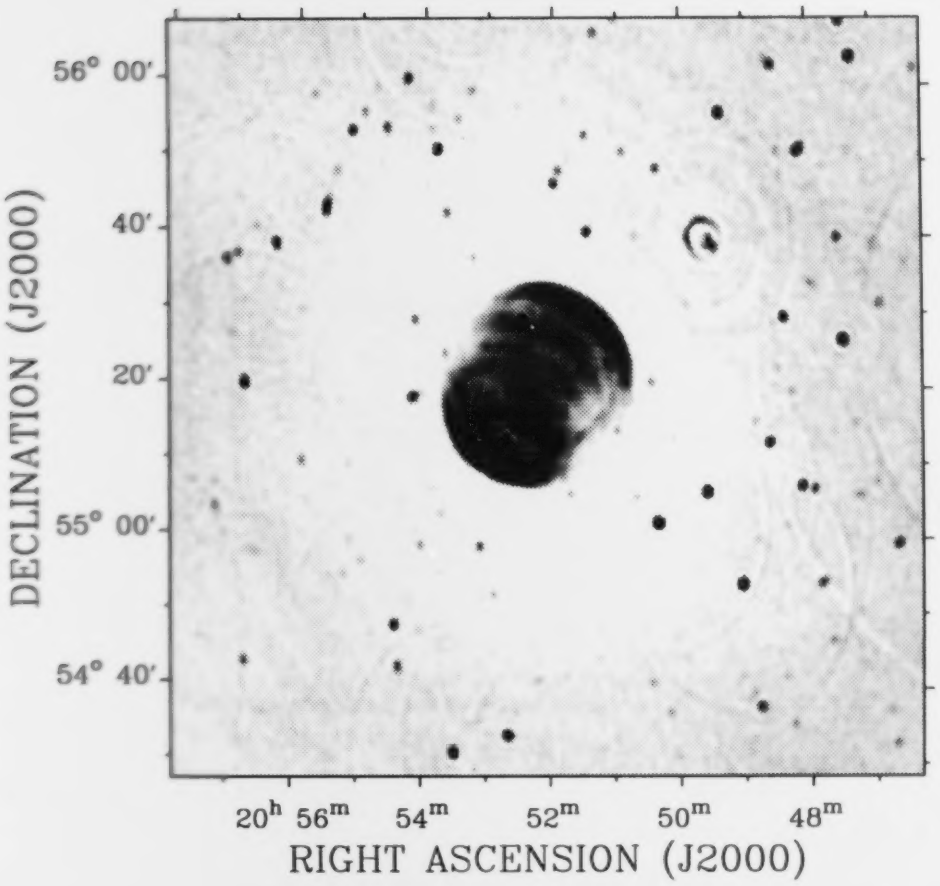

Figure 5.2: The offset field observation of DA530. This is a total intensity map in which darker shading corresponds to increasing positive levels. The phase centre is at RA 20H 49M 39.00S and DEC 55D 40′ 7.0″. The CLEAN algorithm has not been applied to this map as indicated by the presence of rings around the many strong unresolved sources in the field. The defect is clearly visible at the phase centre and is seen to contain both positive and negative (white) peaks with the positive peaks of comparable intensity levels to that of the DA530 interior. The negative bowl surrounding DA530 results from absence of data corresponding to baselines shorter than 13 m.

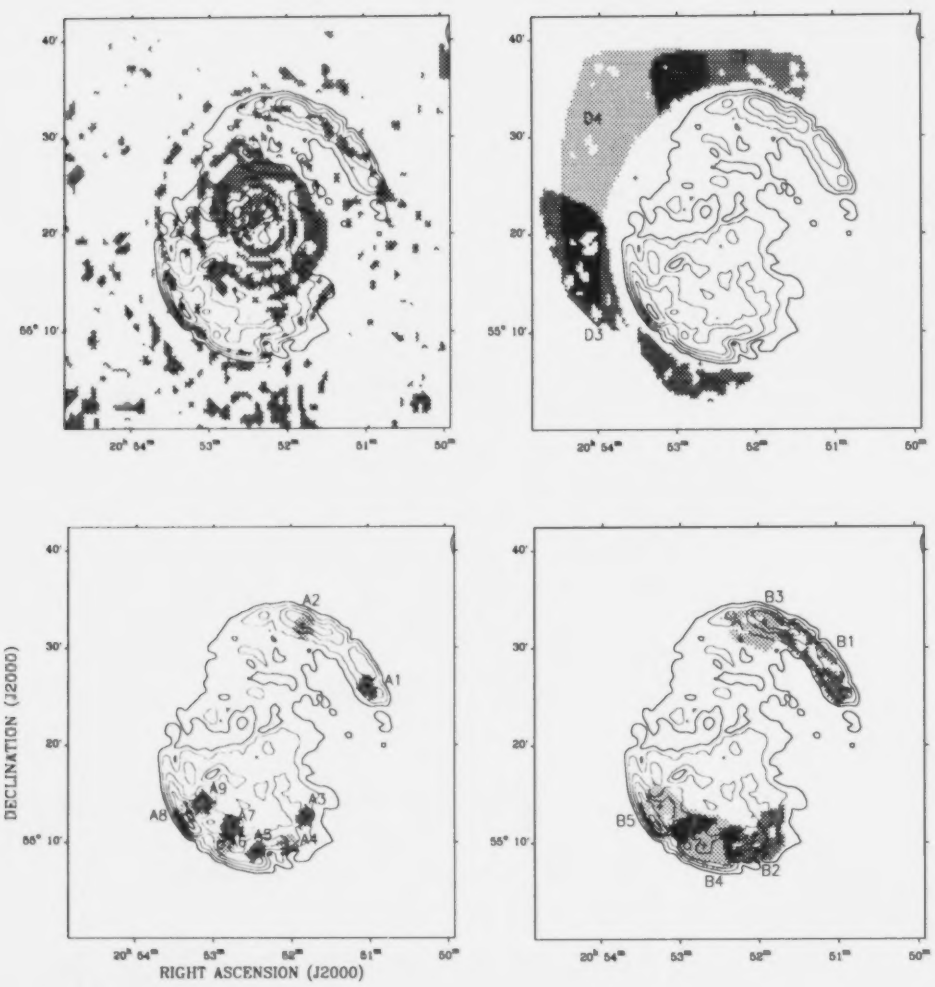

Figure 5.3: Maps of sample regions and corrupted data within DA530 that are used in the polarimeter performance evaluation. The shaded regions in the top left are corrupted data excluded from the analysis of map errors. The top right depicts regions adjacent to DA530 that are used for map background noise evaluation and the two bottom maps depict test regions used for evaluation of differences between the centred and offset maps. The contours are of polarized intensity and included as a reference. The darkest shading is overlap between the regions.

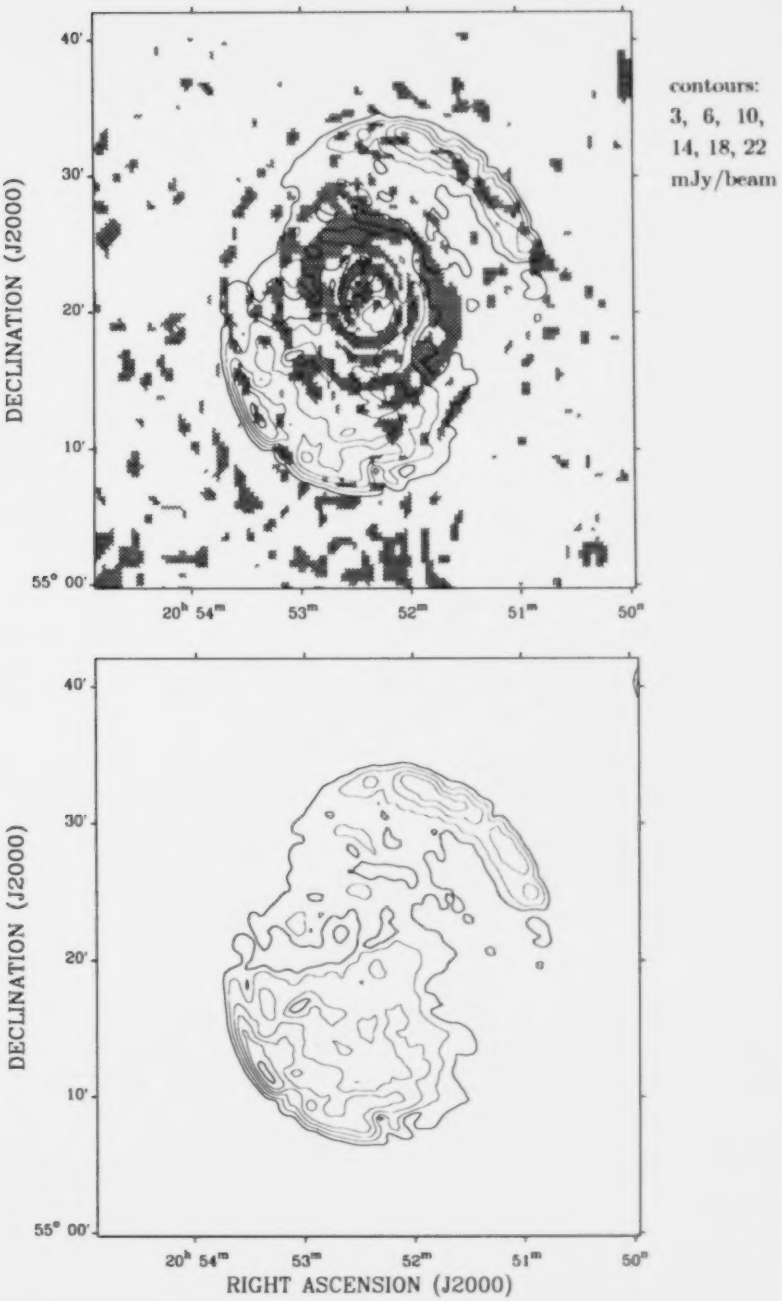

Figure 5.4: A Comparison of linearly polarized intensity between the centred (top) and offset (bottom) observations of DA530 with the DRAO synthesis telescope. The shaded regions are corrupted data associated with the centred observation.

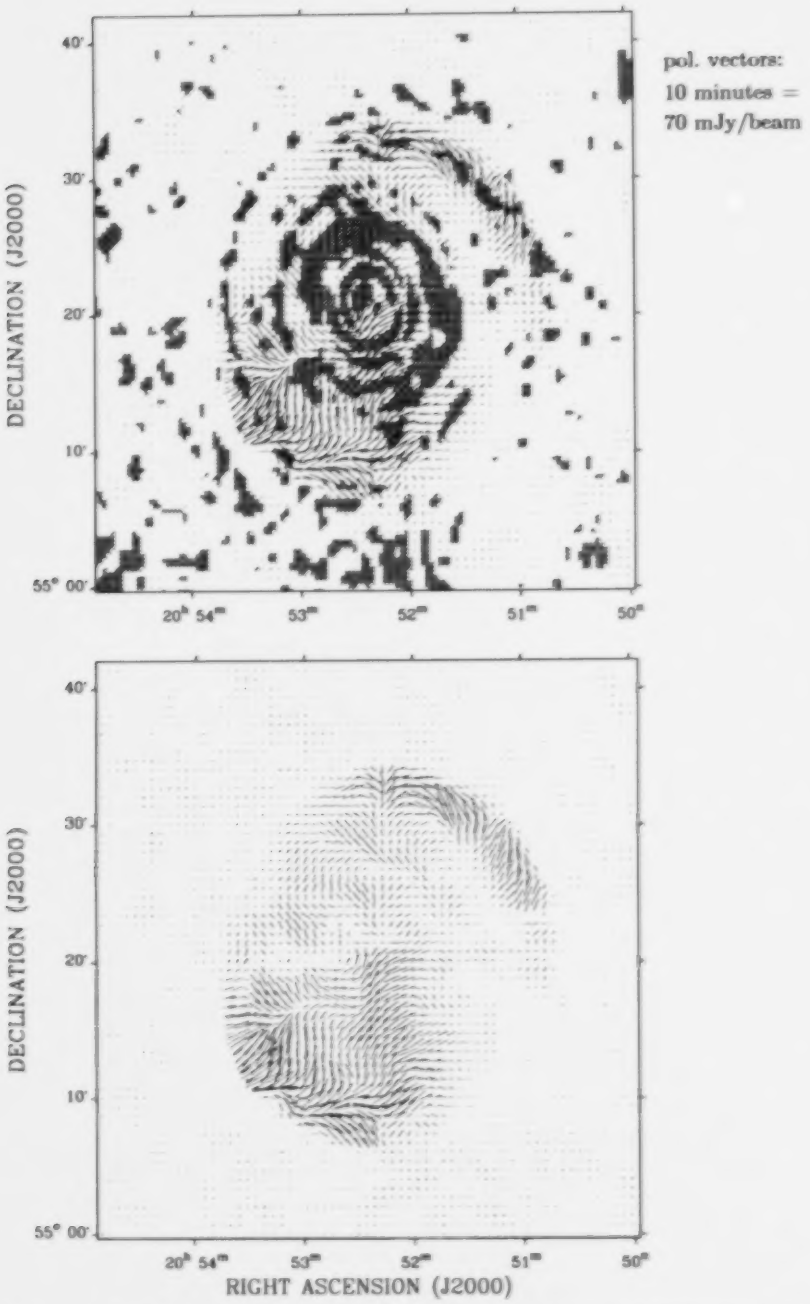

Figure 5.5: A Comparison of polarization vector maps between the centred (top) and offset (bottom) observations of DA530 with the DRAO synthesis telescope. The shaded regions are corrupted data associated with the centred observation.

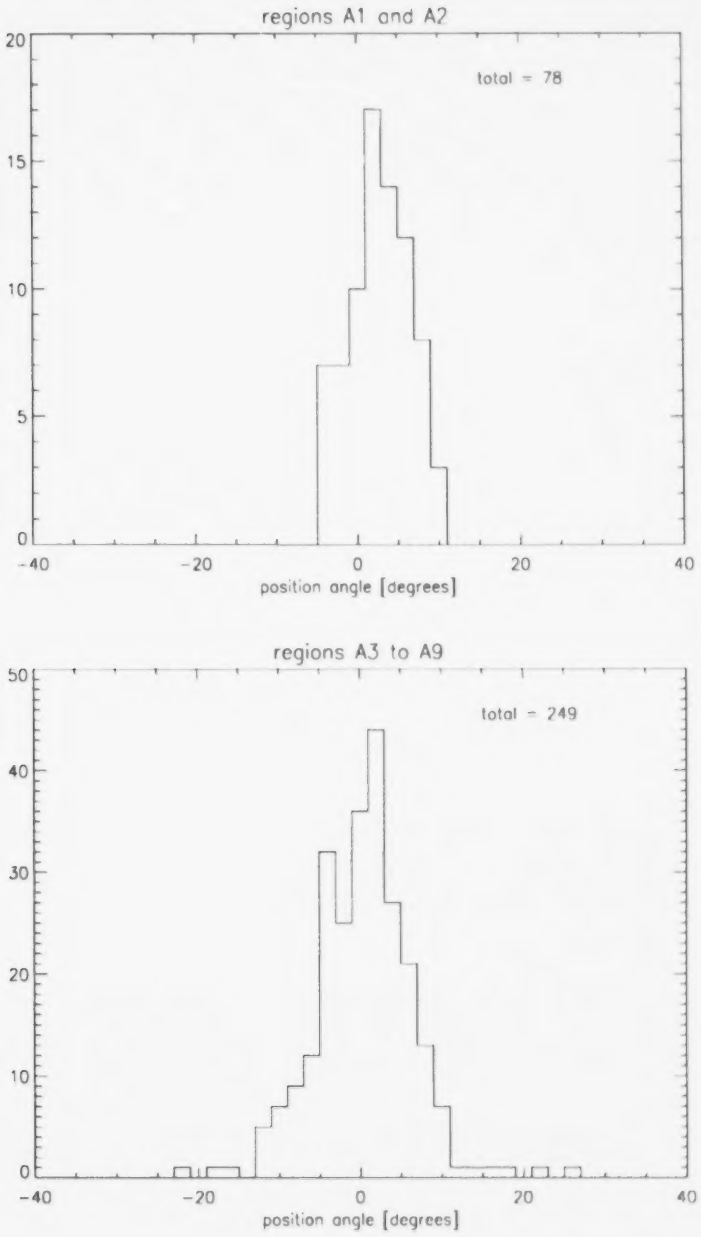

Figure 5.6: Probability density histograms of the position angle difference between centred and offset fields of the DA530 observation using sample set 'A'. The bin size is 2 degrees. The top plot was made from points on the northwest rim of the remnant and the right plot from points on the southeast rim.

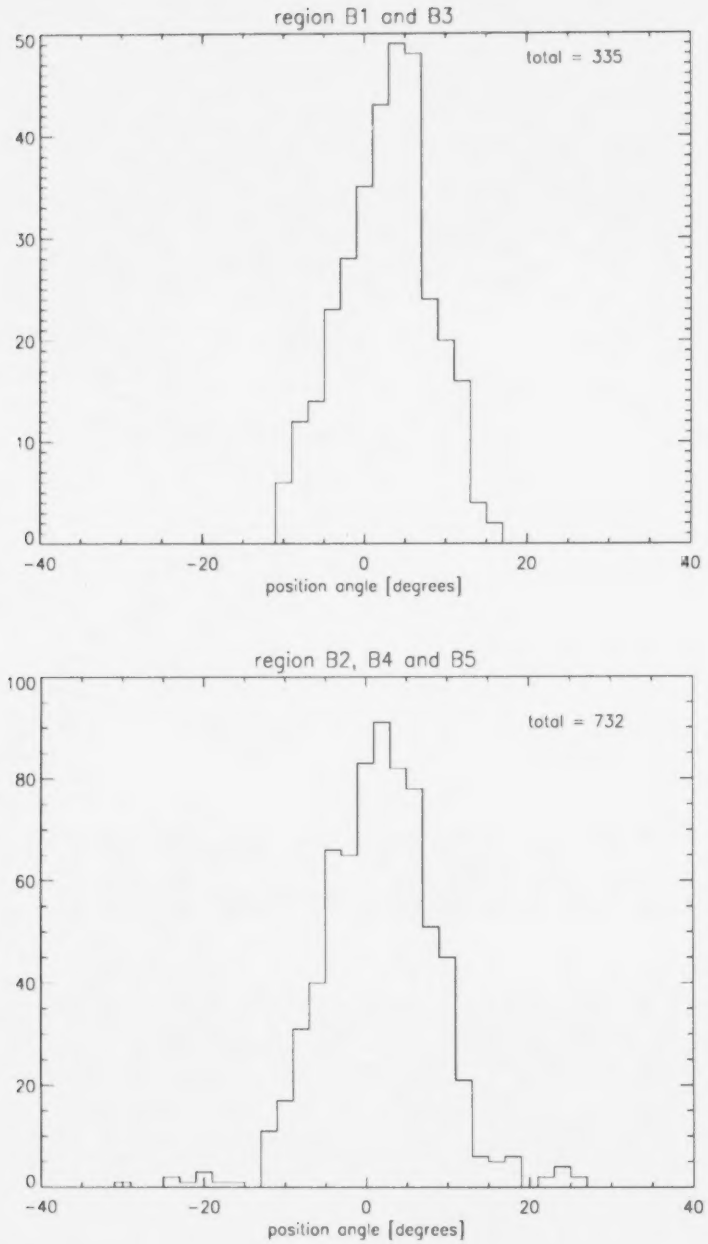

Figure 5.7: Probability density histograms of the position angle difference between centred and offset fields of the DA530 observation using sample set 'B'. The bin size is 2 degrees. The top plot was made from points on the northwest rim of the remnant and the right plot from points on the southeast rim.

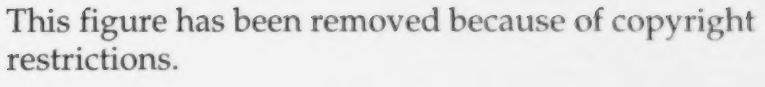

Figure 5.8: These figures were extracted from Lalitha et al. (1984). The top plots contain polarization vectors on top of total intensity contours (left) and polarized intensity contours (right). The bottom left is a map of rotation measure across DA530 as determined from the observations at 4.7 GHz by Lalitha et al. (1984) and at 2.7 GHz by Haslam et al.(1980). The bottom right is a plot of the projected magnetic field within DA530.

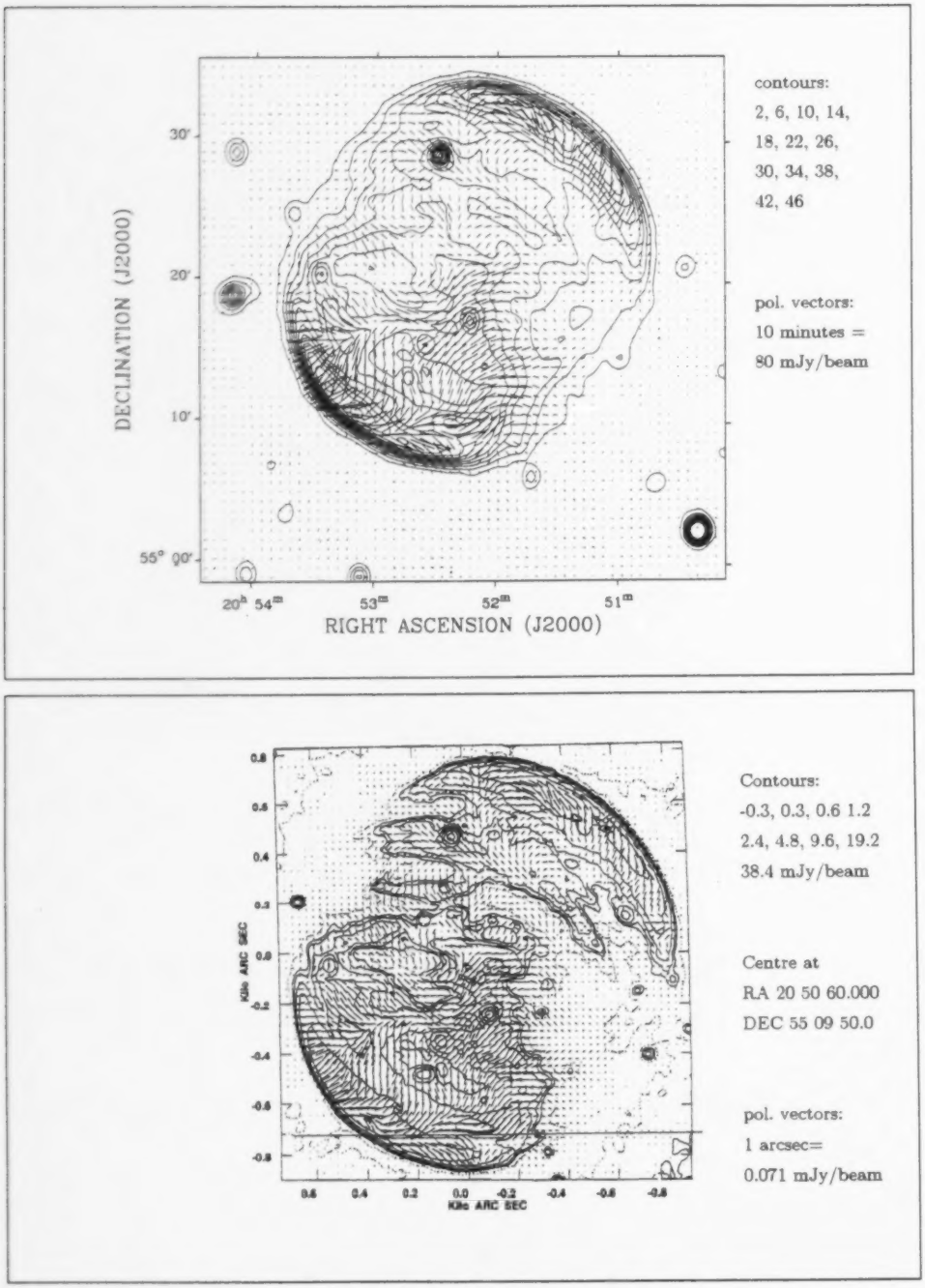

Figure 5.9: The top and bottom boxes depict DA530 as observed at DRAO and the VLA respectively. Polarization vectors are superimposed on contours of total intensity.

Bibliography

Barnes, R.M., Polarimetric Calibration Using In-scene Reflectors, Massachusetts Institute of Technology Lincoln Laboratory *Project Report TT-65*, 10 Sept., 1986

Beran, M.J., Parrent, G.B., *Theory of Partial Coherence*, Prentice-Hall, Englewood Cliffs, N.J., 1964

Bevington, P.R., *Data Reduction and Error Analysis for the Physical Sciences*, McGraw-Hill, New York, 1969

Born, M., Wolf, E., *Principles of Optics*, Pergamon Press Inc., London, 1959

Bracewell, R.N., *The Fourier Transform and its Applications*, McGraw-Hill, New York, 1978

Bridges, G.E., Shafai, L., Kishk, A.A., MOM Analysis of a Cavity-Fed Shaped Beam Reflector Antenna, *ANTEM 1990 conference proc.*, Dept. of Electrical and Computer Engineering, Winnipeg, 1990

Chatterjee, R., *Elements of Microwave Engineering*, Ellis Horwood div. of John Wiley and Sons, Chichester Eng., 1986

Deschamps, G.A., Mast, P.E., Poincare Sphere Representation of Partially Polarized Fields, *IEEE trans. Ant. Prop.*, vol. 21 no. 4, pp 474:478, 1973

Gardiol, F.E., *Introduction to Microwaves*, Artech House, Dedham, MA, 1984

Gardner, F.F., Whiteoak, J.B., *Ann. Rev. Astron., Astrophys* **4**, 245:292

Harrington, R.F, *Time-Harmonic Electromagnetic Fields*, McGraw-Hill, New York, 1961

Haslam, C.G.T., Pauls, T., Salter, C.J., G93.3+6.9: A Highly Polarized Supernova Remnant, *Astron. Astrophys.* **92**, pp 57:62, (1980)

IEEE, Standard Test Procedures for Antennas, Std. 149-1979, The Institute of Electrical and Electronics Engineers, New York, 1979

IEEE, Standard Definitions of Terms for Radio Wave Propagation, Std.211-1977, The Institute of Electrical and Electronics Engineers, New York, 1977

Ko, H.C., Coherence Theory of Radio-Astronomical Measurements, *IEEE Trans. Ant. Prop.*, vol. 15, no. 1, Jan., 1967

Ko, H.C., On the Reception of Quasi-Monochromatic, Partially Polarized Radio Waves, *Proc. IRE*, vol. 50, pp 1950:1957 , Sept., 1962

Kraus, J.D., *Radio Astronomy*, Cygnus-Quasar Books, 1980

Lalitha, P., Mantovani, F., Salter, C.J., Tomasi, P., The Morphology and Magnetic Field Structure of Supernova Remnant G93.3+6.9, *Astron. Astrophys.* 131, pp 196:199, 1984

Lee, Shug-Wu, Okubo, E.K., Ling, H., Polarization Determination Utilizing Two Arbitrarily Polarized Antenna, *IEEE Trans. Ant. Prop.*, vol. 36, No. 5, 1988

Marcuvitz, N., *Waveguide Handbook*, Peter Pereginus, London, 1986

Mott, H., *Polarization in Antennas and Radar*, John Wiley and Sons, 1986

Roger, R.S., Costain, C.H., *DA 530 - A High Latitude Supernova Remnant* Astron. Astrophys., 51, pp 151:153

Rudge, A.W., Milne, K., Olver, A.D., Knight, P., ed., *The Handbook of Antenna Design (vol. 1 and 2, paperback)*, Peter Peregrinus on behalf of the Institution of Electrical Engineers, London, 1986

Simard-Normandin, Martine, Kronberg, P.P., *Astrophys. J.*, 242, pp 74:94, 1980

Simmons, A.J., A Compact Broad-Band Microwave Quarter-Wave Plate, *Proc. IRE* 40, pp 1089:1090, 1952

Spoelstra, T.A.T., Linear Polarization of the Galactic Radio Emission at Frequencies Between 408 MHz and 1411 MHz, *Astron. Astrophys.* 135, pp 238:248, 1984

Stokes, G., On the Composition and Resolution of Streams of Polarized Light from Different Sources, *Trans. Cambridge Phil. Soc.*, vol. 9, pt. 3, pp 399:416, 1852

Tabara, H., Inoue, M., Catalogue of Radio Sources, *Astro. Astrophys. Supp.*, 39, 379-393, 1980

Thompson, R.A., Moran, J.M., Swenson, G.W., *Interferometry and Synthesis in Radio Astronomy*, John Wiley and Sons, 1986

Verschuur, G.L., Kellermann, K.I *Galactic and Extragalactic Radio Astronomy*, Springer-Verlag, 1988